Growth and physical properties of crystalline rubrene

PhD thesis of
Enrico Maria Fumagalli
Matricola 054812

Supervisor : Prof.ssa Adele Sassella

Coordinator of the School: Prof. Gianpaolo Brivio

Cycle XXV

Period 2010 - 2012

Contents

Introduction

Organic compounds showing semiconducting properties, whose study began in the last decades of the past century, are now moving from being a pure research interest to their industrial application in the fabrication of a wide range of electronic devices. Indeed, since the fabrication of the first field effect transistors (FETs) based on polymers or small molecular weight organic materials[1–3], these materials are now finding application, alone or in conjunction with inorganic semiconductors, as the active layers in various kinds of electronic devices: organic light emitting diodes (OLEDs) used for displays or environmental illumination[4–7], organic photovoltaic cells[8–10], radio frequency identification tags (RFIDs)[11], organic lasers[12] and sensors[13]. The market deployment of some of these devices has already begun, for example in the case of OLEDs.

The interest toward these materials is mainly motivated by the low-cost techniques required for their processing, their mechanical properties (such as their flexibility) and the possibility to tailor their electronic properties by modifying their molecular structure.

A common feature of organic semiconductors is the presence of delocalized π molecular orbitals leading to delocalization of the electronic charge along the whole molecule. Apart from this common trait, molecules belonging to this class of materials can show a wide range of different properties. A first classification of these materials is that distinguishing between polymers and small molecular weight materials, referring to the length of the conjugated system. In the case of polymers the active layer is generally deposited by solution based methods (such as spin-coating), while small molecule materials are usually deposited by evaporation methods. The latter methods, while being generally more complicated and requiring a more controlled environment, lead to greater control over the structure of the deposited layers and are thus particularly indicated for the study of the fundamental proper-

ties of these materials. Even more controlled and defect-free structures can
be obtained with single crystals. The understanding gained by studying the
properties of single crystals can then be exploited for the optimization of the
properties of crystalline thin films.

Among small molecule organic semiconductors, one of the most promis-
ing is rubrene (5,6,11,12-tetraphenyltetracene), which in the single crystal
form reaches the highest charge carrier mobility values among organic semi-
conductors, up to $\approx 40\,cm^2/Vs$, a value comparable to that of amorphous
silicon[14, 15]. Rubrene single crystals show also an extremely high photo-
conductivity and large exciton diffusion length[16, 17]. While rubrene single
crystals with a size up to few centimeters can be prepared quite easily by
sublimation methods[18], the growth of crystalline thin films with the same
structural properties (and thus the same transport properties) of rubrene
single crystals is not as straightforward[19–24]. While the choice of the right
substrate and deposition technique for the growth of rubrene thin films can
lead to crystalline thin films, they always consists of polycrystalline layers
with multiple in-plane orientations[25–28]. The high anisotropy of rubrene
transport properties make it thus impossible to achieve mobility values close
to those found for rubrene single crystals.

Rubrene molecules are also strongly affected by oxidation, particularly in
the presence of light, leading to the formation of rubrene endoperoxide[29].
Several theoretical and experimental studies have been carried out in order
to understand the effects of oxidation over transport and optical properties
of crystalline rubrene, but a clear picture is still missing and lots of contra-
dictory results have been reported[30–35]. In order to exploit rubrene as the
active layer of electronic devices operating in ambient atmosphere a deeper
understanding of its oxidation mechanism and of its effects over crystalline
rubrene transport properties is thus mandatory.

The aim of the experimental work described in this thesis has been to gain
more control over the growth of rubrene in the thin film form, by exploiting
epitaxy with proper substrates and then to study the effects of the interac-
tion with oxygen over the structural and transport properties of crystalline
rubrene.

In chapter 1, a general overview of the properties of organic molecular
solids is presented, with a focus over the physical properties of organic small
molecule crystals.

Chapter 2 is devoted to a thorough description of rubrene physical and chemical properties, with a presentation of the state of the art and of the main open problems related to this material.

In chapter 3 the experimental techniques exploited for the preparation and characterization of the samples studied in the following chapters are presented.

The growth and structural/morphological characterization of rubrene thin films grown by means of organic molecular beam epitaxy on two different substrates, namely tetracene single crystals and α-quaterthiophene crystalline thin films grown on potassium hydrogen phthalate single crystals, are presented in chapter 4. The latter heterostructure is of particular interest regarding its use in the fabrication of organic cascade solar cells. Here, thanks to the adoption of several characterization techniques it will be shown that rubrene thin films grown on the (0 0 1) surface of tetracene single crystals are crystalline and, even more important, grow according to a unique epitaxial relationship with the substrate, which in turn leads to a unique crystalline orientation of the film in the growth plane. Rubrene thin films grown on α-quaterthiophene still grow according to a unique epitaxial relationship but, due to symmetry reasons, show four different in-plane orientations of their crystalline lattice.

Rubrene thin films grown on tetracene, whose structural characterization has been carried out in chapter 4, are then studied with regard to their morphological and structural evolution upon oxidation. The results of this characterization are reported in chapter 5. There, thanks to a combination of various experimental techniques, it is shown that the exposition of rubrene thin films to ambient air leads to the formation of a stable crystalline layer of rubrene endoperoxide molecules, packed according to a specific crystalline structure, on top of the pristine rubrene film. This process somehow resembles what happens for silicon with the formation of a native oxide layer.

Finally, in chapter 6 the results of dark and photo-conductivity measurements carried out on rubrene and rubrene derivatives single crystals, aimed at determining the effects of interaction with oxygen over rubrene transport properties, are presented. There, it is demonstrated that the interaction with oxygen plays an essential role in enhancing crystalline rubrene transport properties. In particular the experimental results suggest that what is important for electrical transport in crystalline rubrene is the interstitial

molecular oxygen included in the crystal and not the formation of rubrene endoperoxide molecules.

At the end a short summary of the results presented in this thesis is given, along with the presentation of some of the open perspectives for the prosecution of this work.

Chapter 1

Organic semiconductors

1.1 Organic molecular solids: an introduction

With the term *organic molecular solids* one generally refers to a wide range of different solids, such as single crystals, polycrystals, glasses or thin-films formed by organic molecules, i.e. molecules whose main constituents are carbon atoms[36]. In particular, the focus of this work is on single crystals or crystalline films formed by organic conjugated molecules. In an organic conjugated molecule the carbon atoms have an sp^2 hybridization of their valence orbitals, as sketched in figure 1.1 for the benzene molecule, the simplest conjugated organic molecule. This kind of hybridization leads to the formation of three σ orbitals for each atom in the plane of the molecule, forming an angle of 120° to each other, and of a single p_z orbital directed along the normal to the molecular plane. The overlap between the p_z orbitals of neighboring atoms leads to the presence of delocalized electrons above and below the molecular plane, in what is called a π molecular orbital. Electrons in the π orbitals are relatively weakly bound to the molecule, and energies of a few eV are enough to excite them to higher energy levels. Because of this these molecules absorb and emit light in the visible range. In general, the excitation energy needed to excite a π electron decreases with increasing length of the conjugated system. The presence of these weakly bound electrons in the π orbitals is the reason for many of the peculiar properties of these systems, such as their solid state optical and electric transport properties, which will be described in the following paragraphs.
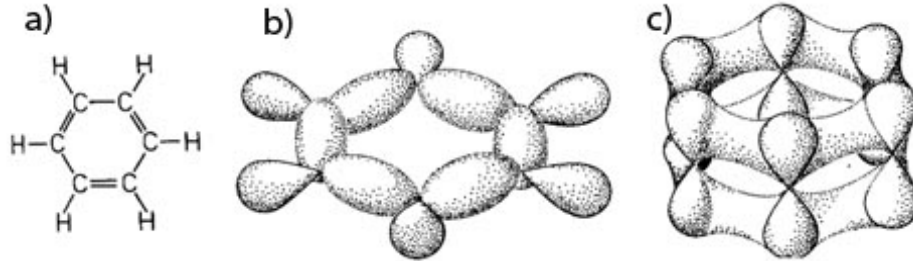
Figure 1.1: Electronic structure of a conjugate molecule. (a) Structural formula of a benzene molecule. (b) Disposition of its σ orbitals. These orbitals are all on the same plane and form 120° angles between each other. (c) The superposition of the p_z orbitals of neighboring atoms leads to the formation of π orbitals and to the presence of a delocalized charge density on the entire molecule, with a nodal plane in correspondence of the molecular plane.

1.2   Organic molecular crystals

In general the bonding between molecules in a crystal can be of different kinds: ionic, covalent, metallic or van der Waals. The kind of the interactions holding together the crystal strongly influences its physical properties, such as the melting point, electrical or optical properties. In the case of small conjugated molecules, due to the absence of a net molecular dipole moment the main interactions are of the van der Waals kind. Such interactions are due to the instantaneous fluctuations of the charge density around each molecule, leading to the establishment of weak induced-dipole - induced-dipole interactions, whose dependance from the intermolecular distance r is given by r^{-6}. With respect to the repulsive forces between the core electrons of the atoms constituting each molecule, relevant when two molecules are too close to each other, their dependance from r can be given by the empirical potential C_{12}/r^{12}, where C_{12} is an empirical parameter depending on the specific kind of interacting molecules. One can then express the interaction potential $V(r)$ between two adjacent molecules of the same kind with the Lennardt-Jones potential:

$$V(r) = \frac{C_{12}}{r^{12}} - \frac{A}{r^6} \tag{1.1}$$

where A is a parameter depending on the specific kind of molecules being considered. The dependance of the van der Waals potential on r^{-6} makes these interactions particularly weak. Because of this, molecules forming molecular crystals retain most of the properties of the free molecule.

Moreover, owing to the short range of van der Waals interactions, the lattice energy of molecular crystals is minimized when they are packed with the highest possible density. Indeed, defining the packing coefficient K of a specific crystal unit cell as:

$$K = Z\frac{V_0}{V} \qquad (1.2)$$

where Z is the number of molecules in the unit cell, V is the volume of the unit cell and V_0 is the volume occupied by each molecule, in the case of organic conjugated molecules the values of K are well above 0.5, while in the case of common covalently bonded crystals it is well below that value.

Owing to the complex three-dimensional structure of organic molecules, not only the packing density, but also the relative orientation of the different molecules in the unit cell gives a significant contribution to the coesion energy of the crystal. Moreover, due to the weak intermolecular interactions, depending on the particular growth conditions a molecule can form crystals with different symmetries, different lattice parameters and different molecular packing[37, 38].

1.3 Small-molecule organic semiconductors

With the term 'organic materials' one refers to the wide range of molecular compounds whose main constituent are carbon atoms. The physical properties of such molecules span a wide range, going for example, with respect to their electrical properties, from highly resistive materials to highly conductive or even superconductive ones. In particular, owing to the highly delocalized π electrons coming from the sp^2 hybridization of the carbon atoms constituting them (see figure 1.1c), conjugated aromatic molecules have particularly good electrical transport properties if compared to other classes of organic materials. A first distinction between different organic conjugated compounds is that between small molecule materials and polymers. All the research work reported in this thesis is focused only on small molecule organic semiconductors, which will be described in depth in the following paragraphs, and from now on with the expression 'organic semiconductors' we will refer only to those ones.

1.3.1   Optical properties of organic semiconductors

Among the most interesting properties of organic molecular crystals there are their peculiar optical properties, in particular their ability to conduct optical excitation energy within the crystal, and to transfer it. Moreover, unlike what happens for inorganic solids, the electronic excited states of organic molecular crystals strongly resemble those of the corresponding isolated molecules. This, like most organic molecular crystals properties, comes from the weakness of the intermolecular interactions in such materials, leading only to a small perturbation of the electronic structure of the molecules when they are packed in the crystal.

Nonetheless, the presence of the Van der Waals interactions leads to some difference between the electronic and vibrational spectra of the isolated molecule and of the relative molecular crystal, namely[36]:

- a general shift, called *solvent shift*, toward lower energies, due to the van der Waals interactions between adjacent molecules;

- a splitting of each peak in a maximum of Z different peaks, where Z is the number of molecules not symmetrically equivalent in the unit cell. This effect is called *Davydov splitting*. The different peaks are also often differently polarized;

- the delocalization of the excitation between all the molecules in the crystal leads to the formation of the so-called *excitonic bands*, and thus to a general broading of the peaks;

- a total, or partial, removal of the degeneracy of the excited levels and a change in the selection rules for the optical transitions. This is due to the fact that in crystals the selection rules are determined not only by the symmetry of the single molecule, but also by that of the whole crystal;

- for transitions with a particularly high oscillator strength, the effects of the solvent shift and of the Davydov splitting can be strong enough to completely remove any resemblance of the crystal spectrum with that of the single molecule.

All these effects find an explanation in the molecular exciton theory, developed by Davydov[39], that permits to build the eigenstates of a perfect,

rigid crystal of $N\sigma$ identical weakly interacting molecules, N being the number of unit cells in the crystal and σ the number of molecules per unit cell. Considering the simpler case, in which the molecules are considered as two level systems with the wave function and energy of the ground and excited states given by φ^0, e_0, φ^* and e^*, respectively, the Hamiltonian H of the system is given by:

$$H = \sum_{n\alpha}^{N} H_{n\alpha} + \sum_{n\alpha m\beta}' V_{n\alpha m\beta} \qquad (1.3)$$

where $H_{n\alpha}$ is the Hamiltonian of the isolated molecule in the lattice position $n\alpha$ and $V_{n\alpha m\beta}$ is the van der Waals interaction potential between the two molecules in the $n\alpha$ and $m\beta$ lattice sites. If $V_{n\alpha m\beta}$ is considered small with respect to $\sum H_{n\alpha}$ it can be described as a perturbation within a tight-binding approximation. The wave function Ψ of the crystal ground state is given by the antisymmetrized product of the ground state wave functions of the single molecules and the corresponding energy at the first order is given by:

$$E_0 = Ne_0 + \sum_{n\alpha m\beta}' \left\langle \varphi_{n\alpha}^0 \varphi_{m\beta}^0 | V_{n\alpha m\beta} | \varphi_{n\alpha}^0 \varphi_{m\beta}^0 \right\rangle = Ne_0 + D \qquad (1.4)$$

where the term D accounts for the total energy of the van der Waals interactions holding together the crystal.

The wave functions Ψ^* of the crystal excited states (or excitons) can be built by considering a single molecule in its excited state, the excitation being completely shared among all the molecules constituting the crystal. Crystal periodicity has then to be included and a wave vector $\mathbf{k}$ is introduced, which takes N values in the first Brillouin zone. The corresponding eigenenergies $E(\mathbf{k})$ form the electronic bands (or excitonic bands) of the crystal and are given by:

$$E(\mathbf{k}) = E_0 + e^* - e_0 + \Delta D \pm I(\mathbf{k}) \qquad (1.5)$$

Here, ΔD is the solvent shift, representing the difference between the interaction energy D of a single molecule in its ground state with all the other molecules comprised in the crystal and the interaction energy D' of the same molecule in its excited state with all the other molecules (see also figure 1.2). $I(\mathbf{k})$ is instead the so-called resonance term (or exciton shift), and represents the transfer interaction between a molecule in a specific lattice site and all the other molecules and thus accounting for the fact that the molecular
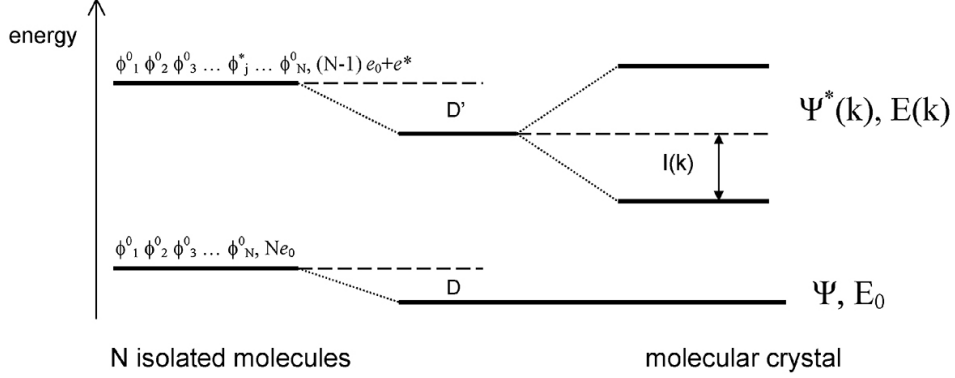
Figure 1.2: Energy levels scheme showing the ground state energy level and the first excited energy level for an assembly of N identical non-interacting molecules (*left*) and for the corresponding molecular crystal (*right*). In the right part of the image the opening of an energy band in correspondence of the first excited level is shown. The symbols are explained in-text. From [40].

excitation originating the crystal excited state can either be on the lattice site where it originated or anywhere else in the crystal. This last term is also responsible for the dispersion (*i.e.* the dependence of $E(\mathbf{k})$ on $\mathbf{k}$) of the excitonic band. These two terms are given by:

$$\Delta D = \sum_{m\beta}^{N\sigma}{}' \left\{ \left\langle \varphi_{n\alpha}^* \varphi_{m\beta}^0 | V_{n\alpha m\beta} | \varphi_{n\alpha}^* \varphi_{m\beta}^0 \right\rangle - \left\langle \varphi_{n\alpha}^0 \varphi_{m\beta}^0 | V_{n\alpha m\beta} | \varphi_{n\alpha}^0 \varphi_{m\beta}^0 \right\rangle \right\}$$

$$(1.6)$$

and

$$I(\mathbf{k}) = \sum_{m\beta}^{N\sigma}{}' \left\{ \left\langle \varphi_{n\alpha}^* \varphi_{m\beta}^0 | V_{n\alpha m\beta} | \varphi_{m\beta}^* \varphi_{n\alpha}^0 \right\rangle e^{i\mathbf{k}\cdot(\mathbf{r}_{n\alpha}-\mathbf{r}_{m\beta})} \right\} \qquad (1.7)$$

where $\mathbf{r}_{n\alpha}$ indicates the position of the molecule in the site α of the n-th unit cell.

Once the ground and excited states of the crystal are known, time-dependent perturbation theory can be used for the description of the dielectric behavior of the crystal, *e.g.* the transition probabilities and transition moments between two states, the corresponding selection rules, the complete dielectric tensor, etc. For instance, the modulus M of the transition moment for a dipole transition between E_0 and $E(\mathbf{k})$ for an ideal crystal with all aligned identical molecules shows a relationship to the molecular dipole

Frenkel   Wannier   Charge-transfer
exciton   exciton   exciton
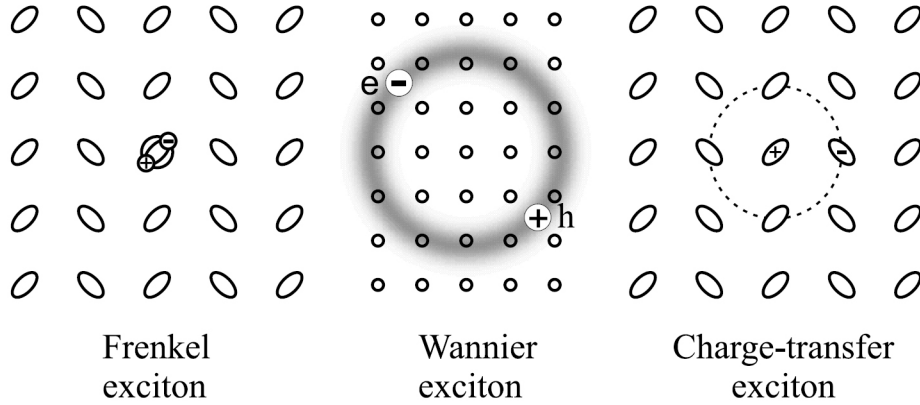
Figure 1.3: Classification of excitons on the basis of the electron-hole pair radius. From [36].

moment $\boldsymbol{\mu}$ given by:

$$M \propto \frac{|\boldsymbol{\mu}|^2}{\mathbf{r}^3} \propto \frac{f}{(e^* - e_0)} \tag{1.8}$$

where $e^* - e_0$ is the energy difference corresponding to the molecular transition $\varphi^0 \to \varphi^*$, $\mathbf{r}$ is the intermolecular distance, and f is the oscillator strength for the single molecule transition. Even for more complex crystals the proportionality between the two momenta still holds, indicating the close link between crystal and molecular properties typical of organic crystals.

As already noted, the result of the coherent excitation of molecules in the crystal is called molecular exciton. Excitons are usually classified on the basis of the radius of the electron-hole pair, as exemplified in figure 1.3. Frenkel excitons, which are the most common type of exciton found in molecular solids, are formed by an electron-hole pair residing on the same molecule and which is able to move around the crystal by jumping between adjacent molecules. The other limiting case, common for inorganic semiconductors and not found in molecular crystals, is that of the Wannier exciton, with a radius of the electron-hole pair corresponding to several primitive lattice vectors. The intermediate case, called charge transfer exciton, can also be found in aromatic molecular crystals, and is formed when an electron or hole is transferred between two adjacent molecules, giving rise to an ion pair.

The importance of molecular excitons lies in their ability to conduct electronic excitation energy within molecular crystals, a process which is also extremely relevant for their electric transport properties and in particular for the development of photovoltaic devices based on these materials.

1.3.2   Electrical transport properties of organic semiconductors

With respect to electric transport properties, most organic molecular solids have an insulating behavior; nonetheless crystals formed by conjugated molecules may show a semiconducting behavior[36, 41].

The performance of organic semiconducting materials with respect to charge transport properties is usually characterized by means of their charge carrier mobility μ, defined, as in the inorganic materials, by:

$$\mu = -\frac{e\tau}{m} \tag{1.9}$$

and entering in the equation for current transport as:

$$\mathbf{j} = -en\mu\mathbf{E} \tag{1.10}$$

where e is the electron charge, τ is the charge carrier relaxation time, m is their mass, n is their volume density, $\mathbf{j}$ is the current density and $\mathbf{E}$ is the electric field.

In general, charge carrier transport in organic semiconductors can be established thanks to two different mechanisms, depending on the crystal purity and quality and on the intensity and degree of anisotropy of the intermolecular interactions: *band-like* transport or *hopping* transport. Those two mechanism can usually be distinguished by the temperature dependence of the charge carrier mobility and lead to different ranges of mobility values.

Band-like transport is the same transport mechanism characteristic of inorganic semiconductors and is usually found for highly ordered and pure crystals. In this case, charge carriers mobility is inversely proportional to temperature, since charge transport is hindered by the scattering from thermal phonons. Moreover, the strong anisotropy typical of molecular crystals leads, for this class of materials, to highly directional charge transport properties. In this case charge carrier mobility can reach values up to tens of cm^2/Vs, that is, values typical of inorganic amorphous or polycrystalline solids. In the case of conjugate molecular crystals the charge transport is mainly due to electrons in the π orbitals[42].

Hopping transport is instead a thermally activated mechanism, for which charge carriers *hop* discontinuously between adjacent molecules. This transport mechanism is usually predominant in crystals with high lattice disorder

or with an high impurity and defect content. In this case mobility is proportional to temperature, since thermal energy favors hopping of charge carriers from molecular site to site. For this kind of organic semiconductors μ is generally the order of $10^{-3}\,\mathrm{cm}^2/\mathrm{Vs}$, or lower.

Even in the case of band-like transport, which gives the highest values of μ, molecular crystals have poorer transport properties with respect to inorganic semiconductors. This is indeed one of the main challenges that need to be addressed in order to fabricate electronic devices. It's particularly important to develop adequate purification, growth and characterization techniques.

As a final remark, it is important to notice that, despite the use of concepts typical of the inorganic semiconductors field, the understanding of charge transport in organic materials is way more complicated due to the peculiarities of these class of materials. For instance, while inorganic semiconductors can be well described via the one-electron approximation, in the case of organic semiconductors electron-electron and electron-phonon interactions can not be neglected. This results in the so-called *polaron* model, whose main application field is that of charge transport in polymers but that can also be adapted to small molecule compounds, in which the charge carriers are actually quasiparticles, called polarons, constituted by the charged particle itself and by the polarized environment surrounding it and following the particle in its motion[41]. Despite being the most widely accepted description of charge carrier transport in organic semiconductors, in particular for polymers, this picture is not unique, and in general a full understanding of the actual charge transport mechanism in organic semiconductors is still lacking.

Chapter 2

Rubrene: physical and chemical properties

2.1 Introduction

Rubrene (5,6,11,12-Tetraphenyltetracene, $C_{42}H_{28}$) is one of the most promising small molecule organic semiconductors, showing record values for most of the properties needed to build efficient devices, such as photocurrent generation efficiency, exciton diffusion length and charge carrier mobility[14, 16, 17]. At the same time it poses a lot of experimental challenges, because of its chemical instability in the presence of oxygen, because of the difficulties found in obtaining rubrene thin films with a good crystalline quality and also due to the still limited understanding of the origin of its most interesting properties, therefore not optimized yet. Thus, in this chapter we will first focus on the description of what is currently known about rubrene, and afterward we will indicate the main open problems connected with rubrene, some of them to be addressed in the following chapters of this work.

2.2 The molecule

Rubrene belongs to the group of polycyclic aromatic hydrocarbons and consists of a tetracene backbone (i.e. four linearly fused benzene rings) with a phenyl ring bonded on each side of the two central benzene rings, as shown by the structural formula and the three-dimensional sketch reported in figure
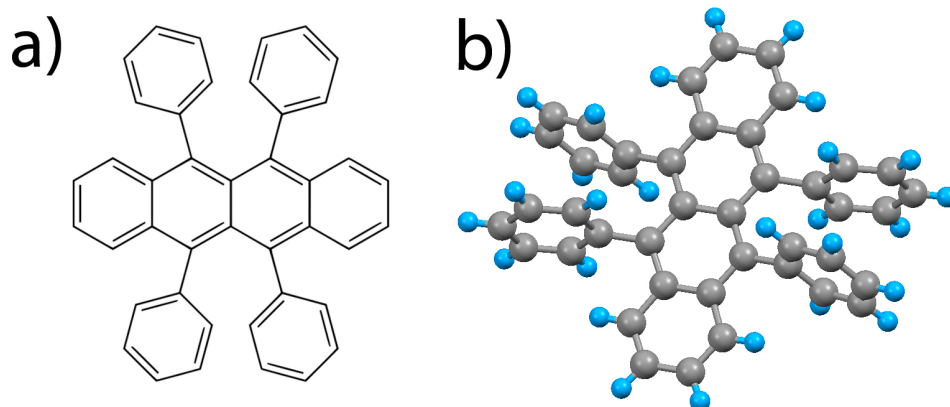
Figure 2.1: Structural formula (*a*) and three-dimensional sketch (*b*) of a rubrene molecule. The hydrogen atoms are omitted from the structural formula for clarity.

2.1.

When exposed to air, rubrene molecules in solution or in the amorphous phase readily oxidize, leading to the formation of rubrene peroxide, a process which is strongly enhanced by the presence of light[29, 43, 44]. Both molecular mechanics (MM) calculations and experiments show that the most common form of peroxide formed after rubrene oxidation is the endoperoxide[19, 45], in which molecular oxygen is linked to one of the two central rings of the tetracene backbone, as shown in figure 2.2a. The bonding with an oxygen molecule leads to a deformation of the molecular backbone, as shown in figure 2.2a, that in turn leads to the disruption of the delocalized nature of the π molecular orbital. This strongly affects the optical properties of the molecule: at a visual inspection both rubrene solutions and amorphous films rapidly turn transparent from their original reddish colour, reflecting the disappearence of the main rubrene absorption peaks in the visible range, which is also accompanied by the appearence of a new absorption band centered around $4.95\,\mathrm{eV}$[29]. This effect is shown in figure 2.2b, where the imaginary part of the dielectric function (ε_2) of a rubrene amorphous film collected at various times during its exposure to oxygen and light is reported. During the interval between the collection of the pristine spectrum and the one indicated with '0 min' the film has been kept in an oxygen atmosphere but in absence of light for $870\,\mathrm{min}$, making it evident that the process of oxidation is strongly enhanced by the presence of light.
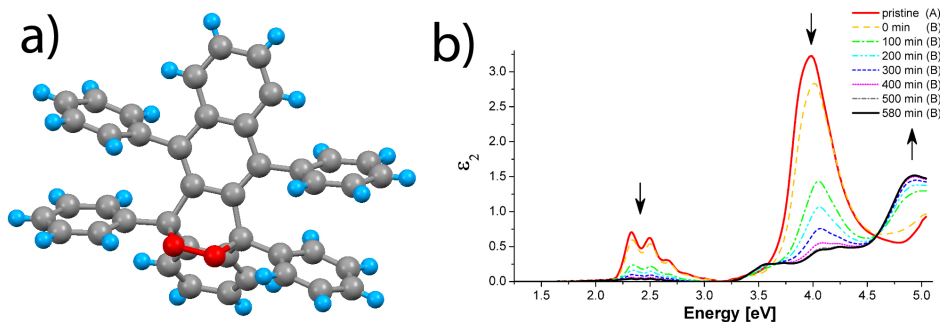
Figure 2.2: (*a*) Three-dimensional sketch of a rubrene endoperoxide molecule. The oxygen atoms are coloured in red. (*b*) Imaginary part of the dielectric function of an amorphous rubrene film measured during its exposition to oxygen and light. From [29]

2.3 Crystalline rubrene

Rubrene crystallization can be achieved by following several different routes, obtaining different polymorphs with their characteristic different molecular arrangments[46,47]. The molecular arrangment in the three main known rubrene polymorphs is shown in figure 2.3. The three structures are all observed from a direction normal to the long axis of the molecules, in order to show the amount of $\pi - \pi$ stacking between the conjugate backbones of adjacent molecules. The first two crystalline structures have a monoclinic and a triclinic unit cell, respectively, and can be obtained by solution crystallization methods[47]; the third structure has an orthorhombic symmetry and can be obtained by physical vapour growth[46].

The analysis of the three crystalline structures reported in figure 2.3 shows that:

- In the monoclinic polymorph (figure 2.3a) the molecular planes of two adjacent molecules are almost normal to each other, thus yielding no $\pi - \pi$ stacking at all;

- in the triclinic polymorph (figure 2.3b) the molecular planes of adjacent molecules are all parallel but also laterally shifted with respect to each other, leading only to a partial superposition of their π orbitals in the stacking direction;

- in the orthorhombic polymorph (figure 2.3c) the molecules are arranged in the so-called herringbone packing, with an almost complete $\pi - \pi$
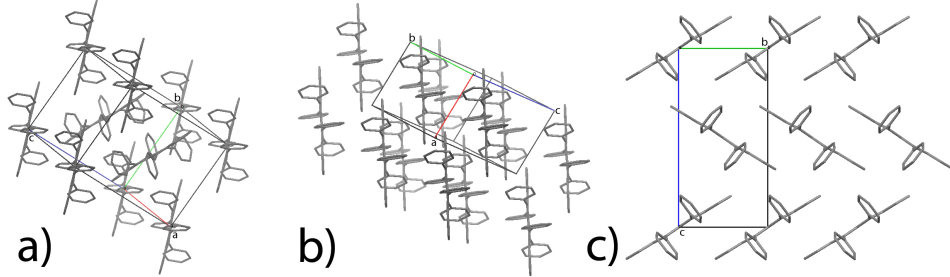
Figure 2.3: Arrangement of molecules in the three known rubrene polymorphs: monoclinic (*a*), triclinic (*b*), orthorhombic (*c*). The three structures are observed in a direction normal to the orientation of the long axis of the molecules, in order to easily show the amount (if any) of $\pi - \pi$ stacking between adjacent molecules. Hydrogen atoms are not shown for clarity.

Parameter	Value
Space group	*Cmca*
a [Å]	26.86(1)
b [Å]	7.193(3)
c [Å]	14.433(5)
Volume [Å^3]	2788.5(18)
Z	4

Table 2.1: Unit cell parameters of orthorhombic rubrene collected at 293 °K, as reported in [46].

stacking in the **b** lattice direction.

Rubrene crystals in the orthorhombic phase are easier to obtain, even with sizes up to some centimeters and they are also the ones that show the best transport properties, most likely due to the higher degree of $\pi - \pi$ stacking with respect to the other two polymorphs, as will be discussed in more details in the following sections[14, 48]. This is why we will now focus our discussion on the orthorhombic polymorph.

In Table 2.1 the cell parameters of a rubrene orthorhombic crystal grown by physical vapor transport at ambient temperature (293 °K) are reported, while in figures 2.4b and c its unit cell is shown, as viewed along the **b** and **c** axis, respectively[46].

It can be noticed that along the **a** axis the molecules are stacked in a simple layer by layer fashion, with the molecules of successive layers interacting only through their phenyl rings. This causes a strong anisotropy in the intensity of intermolecular interactions in the (*b,c*) plane with respect to those
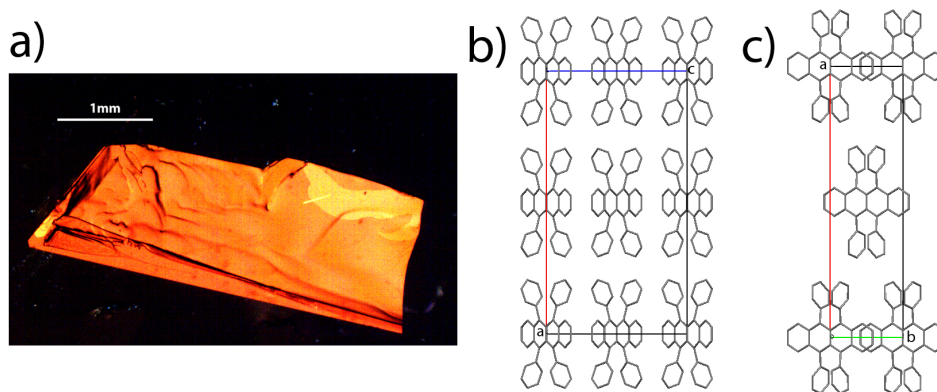
Figure 2.4: (*a*) Optical microscope photograph of a rubrene orthorhombic crystal grown by physical vapor transport. The exposed surface is the (1 0 0) one, while the thickness is of few μm. (*b*),(*c*) Orthorhombic rubrene unit cell observed along the **b** and **c** axis, respectively.

along the **a** lattice direction that in turn influences the growth dynamics of the crystals. Indeed, because of this rubrene orthorhombic crystals grown by physical vapor transport have an high aspect ratio and always expose the (1 0 0) surface, like the crystal shown in the optical microscope image reported in figure 2.4a.

When observed at an higher resolution, the surface of these crystals appears molecularly flat, usually with a few surface steps with the height of one or two molecular layers, directed along the **b** axis and well separated from each other.

2.4   Transport properties of crystalline rubrene

As already noted the interest toward rubrene is mainly motivated by its outstanding electrical transport properties. Indeed, since the first measurements of charge carriers mobility in rubrene single crystals have been reported, great efforts have been devoted toward the understanding of the actual mechanism behind charge carrier transport in rubrene and of the reason for such high mobility values.

Charge carriers mobility in rubrene orthorhombic single crystals can reach values as high as $40\,\mathrm{cm^2/Vs}$, a value comparable to that found for amorphous silicon[14, 15]. As for most organic crystals, electrical transport in crystalline rubrene is strongly anisotropic, with the larger mobility values measured along the **b** lattice direction. This is shown in the polar plot of
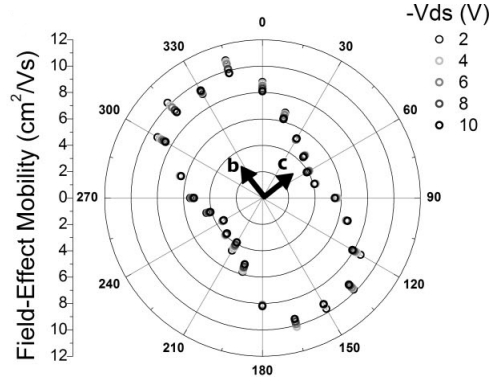
Figure 2.5: Polar plot showing the field-effect mobility values of a rubrene single crystal measured along various directions in the (b,c) plane. The **b** and **c** lattice directions are labeled on the plot. The different symbols indicate mobility values determined for different source-drain voltages of the field-effect transistor fabricated for the measurements. From [49]

mobility values measured in the (b,c) plane of a rubrene single crystal reported in figure 2.5[14, 49]. Rubrene, like most organic semiconductors, is also a unipolar p-type material, since the reported high mobility values regard only hole transport, while electron mobility is smaller by several orders of magnitude[50].

The lattice direction of maximum mobility corresponds to the direction of the $\pi - \pi$ stacking of the rubrene molecules (see also figure 2.3c). This fact strongly suggests that the conduction mainly originates from the overlap of molecular π orbitals. Indeed, the perfect alignment along the short molecular axis between adjacent rubrene molecules is not found in the case of other similar materials with a similar molecular structure and crystalline packing, but worse charge transport properties (e.g. tetracene or pentacene, whose molecules are instead slightly displaced along the short molecular axis)[42, 51]. The role of $\pi - \pi$ stacking in the electrical transport properties of orthorhombic rubrene has also been confirmed by measuring mobility as a function of the pressure applied to the crystal, showing that to an increasing pressure, and thus to a decreasing of the intermolecular distances, corresponds an increase in mobility[52].

The strong anisotropy in the transport properties of rubrene single crystals suggests that the main conduction mechanism in these systems is band-like transport. Even if there is still some debate whether this picture is correct or not, other strong pieces of evidence in its favor have been re-
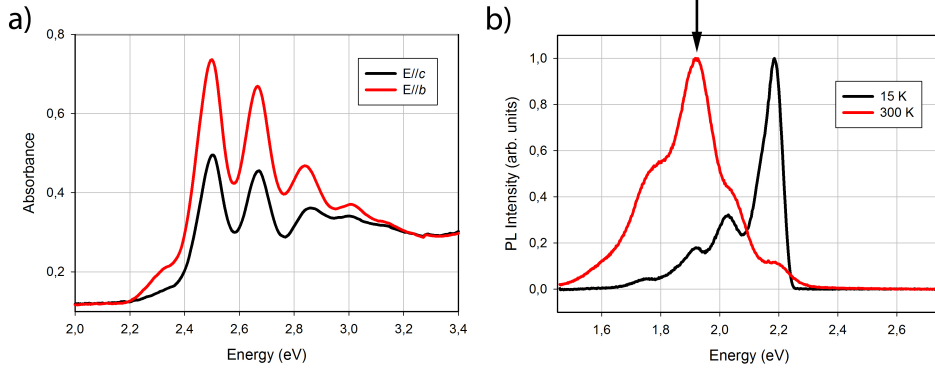
Figure 2.6: (*a*) Absorption spectra of a rubrene single crystal collected at normal incidence on the (*b*,*c*) surface and with light polarized along the **b** lattice direction (*black*) and **c** lattice direction (*red*). (*b*) Photoluminescence spectra of a pristine rubrene crystal collected at normal incidence on the (*b*,*c*) surface and with an excitation wavelength of 473 nm at 15 K (*black*) and 300 K (*red*). The arrow indicates the 650 nm PL peak attributed to crystal defects (see also section 2.6).

ported: the low amount of traps and scattering centers in bulk rubrene single crystals, the results of Hall effect measurements, the inverse dependence of the mobility on temperature up to temperatures as high as 300 K, Seebeck effect measurements on rubrene FETs, direct measurements of the HOMO band dispersion and UPS (ultraviolet photoelectron spectroscopy) measurements[14, 53–57].

2.5 Optical properties of crystalline rubrene

The normal incidence absorption spectrum and photoluminescence (PL) spectrum of a rubrene single crystal exposing the (1 0 0) surface are reported in figures 2.6a and b, respectively. The absorption spectrum, reflecting the molecular packing in orthorhombic rubrene, in which the molecules have an herringbone packing motif, with their short axes (M) all parallel to the **a** lattice direction, is strongly anisotropic, with maximum absorption in the visible range for light polarized along the **b** lattice direction. Apart from this anisotropy, the spectrum strongly resembles that of the single molecule, as expected for an organic crystal in which the intermolecular interactions are extremely weak. The absorption spectra are characterized by the vibronic progression with main peaks at 2.50 eV, 2.67 eV and 2.86 eV, attributed to b- and c-polarized vibronic transitions originating from the second, LN-polarized, molecular transition (where the L and N molecular axes lie in the

(b,c) crystal plane). The shoulder at $2.32\,eV$ has instead been attributed in the literature to the a-polarized lowest energy optical transition of the crystal, originating from the M-polarized molecular transition, and thus is only barely visible in the normal incidence spectra, probably due to crystal imperfections[58, 59].

The PL spectrum of a rubrene single crystal shows two clear bands at $2.04\,eV$ and at $1.9\,eV$, attributed to the transition between the lowest LUMO vibrational level and the lowest HOMO vibrational level and to the first replica of its vibronic progression, respectively[60]. More insights into the properties of the rubrene PL spectrum will be given in section 2.6

In addition to their extremely high charge carrier mobility, one of the most outstanding features of rubrene single crystals is their huge photoconductivity, with a photocurrent generation efficiency close to unity[16, 61]. The actual reason for this behavior has not been clarified yet, but there is strong evidence toward an ensemble of factors all contributing to this result.

Najafov *et al.* have shown, by studying the photocurrent dynamics in rubrene single crystals after their exposure to a short light pulse, that photoconductivity in rubrene single crystals is mainly due to free charge carriers that are released from a long-lived intermediate state $\approx 100\,\mu s$ after the excitation pulse[16, 61]. In that and subsequent works it has also been shown that this process of delayed conversion of photoinduced excitons into free charge carriers is mainly limited to the surface region of the crystal, where it occurs with an efficiency close to one[16, 17, 62]. This last result seems to suggest a role of surface related states in the photoconductivity of rubrene single crystals, a topic that will be addressed in more depth in the next section.

More evidence has been given that in rubrene single crystals triplet excitons with a lifetime of $(100 \pm 20)\mu s$ are generated with a large quantum yield efficiency[63]. The large yield for triplet generation, along with the coincidence of their lifetime with the delay of free carriers generation, suggests that the origin of photocurrent in rubrene is actually the dissociation of these long-lived triplet excitons into couples of charge carriers that are free to move toward the electrodes.

The reason behind the large quantum yield for triplet exciton generation in crystalline rubrene has been recently demonstrated to be singlet fission[64]. It is a spin-allowed process in which a single excited molecule shares its
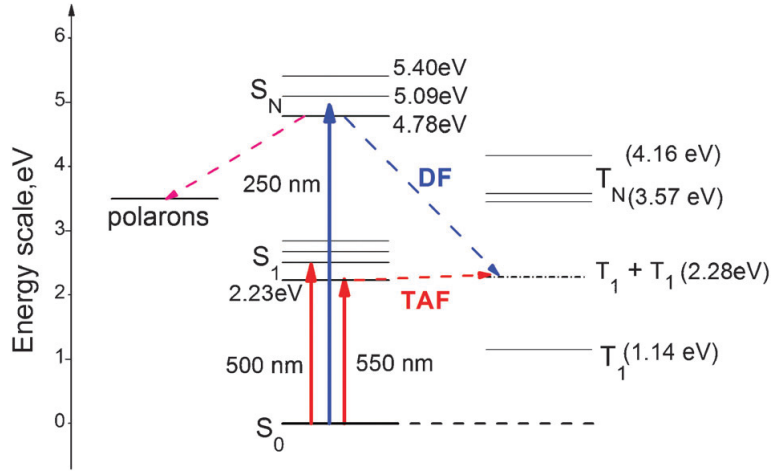
Figure 2.7: Scheme of the energy levels and transitions involved in the singlet fission process in a rubrene single crystal. TAF indicates *thermally activated fission* and DF indicates *direct fission*. From [64].

excitation energy with a neighboring molecule in its ground state, leading to the formation of a couple of triplet states[65]. The main condition for this process to be predominant in a molecular crystal, which is quite infrequent, is that the energy of the lowest singlet excited state S_1 must be almost exactly twice the energy of the lowest triplet excitation energy T_1. This is realized in the case of orthorhombic rubrene, where $S_1 = 2.23$eV and $T_1 = 1.14$eV, as shown in figure 2.7, where the energy levels of crystalline rubrene relevant for the singlet fission process are reported. Thanks to singlet fission the efficiency of carrier photogeneration can theoretically extremely high values, leading to higher limits for the maximum efficiency of organic photovoltaic cells and thus motivating the interest toward this topic.

Finally, another outstanding property of excitons in orthorhombic rubrene is their extremely large diffusion length. Najafov *et al.* have shown by photoconductivity measurements that the exciton diffusion length in crystalline rubrene is in the range of $3 \div 8$ µm, making it possible for excitons generated in the whole absorption region to reach the surface, where they dissociate into free charge carriers leading to generation of photocurrent[17]. By direct imaging of exciton diffusion, as shown in figure 2.8, other authors have confirmed the large diffusion length of excitons in rubrene crystals, showing at the same time the presence of a strong anisotropy in the diffusion length, particularly large along the **b** lattice direction, i.e. along the same lattice
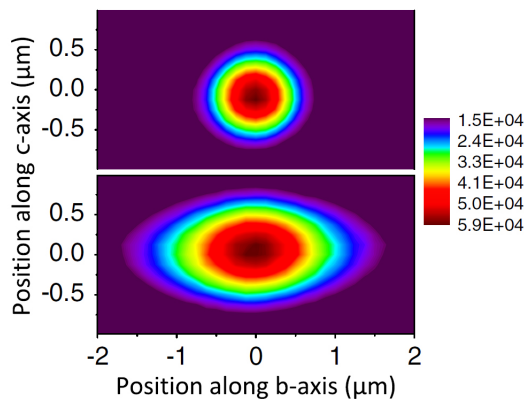
Figure 2.8: Contour plot showing the excitation intensity distribution (*top*) and the PL intensity distribution (*bottom*) on the (*b,c*) surface of a rubrene single crystal. From [66]

direction for which charge carrier mobility reaches its maximum values[66].

2.6   Oxidation of crystalline rubrene

As already noted in section 2.2 rubrene molecules are strongly affected by oxidation. The understanding of the dynamics and effects of this process on the properties of crystalline rubrene is thus mandatory.

The main source of contaminants and defects in crystalline rubrene is the presence of impurities in the source material which are incorporated during the crystal growth; rubrene peroxide have been shown to be the dominant impurity in commercial rubrene powder, and the presence of small amounts of oxygen in the inert gas flow used for crystal growth has been shown to increase the amount of such impurities in the as-grown crystals[67, 68]. Purification of the source material through several sublimation cycles and a carefully controlled growth environment are thus mandatory in order to get high quality samples in a reproducible manner.

A study of the post-growth oxidation of crystalline rubrene exposed to ambient conditions for several days has been carried out by mass spectrometry[19]. In figure 2.9 the concentration of rubrene peroxide molecules in rubrene thin films of different crystalline quality as a function of depth is reported. While in amorphous or dendritic films a large amount of rubrene peroxide is found even in the deeper layers, in rubrene crystallites it is present only in the first layers. The most likely reason for this behavior is that in
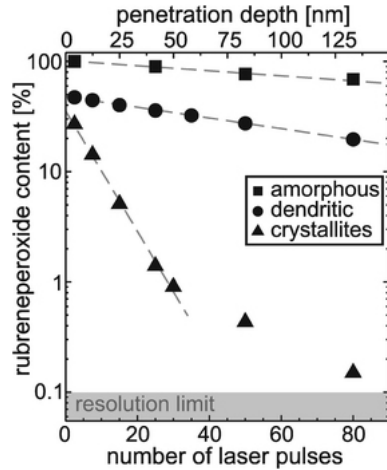
Figure 2.9: Depth profiles of rubrene peroxide concentration in rubrene thin films with different degrees of crystallinity as determined by mass spectrometry. From [19].

crystalline rubrene there is less room for the molecular conformational change upon rubrene peroxide formation. Nonetheless this result demonstrate the presence of a non negligible amount of rubrene peroxide even in the first few layers of rubrene crystals exposed to air. This has also been confirmed by Mitrofanov *et al.*, comparing the PL spectra of pristine rubrene single crystals with those of rubrene single crystals oxidized on purpose by exposing them to a pure oxygen atmosphere for several hours[69]. The PL spectra collected at various temperatures, reported in figure 2.10a and referring to pristine (*left*) and oxidized (*right*) samples, show a clear change of the PL bands upon oxidation, in particular with the appearance of a band around 650 nm, attributed to the electronic transitions from a bandgap state induced by rubrene peroxide. By two-photon spectroscopy the authors have also been able to measure the PL spectra of the oxidized samples as a function of depth in the crystal. The results, reported in figure 2.10b, show that the rubrene peroxide PL band is present only in the spectra collected from the sample surface, while the spectra collected from the bulk resemble those of pristine rubrene crystals, in agreement with the mass spectrometry data previously discussed.

The actual origin of the 650 nm PL band, which is often related to oxygen induced bandgap states, is however still unclear. Recently Chen *et al.* have carried out a systematic study on this particular band and their findings suggest that it actually originates from amorphous inclusions in rubrene
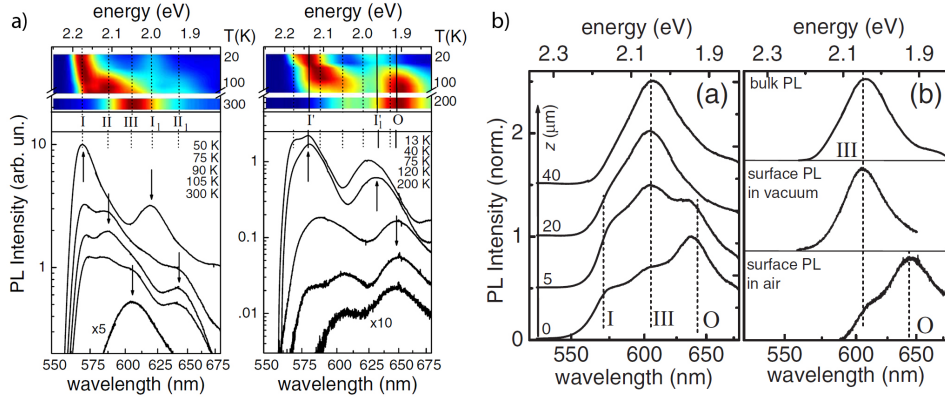
Figure 2.10: (*a*) PL spectra collected at various temperatures from an as-grown rubrene single crystal (*left*) and an oxidized rubrene crystal (*right*). The arrows indicate the characteristic PL bands of as-grown samples (*left*) and oxidized samples (*right*). (*b*) On the left are reported the normalized PL spectra of an oxidized rubrene crystal taken at various depths, on the right are reported the PL spectra taken from the bulk of an oxidized sample (*top*), from the surface of an as-grown sample (*centre*) and from the surface of an oxidized sample (*bottom*). From [69].

single crystals and is not directly correlated to oxidation[70]. This conclusion contradicts the observations reported in the previous paragraph and do not seem to be compatible with the results recently reported by Irkhin *et al.*, that noticed a strong polarization of this band thus excluding any amorphous phase as its origin[60, 69]. The existence of a bandgap state induced by oxygen at an energy level compatible with the 650 nm PL band has also been confirmed independently by means of *temperature-dependent space-charge limited current* spectroscopy, and is in agreement with the results of theoretical calculations[30, 34].

The role of rubrene peroxide in the transport properties of rubrene single crystals is also still subject to debate and up to now evidence of both a detrimental and an enhancing effect of oxidation on the transport properties of rubrene has been reported[31, 32, 69, 71]. Some authors have shown a significant improvement on conductivity and photoconductivity of rubrene upon oxidation, as shown in figure 2.11a, where a comparison between the I-V curves of pristine and oxidized rubrene single crystals is reported along with a comparison between their photoelectric responses, showing a huge increase in both conductivity and photoconductivity of oxidized rubrene crystals[69]. Furthermore Zhang *et al.* have been able to observe reversible increase and decrease of charge carrier mobility in rubrene single crystals by exposing their
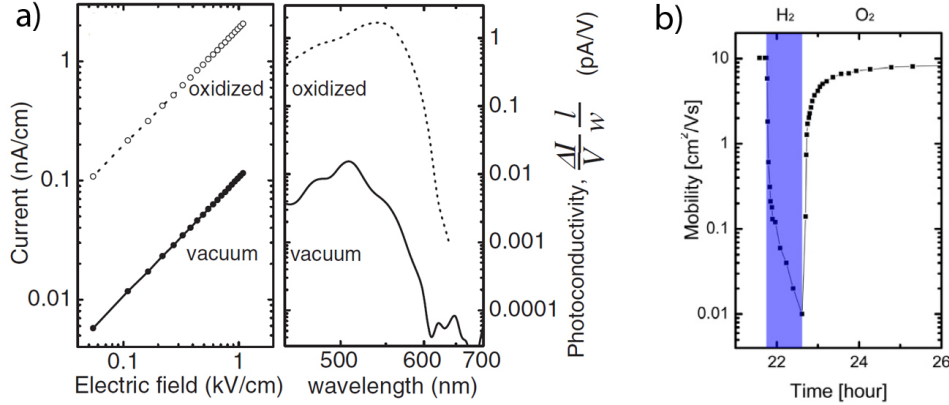
Figure 2.11: (*a*) Dark I-V curves measured from oxidized and non-oxidized rubrene single crystals (*left*) and photocurrent spectral responses of the same samples (*right*). From [69]. (*b*) Charge carrier mobility of a rubrene single crystal as a function of exposure time of its surface to hydrogen and oxygen. From [31].

surface to a pure oxygen atmosphere and to a pure hydrogen atmosphere, respectively[31]. They first exposed the surface of rubrene single crystals to pure oxygen, noticing a clear increase in mobility, and then introduced pure hydrogen in the experimental chamber, measuring a steep decrease in the mobility. By exposing the crystals once again to oxygen the starting mobility value could then be recovered, demonstrating both the relevant role of oxidation and the reversibility of the reaction. A plot exemplifying this behavior is shown in figure 2.11b.

On the other hand Najafov *et al.* have shown in [32] that in organic single crystals exposed to light and oxygen at the same time there is a clear decrease in photoconductivity with increasing oxygen exposure time. The authors attribute such an effect to an increase of the trap density in the crystal due to oxygen diffusion.

Finally, a prominent role of oxygen related defects in the enhanced free charge carriers production from long lived excitons in the surface region of rubrene crystals, accounting for their large photoconductivity, has been suggested several times[62].

2.7   Growth of rubrene thin films

Single crystals are often the best choice for the study of the intrinsic properties of a material, since they represent ideal solid samples and can be easily

grown in a reproducible way and with high structural quality. Nonetheless, in order to exploit rubrene in the fabrication of electronic devices, it is necessary to grow it in the thin film form, in order to meet the current industrial standards for device miniaturization. Moreover, the large anisotropy in the optical end electrical properties of crystalline rubrene requires a high control over the crystalline structure of the thin films, possibly with a single orientation.

Despite this, up to now only few attempts to grow crystalline rubrene thin films have succeeded. Most of the times the attempts to grow rubrene thin films with standard solution or evaporation methods led only to amorphous films[20, 21]. In particular there have been several attempts to grow rubrene thin films on SiO_2, which is a standard dielectric for most electronic applications, but up to now it has been possible to grow high quality crystalline thin films only by previously depositing a pentacene buffer layer on top of the bare SiO_2 substrate[19, 25, 72]. Other successful attempts to obtain rubrene crystalline thin films on SiO_2 substrates are based on the abrupt heating at $100\,°C$ of previously deposited amorphous films[26]. By these means it has been possible to obtain highly crystalline thin films with their **a** axis normal to the substrate surface, but constituted by grains of about $80\,\mu m$ in size and with a random in-plane orientation of their **b** and **c** axes.

Other successful attempts of rubrene crystalline thin films growth have exploited epitaxial growth on other inorganic substrates such as Au or Bi or on organic single crystals like tetracene[27, 73, 74]. By these means it is generally possible to have a greater control over the structural properties of the grown film, but the presence of an interface with another organic semiconducting material generally leads to complications in interpreting the results of optical and electrical measurements carried out on these systems.

2.8   Conclusions

As discussed in the previous sections there are still several open problems regarding both the intrinsic properties of rubrene and the preparation of working devices. In the next chapters we will thus describe both the results of our work aimed at growing crystalline rubrene thin films and of our experiments aimed a deeper understanding of the process of oxidation of crystalline rubrene; in addition, we will focus on the effects of this oxidation

process over rubrene optical and electrical transport properties.

Chapter 3

Experimental techniques

The experimental work described in this thesis required the use of a wide variety of sample preparation and measurement techniques, that will all be introduced in this chapter, along with the principles behind their functioning, when relevant for the results presented in the following chapters. The sample preparation techniques include the growth of single crystals and epitaxial thin films of rubrene and other organic materials; the characterization techniques that will be described in the following sections instead include various atomic force microscope based techniques and structural characterization by means of X-ray diffraction.

3.1 Sample preparation

3.1.1 Crystal growth

The most efficient and reproducible method to grow organic molecular crystals of oligoacenes such as rubrene or tetracene is the *physical vapor transport* (PVT) method[75, 76]. In figure 3.1 the scheme of the apparatus used to grow crystals using such a system is reported in its vertical configuration. In our case, the apparatus used to grow crystals with the vertical physical vapor transport method consists of a quartz tube with a closed extremity and with two openings at the other extremity. On the bottom of the tube a crucible is placed containing the starting material for the growth of the crystal. A smaller tube, inserted from the topmost opening of the larger tube is used to convey an inert gas flux (usually He, Ar or N_2) toward the source material. The gas is then expelled through a second opening
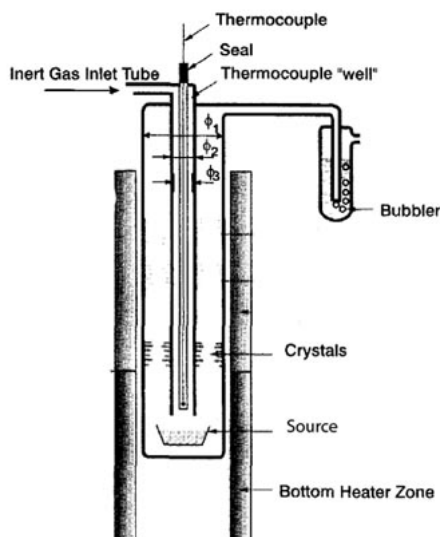
Figure 3.1: Scheme of the apparatus used to grow organic molecular crystals by the physical vapor transport method in the vertical configuration.

placed near the top of the larger tube. The crucible is then heated at a fixed temperature, controlled thanks to a thermocouple, reaching the sublimation temperature of the source material. A temperature gradient is established along the tube thanks to a proper dissipation system. Due to this gradient the heated molecules, transported toward the top of the tube by the inert gas flux, deposit on the walls of the inner or of the outer tube, leading to the formation of crystals whose size and shape will depend on the exact growth conditions, as described in the following. In general it is possible to distinguish between four different regimes for the transport of the sublimed molecules. Figure 3.2 shows the three possible regimes corresponding to a condition in which the inert gas flux is zero. Such regimes, corresponding to increasing values of the inert gas pressure, are tagged respectively as: molecular flow, diffusion and convection. When the flux is non-zero, then the regime is tagged as forced convection. In a situation where the flux is zero and the pressure is less than 15 Torr, i.e. in the molecular flow and diffusion regimes, there is a large number of nucleation centers due to the high speed of the molecules, thus leading to the formation of negligibly small crystals. At pressures higher than 15 Torr transport is a little slower and crystals with a size of the order of some μm can form. Nonetheless there are still so many nucleation sites that there is a large probability that neighbor-
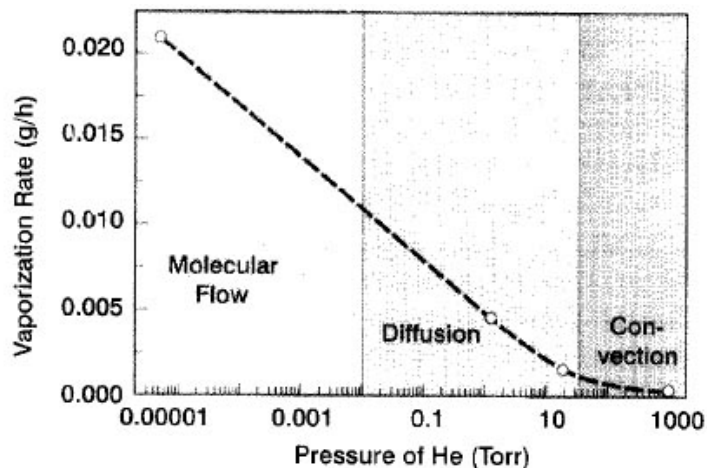
Figure 3.2: Vaporization rate as a function of the inert gas pressure (in this case He) with the source at constant temperature. Only the three possible regimes for a zero gas flux are shown here.

ing crystals coalesce, leading to the formation of larger crystals with a large number of defects. If a non-zero flux of the inert gas is used, instead, the convection due to the thermal gradients along the tube dominates over the forced convection of the gas flux. In this case one can easily obtain larger crystals (with a size up to few cm) with a good structural quality. Usually crystals of oligoacenes grown by this technique are very wide and thin (with an aspect ratio the order of 10^3). This is due to the peculiar characteristics of the intermolecular bonds between conjugated molecules. Indeed, as shown in chapter 1 the presence of the π orbitals, which are concentrated around specific areas of the molecules, leads to intermolecular bonds which are much stronger in specific directions with respect to others. Thus, the approaching molecules easily attach to the borders of the growing crystal, while the molecules landing on the surface of the crystal move along it until they reach the crystal border.

3.1.2   Thin film growth

Epitaxial thin films of high crystalline quality and with controlled properties can be grown by Organic Molecular Beam Epitaxy (OMBE)[40, 77], a technique based on Molecular Beam Epitaxy (MBE), which is nowadays widely used for the epitaxial growth of inorganic materials[78].

This technique consists in slowly depositing the sublimated molecules
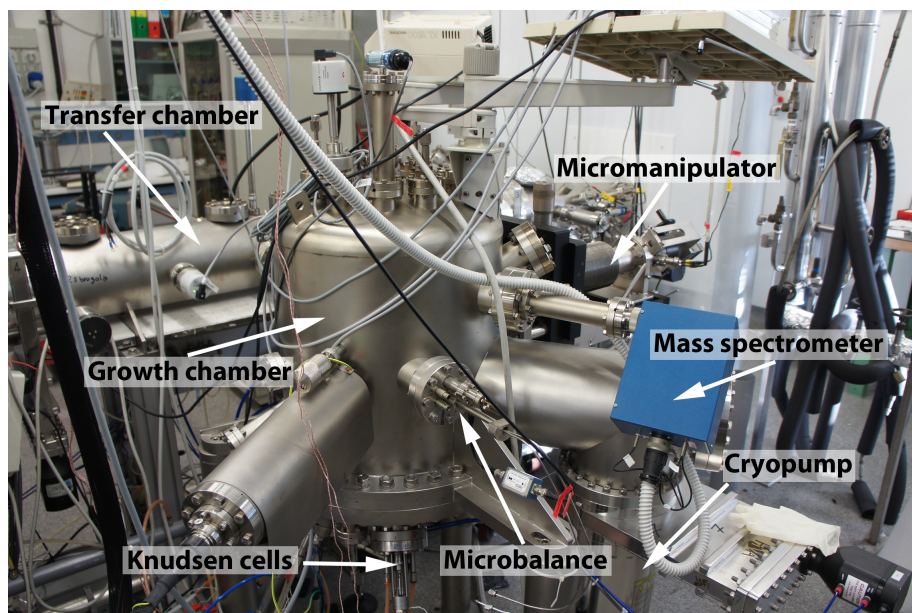
Figure 3.3: Photograph of the apparatus used for the epitaxial growth of thin films by the OMBE technique. In the picture are indicated: the deposition chamber, the micromanipulator, the cryopump, the Knudsen cells, the microbalance, the transfer chamber, and the mass spectrometer. The main chamber diameter is $\approx 50\,\mathrm{cm}$.

on the desired substrate in an ultra high vacuum (UHV) atmosphere ($\approx 10^{-9} \div 10^{-10}$ Torr). By these means it is possible to grow very thin films, with a thickness down to a fraction of a single layer, at really low deposition rates. One of the main advantages of this technique is the high control it gives over various growth parameters, such as the deposition rate, the substrate temperature and the source temperature. In figure 3.3 a photograph of the apparatus used for the epitaxial growth of thin films by the OMBE technique, with a labeling of the most important parts, is reported. The system consists of an introduction and transfer chamber, used to insert the clean substrate and to extract the sample after the deposition, and of the actual deposition chamber. The two chambers are separated by gate valves. The presence of an introduction chamber makes it possible to insert and remove the sample without bringing the larger deposition chamber to ambient pressure. The ultra high vacuum condition is reached in the deposition chamber only, thanks to the use of three different pumps in successive steps: a $20\,\mathrm{m^3/h}$ rotary pump, a $500\,\mathrm{l\,s^{-1}}$ turbomolecular pump and finally a $1500\,\mathrm{l\,s^{-1}}$ cryopump, shown in figure 3.3.

Inside the deposition chamber, where up to six different sources can be

mounted, all at a distance of 16 cm from the surface of the sample, the sample is placed with the surface looking downward. The sources consist of Knudsen cells, which consist in a crucible containing the material to be sublimated in powder form and whose temperature is controlled thanks to a filament heating system. After the sublimation temperature is reached, the shutter connecting the cell to the main chamber is opened and the molecular beam, highly collimated by a *liner* in order to not contaminate the whole chamber, form and is directed towards the sample surface.

The deposition rate and the nominal thickness of the deposited film (i.e. the thickness it would have if it uniformly covered the substrate surface) are monitored thanks to a quartz microbalance sitting right aside the substrate. An AC signal at 6 MHz is used to induce oscillation of the quartz crystal. Then, if the thickness of the deposited film is significantly lower than the wavelength of sound, the dependence of the oscillation period of the quartz crystal on the viscosity of the deposited material will be negligible and thus the following equation will apply

$$T = \frac{N_q d_q}{d_f} \left(\tau - \tau_q \right) \tag{3.1}$$

where T is the thickness of the deposited film, N_q is a constant with the dimensions of a frequency, d_q and d_f are the density of quartz and of the deposited material, respectively, and τ_q and τ are the oscillation periods of the crystal before and after the deposition, respectively[79]. Measuring the oscillation period of the quartz in real-time during the deposition and knowing the density of the deposited material it is thus possible to calculate the deposition rate and the nominal thickness of the film. Often, density is unknown, and 'nominal' film thicknesses are determined, i.e. referred to standard known materials.

The temperature of the sample during ad after the deposition can be controlled due to a cooling and heating system, while the microbalance is always kept at a fixed temperature by a water cooling system. Finally, the structural evolution of the film during the deposition can be monitored by a *reflectance anisotropy spectroscopy* (RAS) system, an *in situ* characterization technique based on the real-time monitoring of the reflectance anisotropy of the sample surface during the deposition[80].

3.2   Sample characterization

To carry out the work described in this thesis different characterization techniques have been used. Most measurements have been carried out either using an atomic force microscope (AFM) in one of its various working modes, or X-ray diffraction techniques (both with standard and synchrotron X-rays sources). These two techniques will thus be thoroughly described in the following paragraphs, along with the presentation of the relevant theoretical background. Other characterization techniques used for smaller parts of this work include electrical and optical measurements, whose experimental setup will be presented in the corresponding chapters.

3.2.1   Atomic Force Microscopy

AFM is one of the so-called Scanning Probe Microscopes (SPM), which also comprise Scanning Tunnel Microscope (STM) and Scanning Near-field Optical Microscope (SNOM). Its invention dates back to 1986; it is an instrument characterized by a great versatility, in that it presents a wide range of different operating modes[81, 82]. Unlike STM, its use is not limited to conductive materials, and can also be used in liquid environments. This makes the AFM a particularly useful instrument for the study of organic or even biological samples, which are often poorly conducting or insulating and may need to be kept in an aqueous environment[83–85]. A simple scheme of a generic AFM, showing all its fundamental components, is reported in figure 3.4. The probe used to image the surface of a sample is a tip, generally made of silicon or silicon nitride, with a curvature radius at the apex which is generally the order of tens of nm and a height of the order of tens of µm. The tip is placed on a flexible cantilever, which can bend both in vertical and horizontal directions and which are usually in a triangular or rectangular shape. Given the physical properties of the cantilever it is possible to extract the force acting on the tip from a measure of the deflection of the cantilever itself. In figure 3.5 the images taken with a scanning electron microscope (SEM) of a triangular cantilever along with the tip mounted on it are reported. The deflection of the cantilever is measured through a laser beam impinging on the back of the cantilever and reflected toward a photodiode divided into four quadrants. Measuring the difference in the signal intensity between the top and bottom parts of the diode or between the left and the
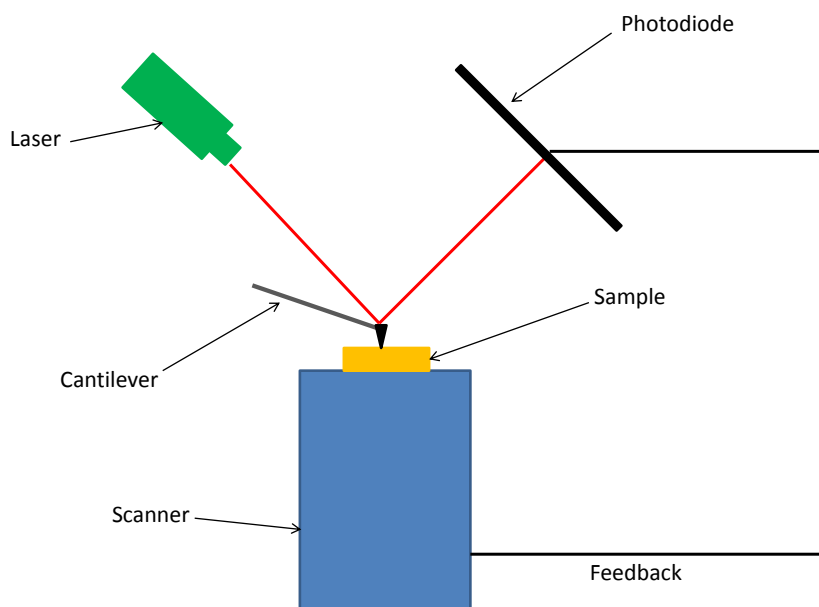
Figure 3.4: Schematic representation of a generic AFM with all its fundamental components.
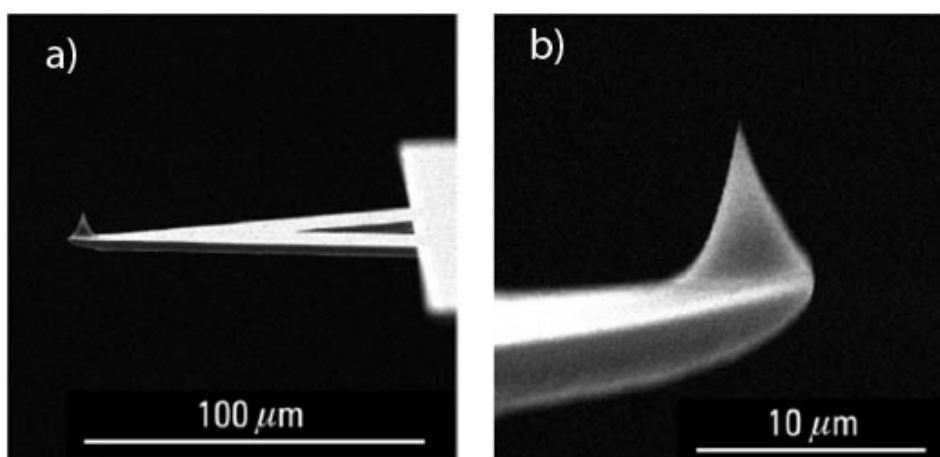
Figure 3.5: (a)SEM image of a triangular shaped cantilever and of the tip mounted on it. (b) Detail of the tip from image (a).
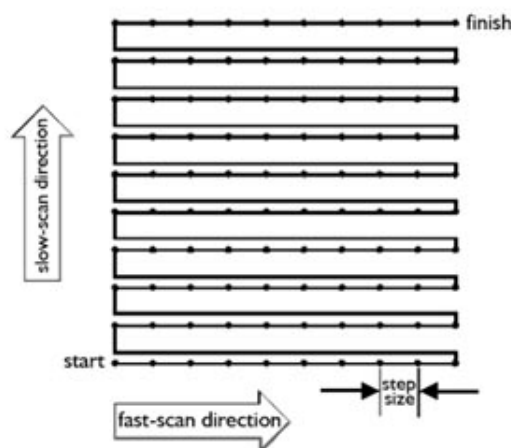
Figure 3.6: Scheme of the raster scanning mode of an AFM. The collected images are consituted by the assembly of the points collected during the scanning in the fast-scan direction.

right parts it is possible to obtain the amount of deflection in the vertical or horizontal direction, respectively.

The sample is mounted on a piezoelectric scanner, whose motion in the three dimensions can be controlled with nanometric precision by varying the applied bias. The AFM performs a raster scanning of the sample surface, as illustrated in figure 3.6. The angle between the fast-scan direction and the long axis of the cantilever can be changed at will, in order to achieve the desired experimental conditions. Finally, a feedback circuit is present, making it possible to readjust the scanner vertical extension in function of the cantilever deflection, as will be explained with more details in the following paragraphs.

Base working modes

The two main AFM working modes are the *contact* and *semi-contact* (also called *tapping*) modes. Choosing one of these two working modes it is possible to obtain information about the topography, the chemical composition, various physical properties and the orientation of the single crystalline domains constituting a crystalline thin film. It is also possible to obtain molecular resolution images of a crystalline surface. In general the interactions between the AFM tip and the sample surface are due to contributions from a wide range of different forces, among which the main ones are:
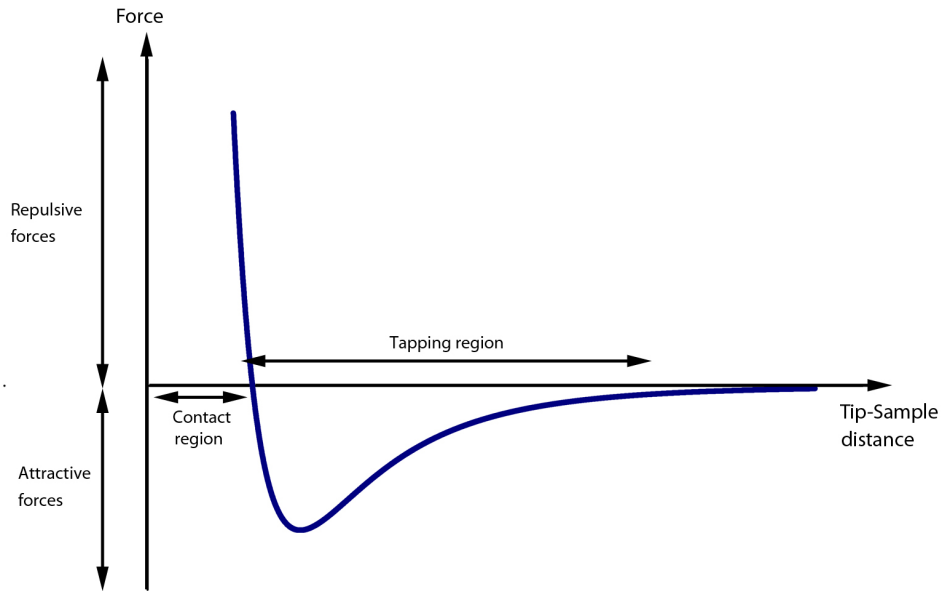
Figure 3.7: Plot of the tip-sample interaction potential as a function of the tip-sample distance. For the different ranges of tip-sample distance the corresponding AFM working modes and the kinds of the preponderant tip-sample interactions are indicated.

- Van der Waals forces

- Short-range repulsive forces

- Capillary forces

- Electrostatic and magnetic forces

The cantilever deflection is due to the sum of all these forces, which can then be measured knowing the elastic constant of the cantilever. As shown in figure 3.7, depending on the AFM working mode in use and more generally on the tip-sample distance, different kind of forces can dominate the tip-sample interaction from time to time. The calculation of the exact amount of the combination of all those interactions is in general quite complex, but for the general use of an AFM this is not necessary, and thus it won't be described in more detail. The maximum resolution of an AFM is determined by various factors. First of all, it is necessary to distinguish between lateral and vertical resolution. Indeed, the vertical resolution is only limited by the precision of the vertical movements of the scanner. The best attainable resolution with

the scanner used in this work is 0.1 nm. The maximum lateral resolution is instead determined by the tip size and curvature. An AFM tip has generally a rounded apex, whose curvature radius is, for the most commonly used tips, around 50 Å. This leads to a limit resolution of around 20 Å at best, since only a part of the tip interacts with the sample.

In contact mode the tip is brought to a distance from the sample surface for which the tip-sample interaction is of the repulsive kind. When, during scanning, the tip encounters a protrusion or a valley on the surface, the tip-sample distance and thus the cantilever deflection vary. In response to the change of the cantilever deflection, the feedback circuit vary the vertical position of the scanner, in order to restore the original cantilever deflection. Standard AFM topographic images are constructed by mapping the variations in the vertical extension of the scanner as a function of the tip position over the sample surface. In figure 3.8a an AFM height image collected in contact mode is reported, in which the grays scale is used to represent the relative height of each point. In figure 3.8b the grays scale is instead used to represent the cantilever deflection in each point. The color of this image is uniform with the exception of the steps present on the surface, since the feedback circuit reacts to the change in the cantilever deflection in correspondence of a step, restoring it to the original value. It can also be observed that the second image corresponds to the first derivative of the first one. With an AFM working in contact mode it is possible, in parallel to the aquisition of height images, to get images conveying further information such as: the presence of regions with different chemical or physical properties (Lateral Force Microscopy, LFM), the orientation of the surface crystalline domains (Transverse Shear Microscopy, TSM) or molecular resolution images[84, 86–89].

The intensity of the tip-sample interaction during scanning in contact mode is large enough to damage the surface of the softer samples, such as most organic materials. Even if the interaction with the tip can be significantly reduced, for example by working in dry nitrogen atmosphere in order to remove the contribution from capillary forces, it is better, if working in contact mode is not absolutely necessary (for example in order to obtain molecular resolution images), to make use of a complementary technique, called *semi-contact* mode. In tapping mode the cantilever is forced to oscillate at a frequency ν close to its resonant frequency, thanks to a piezoelectric element placed in the tip holder. The tip-sample distance is then adjusted to
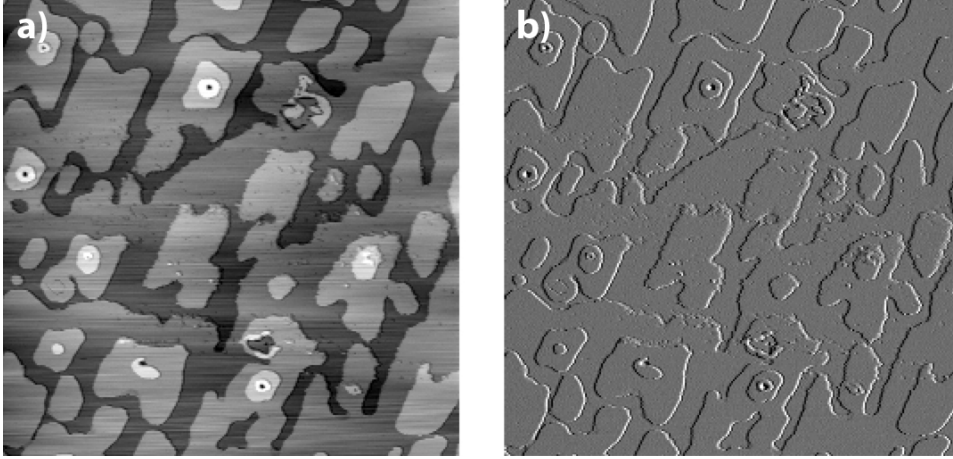
Figure 3.8: Contact mode AFM image of the surface of a (3×3) µm^2 region of a rubrene thin film grown on top of a rubrene single crystal. (*a*) Height image in which lighter grays correspond to higher regions of the surface. (*b*) Deflection image collected on the same region, in which the grays scale is used to represent the cantilever deflection in each point.

a value such that, during each oscillation, the tip passes from a non-contact regime to a contact regime, and then back to a non-contact regime.

Variations in the average tip-sample distance lead to variations of the root mean square (RMS) oscillation amplitude of the cantilever. Thus, if during the scanning the tip encounters a valley or a protrusion on the sample surface there is a variation in the RMS oscillation amplitude of the cantilever. In analogy with what happens for contact-mode measurements, the feedback circuit restores the initial oscillation amplitude by varying the vertical extension of the scanner. A morphological image of the surface can then be reconstructed by assigning to each image pixel the corresponding value of the scanner vertical extension. Height and amplitude images collected in tapping mode would look exactly like the height and deflection images reported in figure 3.8 and collected in contact mode.

Since in tapping mode the AFM tip is in contact with sample surface only in the lowest point of the cantilever oscillation, the duration of the tip-sample interaction is minimized with respect to contact mode. This leads to the main advantage of tapping mode over contact mode measurements, i.e. minimum sample damage due to tip-sample interactions.

During the scanning of a surface in tapping mode it is also possible to collect phase-contrast images, in addition to height images, constructed

by representing for each pixel the corresponding phase shift between the oscillation of the cantilever and the forcing oscillation. This imaging mode is based on the assumption that the energy dissipated by the tip during each oscillation is linked to the phase shift through the equation

$$\overline{E}_{tip} = \frac{1}{2} \frac{kA^2\omega_0}{Q_{cant}} \left[\left(\frac{A_0}{A} \right) \sin\varphi - 1 \right] \tag{3.2}$$

where $\overline{E}_{tip}$ is the average energy dissipated by the tip, k, ω_0 and Q_{cant} are parameters depending on the cantilever properties and A and A_0 are the oscillation amplitudes of the cantilever and of the forcing oscillation, respectively[90]. This relation leads to the consequence that if the oscillation amplitude is kept fixed by the feedback circuit, then also the value of φ do not change unless there is a change in the energy dissipated during the oscillation. This means that a phase contrast is observed only between regions of the sample over which the energy dissipated by the tip during the oscillation is different and, since the amount of dissipated energy depends in general on the properties of the material under the tip, a contrast between two regions in the phase image corresponds to a difference in the composition of the regions themselves. Thus, collecting phase contrast images it is possible to distnguish between regions of a sample made of different materials, even if they display the same morphology; this is exemplified in figure 3.9, where an height and phase contrast image of the same region of a sample covered by two different materials are shown. In this case the brighter areas in the phase contrast image corresponds to rubrene islands, while the darker regions correspond to quatertiophene islands.

Kelvin Probe Force Microscopy

With Kelvin Prove Force Microscopy (KPFM) it is possible to measure the work function or surface potential of a sample with sub-micrometric resolution, while at the same time collecting morphological images of the surface[91–93]. In order to carry on a KPFM measurement a conductive AFM tip is scanned over the surface of the sample at a constant distance from the surface of a grounded sample, while an AC signal is applied to the tip itself. The tip will then oscillate at the same frequency of the applied bias V_{ac} due to its electrostatic interaction with the sample surface. An additional DC signal is then applied to the tip through a feedback loop in
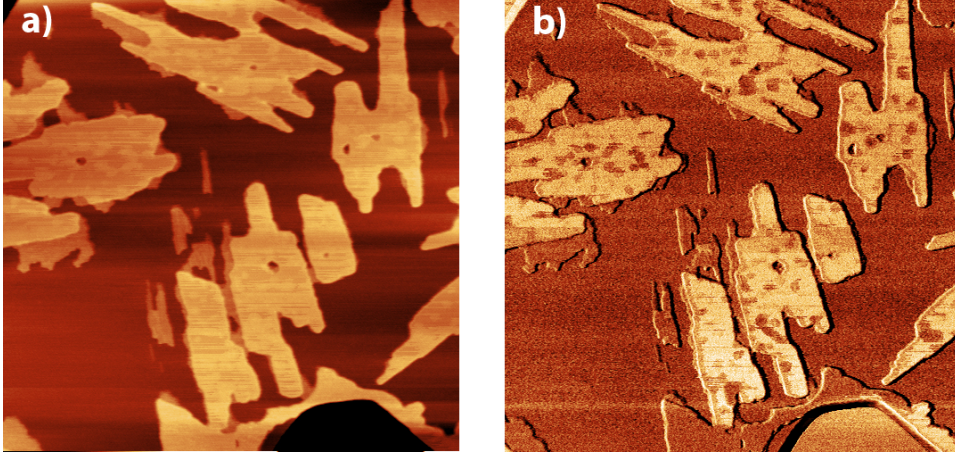
Figure 3.9: AFM tapping mode images of a 3×3 µm^2 region of the surface of a sample consisting of a rubrene thin film grown on top of a quatertiophene thin film. (a) Height image. (b) Phase contrast image collected at the same time as (a).

order to minimize the tip-sample electrostatic interaction. The resulting voltage between the tip and the sample then is:

$$\Delta V = \Delta \varphi - V_{dc} + V_{ac} \sin(\omega t) \tag{3.3}$$

where $\Delta \varphi$ is the work function difference (or contact potential difference) between the tip and the sample, V_{dc} is the DC potential applied to the tip and ω is the frequency of the applied V_{ac} bias. If the tip-sample distance is smaller than the tip radius, then the tip-sample system can be considered as a parallel plate capacitor whose energy U is given by

$$U = \frac{1}{2} C \Delta V^2 \tag{3.4}$$

where C is the capacitance of the tip-sample system.

The electrostatic force between the tip and the sample is then given by

$$F = -\frac{\partial U}{\partial z} = -\frac{1}{2} \frac{\partial C}{\partial z} \Delta V^2 = F_{dc} + F_\omega + F_{2\omega} \tag{3.5}$$

where the three components of the force are

$$F_{dc} = -\frac{1}{2} \frac{\partial C}{\partial z} \left[(\Delta \varphi - V_{dc})^2 + \frac{V_{ac}^2}{2} \right] \tag{3.6}$$

$$F_\omega = -\frac{\partial C}{\partial z} \left[(\Delta\varphi - V_{dc}) V_{ac} \sin(\omega t) \right] \tag{3.7}$$

$$F_{2\omega} = \frac{1}{4}\frac{\partial C}{\partial z} \left[V_{ac}^2 \cos(2\omega t) \right] \tag{3.8}$$

From the expression for F_ω it follows that this component will be zero if $V_{dc} = \Delta\varphi$. Thus, extracting through a lock-in amplifier the ω component of the cantilever oscillation and finding the V_{dc} value applied through the feedback loop that zeroes this component, it will be possible to obtain a map of the value of $\Delta\varphi$, and thus of the work function, over the scanned area.

In order to maintain a constant distance from the sample surface during the collection of the KPFM image, the AFM is operated in the so-called *lift mode*, i.e. each scan line is scanned first in standard tapping mode in order to detect the height profile along it and then the same line is scanned once more in Kelvin Force mode exploiting the morphology signal collected during the previous scan to maintain a constant tip-sample distance.

One issue that should always be addressed when analyzing KPFM images is the fact that, due to the longer range of the electrostatic forces involved in KPFM with respect to those involved in standard tapping AFM measurement, the resolution is always lower than that reached in morphological images and that, for structures below a certain size, the measured surface potential is a convolution of the surface potential distribution of a large area under the tip with a proper transfer function describing the tip shape[94, 95]. Thus, depending on the features of the imaged area, the data should always be treated with specific methods before the real surface potential can be properly extracted. The method used in this work will be described in the chapter dedicated to the discussion of the results of the KPFM measurements (chapter 5).

Conductive Atomic Force Microscopy

Conductive Atomic Force Microscopy (C-AFM) is a contact mode technique in which a conductive AFM tip is used as an electrode, in order to apply a bias to the sample and to measure the current passing through it, as shown in the left part of figure 3.10. This technique has many advantages over STM measurements, in particular when dealing with organic materials. The two main advantages are the decoupling between the current measure-
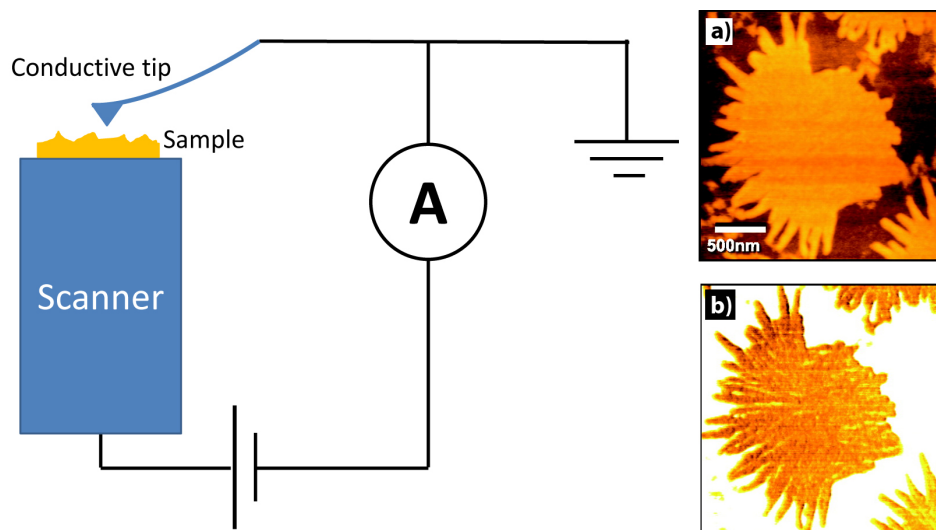
Figure 3.10: *Left*: scheme of a generic conductive atomic force microscope. *Right*: height (a) and current (b) AFM images of the surface of a SiO$_2$ crystal partially covered by D5TBA (4-(5""-Decyl-[2,2';5',2";5",2"';5"',2""] pentathiophen-5-yl)-butyric acid) crystalline islands. From [96]

ment and the control of tip-sample distance (while in a STM the tip-sample distance is controlled through the measured tunnelling current) and the possibility to carry on measurements also on poorly conducting materials (such as most organic semiconductors)[97].

C-AFM measurements can be carried out in two different ways: it is possible to either collect *I-V* curves by keeping the tip fixed in a point of the sample and measuring the current while sweeping the potential or to collect two-dimensional conductivity images by performing a scan at a fixed bias and measuring the current for each scanning point, while at the same time collecting ordinary topographical images. In figures 3.10a and b an example is shown of a C-AFM current image along with the corresponding height image, collected from the surface of a SiO$_2$ crystal partially covered by D5TBA (4-(5""-Decyl-[2,2';5',2";5",2"';5"',2""] pentathiophen-5-yl)-butyric acid) crystalline islands.

Also, two different configurations can be used: the horizontal one, in which an electrode is placed on top of the sample surface, thus probing conduction along the sample surface, and the vertical one, in which the electrode is placed on the back of the sample and the current thus flows in the vertical direction.

In order to interpret the results of a C-AFM measurement it is of critical importance to understand the nature of the contact between the tip and the sample surface, since its geometry is in general more complicated than that of a planar electrode. In order to do so one has to keep into account various factors, such as the tip shape, the stiffness of the surface, the pressure exerted by the tip, the contact area and the tip coating material. Various models have been proposed to evaluate the effect of these aspects, depending on the experimental conditions. Our treatment of this problem will be described later, along with the analysis of the collected data.

Instruments used for this work

The AFM used for this thesis work is a Veeco Nanoscope Multimode V, equipped with various extension modules which permit to exploit all the imaging techniques described in the previous paragraphs. It is equipped with two different piezoelectric scanners: an E scanner, with maximum scanning area of 14×14 µm^2, and a J scanner, with maximum scanning area of 140×140 µm^2.

Images can be collected at different resolutions, in terms of number of sampled points for each scan line, which vary between 128×128 pixels and 16384×16384 pixel.

The collected images have been corrected and analysed with the Nanoscope software (version 7.30)[98] and the open-source program Gwyddion (version 2.29)[99].

3.2.2   X-ray Diffraction

X-ray diffraction (XDR) is the technique of choice to gain information about crystal structure, since X-ray wavelength is comparable to the inter-atomic distances in solids.

In general, X-rays scattered by atoms arranged in a periodic lattice will give rise to specific intensity patterns due to interference effects between rays scattered by different atoms. From such diffraction patterns it is then possible to determine the arrangement of the diffracting atoms and thus the arrangment of the atoms in the crystalline lattice. With the periodicity of the crystal lattice as the only starting assumption, one can obtain the two following conditions for constructive interference of the diffracted rays[100,

101]: the Bragg equation

$$2d_{hkl} \sin \vartheta_B = n\lambda \tag{3.9}$$

and the Laue condition

$$\mathbf{Q} = \mathbf{K} - \mathbf{K_0} \tag{3.10}$$

where d_{hkl} is the interplanar spacing between the (hkl) lattice planes, i.e. the family of planes corresponding to the reciprocal space vector of components hkl, ϑ_B is called the *Bragg angle*, n is an integer number, λ is the wavelength of the diffracted ray, $\mathbf{K}$ and $\mathbf{K_0}$ are the wavevectors of the incident and the diffracted ray, respectively, and $\mathbf{Q}$ is a vector of the reciprocal lattice of the crystal.

Equation 3.10 means that in order to have non-zero diffracted intensity the change in wavevector of the X-ray following diffraction must be a vector of the reciprocal lattice.

The intensity of the diffracted X-ray beam does also depend on the electronic charge distribution surrounding the scattering atom and, in case of polyatomic structures, on the reciprocal position of the different atoms in the unit cell. This dependence is represented through the so-called *structure factor* $S_{\mathbf{K}}$, on which the diffracted intensity has a quadratic dependence and which is given by:

$$S_{\mathbf{K}} = \sum_{j=1}^{n} f_j(\mathbf{K}) e^{i\mathbf{K} \cdot d_j} \tag{3.11}$$

where n is the number of atoms in the unit cell, d_j is the position of the j-th atom in the unit cell and $f_j(\mathbf{K})$ is the so called *atomic form factor* of the j-th atom, given by

$$f_j(\mathbf{K}) = -\frac{1}{e} \int d\mathbf{r} e^{i\mathbf{K} \cdot \mathbf{r}} \varrho_j(\mathbf{r}) \tag{3.12}$$

where e is the unit charge and $\varrho_j(\mathbf{r})$ is the electronic charge distribution around the j-th atom.

Atomic form factors for all the elements have been calculated with high precision, and can thus be used as a mean to identify the different phases present in the sample by measuring the relative intensities of the diffraction peaks[102].
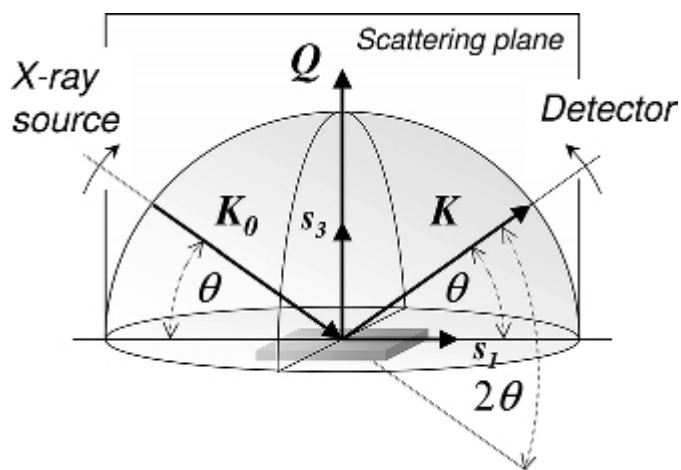
Figure 3.11: Experimental geometry for a $\vartheta/2\vartheta$ XRD measurement. From [103].

$\vartheta/2\vartheta$ measurements

The most common experimental geometry for XRD measurements on powders or thin films is the $\vartheta/2\vartheta$ setup, shown in figure 3.11. In this setup the sample is mounted in the center of the instrument and the X-ray beam is directed toward the sample forming an angle ϑ_{in} with the sample surface. The detector position is such that it measures the intensity of the beam scattered at an angle $\vartheta_{out} = \vartheta_{in}$ with respect to the surface. The scattering vector **Q**, which is always contained in the scattering plane formed by the incident and scattered beams, is thus parallel to the normal to the sample surface. Then, because of the condition over the scattering vector expressed in equation 3.10, the only detected diffraction peaks will be those corresponding the lattice planes oriented parallel to the sample surface, appearing at angles 2ϑ satisfying equation 3.9.

Grazing incidence X-ray diffraction

The penetration depth of X-rays in solids is usually in the range between 10 μm and 100 μm and thus, using the standard $\vartheta/2\vartheta$ measuring geometry, in the case of thin films with thicknesses the order of few hundreds of nanometers or less, most of the diffraction signal originates from the substrate and the intensity of the diffraction peaks coming from the overlayer is too low for getting reliable measurements.

In order to overcome these shortcomings, grazing incidence techniques
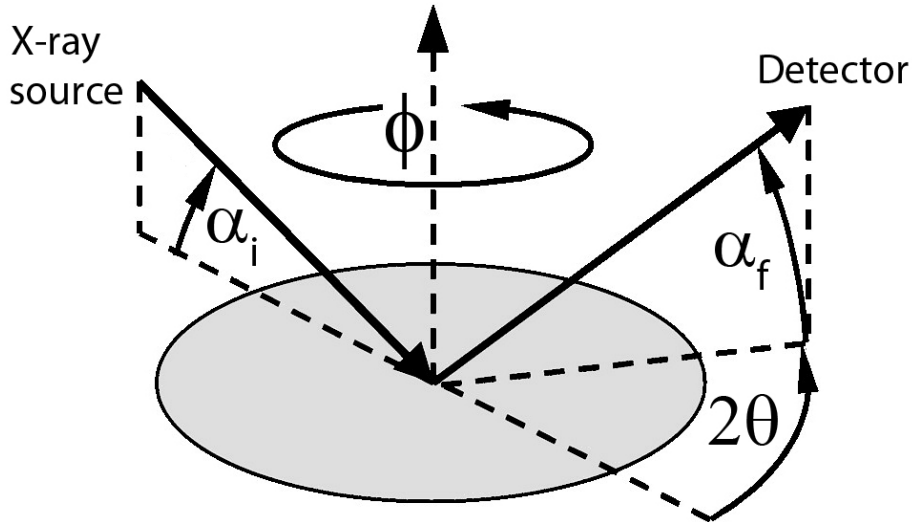
Figure 3.12: Experimental geometry for grazing incidence x-ray diffraction measurements. α_i is the angle formed by the incident beam with the sample surface, α_f is the out-of-plane angle between the diffracted beam and the sample surface and 2ϑ is the in-plane angle between the projections of the diffracted beam and of the incident beam in the plane containing the sample surface.

have been developed. In what is called Grazing Incidence X-ray Diffraction (GIXRD) the incident beam forms an extremely small angle with the surface of the sample, thus increasing the distance traveled by the X-ray beam within the thin film, while at the same time minimizing the penetration depth in the substrate. The experimental geometry for this kind of measurement is shown in figure 3.12, where all the relevant angles are indicated. During this kind of measurements the angle α_i formed between the incident beam and the sample surface is kept at a fixed value, in order to obtain the grazing incidence condition, while the detector can be moved both around the normal to the sample surface (forming the *in-plane* angle 2ϑ with the direction of the projection of the incident beam on the sample surface) and in the vertical direction (forming the *out-of-plane* angle α_f with the sample surface). If α_i is negligibly small (i.e. below 1°), as is often the case, and α_f is zero, then the detector measures only the diffraction peaks corresponding to lattice planes normal to the sample surface and fulfilling the Bragg equation, which are referred to as in-plane reflections.

It is also possible to replace the moving point detector with a fixed two-dimensional plane detector, like a CCD, normal to the projection of the incident beam on the sample surface. In this way it is possible to collect the

whole diffraction pattern at the same time, thus making the measuring procedure faster and reducing the exposition time of the sample to the possibly damaging X-ray beam.

Standard and synchrotron light sources

The most common X-ray sources used for XRD are sealed tubes in which the X-ray radiation is produced by hitting metal targets with electrons accelerated through an appropriate electric field. Usually such sources have a high enough intensity only at a specific wavelength, depending on the metal target material and indicated with K_α (since the radiation originates from transitions from the K shell). The most frequently used materials are copper, with $K_\alpha = 1.5418$Å, and molybdenum, with $K_\alpha = 0.7107$Å.

In order to get X-ray beams with much greater brightness over a wider range of wavelenghts it is possible to make use of synchrotron radiation, i.e. the radiation emitted by electrons or other charged particles when they are forced to move at relativistic speeds along curved trajectories. The desired wavelength for an X-ray diffraction measurement can then be selected using diffraction based monochromators, which are designed to exploit X-ray diffraction from known lattices as a mean to select specific wavelenghts from broader spectra.

Part of the measurements object of this thesis work have been carried out at the XRD-1 beamline of the ELETTRA Synchrotron Facility (Basovizza, Trieste, Italy), a third generation synchrotron light source.

Chapter 4

Rubrene thin films

In this chapter we will present the results of the morphological and structural characterization of rubrene epitaxial thin films grown following two different routes. Different techniques will be used, depending on the particular systems in consideration: rubrene thin films grown on tetracene single crystals and rubrene thin films grown on crystalline α-quaterthiophene (α-4T) films grown on potassium hydrogen phthalate (KAP) single crystals. The interest for the first heterostructure was motivated by the fact that tetracene single crystals are already known as one of the few substrates on which rubrene crystalline thin films can be grown, but a determination of the epitaxial and crystalline ordering of this system on a macroscopic scale was still missing[73, 74]. Regarding the second heterostructure, there have only been reports of the growth of α-4T films on rubrene single crystals, and not of the inverse process[83]. The possibility to grow multilayer heterostructures of different organic semiconductors is of particular interest for their possible use in the development of cascade organic solar cells, in which, by combining materials with complementary light absorption ranges, it is possible to get a significant increase of their photogeneration efficiency[104].

4.1 Organic epitaxy: an overview

With the term epitaxy one generally refers to a situation in which a crystalline overlayer grows on top of a crystalline substrate with a specific geometrical relationship being established between the crystalline lattices of the two layers.

Epitaxy between inorganic materials is a topic which has been studied

for a long time, and its fundamental mechanisms are now thoroughly understood[105]. More recently, the interest toward the development of electronic devices based on organic materials led to the study of epitaxy between organic and inorganic materials and also between both organic substrates and overlayers. Given the strength of the chemical bonds formed between the atoms in the substrate and overlayer in the case of inorganic materials, the key parameter controlling the epitaxy between these materials is the misfit between the substrate and overlayer lattices, given by:

$$f = \frac{|a_f - a_s|}{a_s} \tag{4.1}$$

where a_f and a_s are the bulk lattice constants along a particular direction of film and substrate, respectively. Inorganic thin films with a good crystalline quality can be obtained only with low misfit values.

In the case of organic materials, as already noted in chapter 1, the intermolecular interactions are weaker than in the case of inorganic materials, and this leads to less strict conditions over lattice misfit[77]. Moreover, organic molecules usually form crystalline lattices with large primitive cells, if compared to those of inorganic crystals, thus leading often to a complete incommensurism between substrate and overlayer crystalline lattices, but nonetheless epitaxial growth with precise epitaxial relationships is observed.

A simple way to classify epitaxial relationships between organic materials is that based over geometrical coincidence between lattice or reciprocal lattice points and directions of film and substrate[106, 107]. In particular, most small molecule organic semiconductors thin films often grow according to epitaxial relationships of the line-on-line (LOL) kind, i.e. with a coincidence only between non primitive reciprocal lattice points of the two layers[73, 83, 108, 109].

The actual driving force for epitaxy between these systems is usually found in the physical-chemical properties of the surfaces of the two layers at the interface and in the local surface structure. In particular periodical surface corrugations formed by hydrogen atoms protruding from the surface often play a critical role[40, 108, 110, 111].
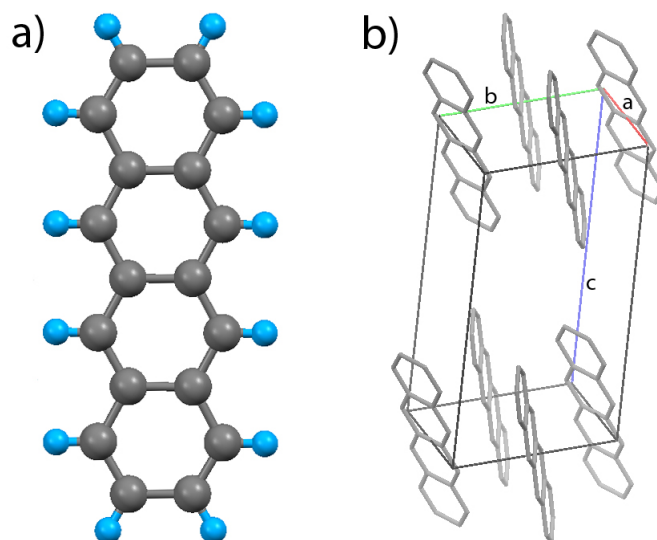
Figure 4.1: (*a*) Molecular structure of tetracene. The hydrogen atoms are reported in blue. (*b*) Unit cell and molecular arrangement in a tetracene triclinic crystal. The hydrogen atoms have been omitted for clarity.

4.2 Rubrene thin films on tetracene

This section is devoted to the description of the growth process of rubrene epitaxial thin films on tetracene single crystals and to the characterization of their structural properties. After a brief description of the material of choice for the substrate we will describe the results of the AFM and X-ray diffraction characterization of the thin films. In particular, from the analysis of the results of the diffraction measurements, the molecular packing in the thin film, along with its epitaxial relationship with the substrate will be determined.

4.2.1 The substrate

The substrates used for the epitaxial growth of rubrene thin films are tetracene (2,3-benzanthracene, $C_{18}H_{12}$) single crystals. Tetracene, whose molecular structure is shown in figure 4.1a, belong to the series of the polycyclic aromatic hydrocarbons, along with naphtacene, antracene and pentacene, and consists of four linearly fused benzene rings. It also resembles the core of the rubrene molecule (see also figure 2.1).

Tetracene single crystals with good crystalline quality can be obtained by the physical vapor transport method. Such crystals belong to the triclinic

Parameter	Value
Space group	$P\bar{1}$
a [Å]	6.0565(9)
b [Å]	7.8376(11)
c [Å]	13.0104(18)
$\alpha[°]$	77.127(2)
$\beta[°]$	72.118(2)
$\gamma[°]$	85.792(2)
Volume [Å^3]	572.97(24)
Z	2

Table 4.1: Unit cell parameters of triclinic tetracene collected at 175 °K, as reported in [112].

system, with the structural parameters (measured at 175 K) reported in table 4.1[112].

Our substrates have been grown from commercial powder (Sigma-Aldrich, 99.9%), with a source temperature of 185 °C and with a constant nitrogen flux of 20 ml min^{-1}. This way, during a single growth cycle, many tetracene crystals with lateral dimensions up to few centimeters and with a thickness of a few hundreds of nanometers can be obtained, as exemplified by the crystal reported in figure 4.2. All the crystals large enough to be used as a substrate have firstly been inspected with an optical microscope, in order to check the quality of their surface. The selected crystals have then been picked up with a needle and placed on the surface of silicon (1 0 0) wafers, where they spontaneously adhere due to electrostatic forces. Silicon wafers have been chosen instead of quartz plates because of their sharp X-ray diffraction spots, in contrast with the broad diffraction peak from amorphous SiO_2, in order to make the interpretation of the diffraction data collected from our samples easier.

4.2.2 Growth of rubrene thin films

Rubrene thin films have been grown by OMBE on top of the tetracene single crystals prepared as described in the previous section. The deposition process has been carried out at about 10^{-7} mbar and at a source temperature of 180 °C, leading to a deposition rate of 2 Å min^{-1}. All the films have been grown with a nominal thickness of 20 nm, as measured by the quartz microbalance, and during the growth the substrate has been kept at room
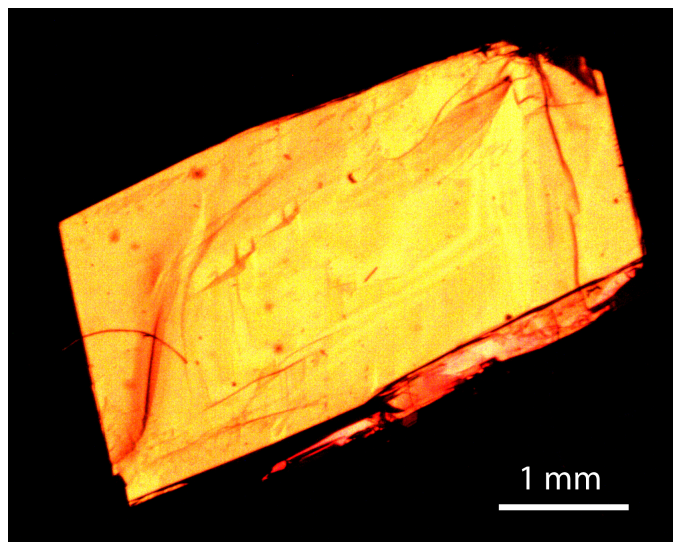
Figure 4.2: A millimeter-sized tetracene single crystal grown by physical vapor transport. The photo was taken with an optical microscope under polarized light.

temperature. The commercially available rubrene powder (Acros Organics, 99%) used as the source material for deposition was first subjected to several sublimation cycles in order to purify it[67].

The deposition rate was chosen in order to minimize the presence of amorphous rubrene along with the crystalline phase, as described in ref. [74].

4.2.3   AFM characterization

A first check of the thin films aimed at verifying that the films were actually crystalline and that the substrate was homogeneously covered has been carried out by tapping mode AFM imaging.

In figure 4.3 the morphological AFM image of one of the samples, showing the typical appearance of the as-grown films, is reported. The film seems to completely cover the substrate surface, except for some holes with a depth of the order of the film thickness and spread all over the surface. These holes are characteristic of rubrene thin films grown on tetracene and originate from the amorphous rubrene nano dots formed during the first stages of the film growth and that afterward evolve into crystalline rubrene[74]. Apart from these holes, the surface is crossed by flat terraces with a thickness, equal to (1.4 ± 0.1) nm or to integer multiples of this quantity, as extracted from
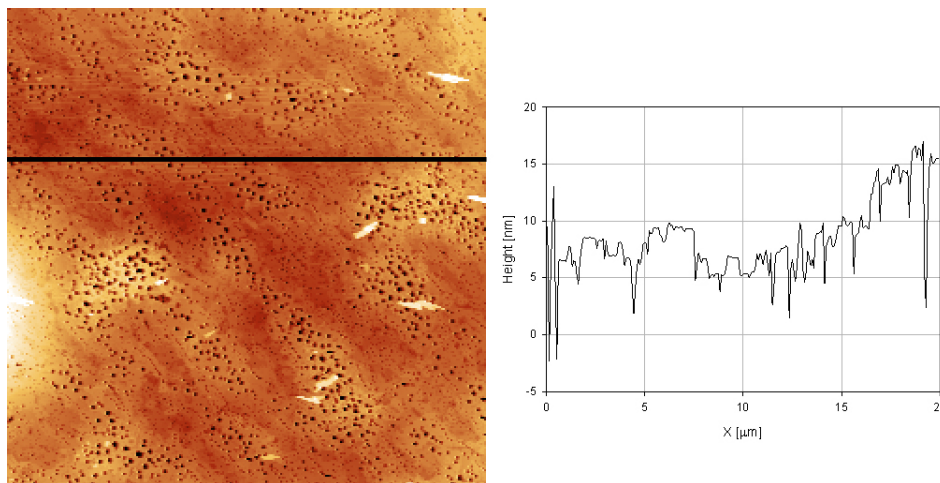
Figure 4.3: Morphological AFM image of a 20×20 µm^2 region of a rubrene thin film with a nominal thickness of 20 nm grown on top of a tetracene single crystal. On the right side is reported the cross-sectional height profile extracted along the scan line highlighted on the AFM image.

cross sectional profiles such as that reported in figure 4.3. Since the height of a single rubrene molecular layer in the **a** direction of the orthorhombic phase is ∼1.34 nm, this seems to suggest that the film consists of successive layers of rubrene molecules packed according to the rubrene orthorhombic structure (see figure 2.4b) and with the (b,c) plane parallel to the substrate surface.

In order to confirm this assumption and to carry on a full structural characterization of this system we then recurred to Grazing Incidence X-ray Diffraction (GIXD) measurements.

4.2.4   Grazing incidence X-ray diffraction measurements

In a GIXD experiment (see also chapter 3) a monochromatic X-ray beam is directed toward the sample surface with a very low (grazing) angle of incidence, in order to maximize the diffraction from the overlayer, at the same time minimizing the diffraction from the substrate. By this technique it is then possible to get structural information from extremely thin films. Moreover, it is possible to gain information about the macroscopic in-plane orientation of the crystalline film, being able to determine the epitaxial relationship between the substrate and the overlayer.

The GIXD measurements described in this work have been carried out at
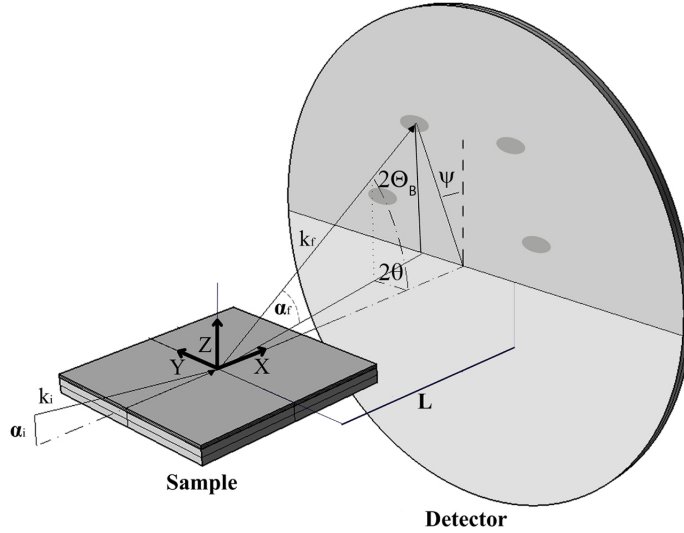
Figure 4.4: Geometry of the GIXD set-up. The incident beam forms an angle α_i with the sample surface and the diffracted beam is recorded by a planar CCD detector at a distance L from the beam incidence point. α_f and 2ϑ indicate the out-of-plane and in-plane diffraction angles, respectively, $2\Theta_B$ is the Bragg angle, ψ is the polar angle and **X**, **Y** and **Z** are the coordinates of the laboratory reference frame.

the XRD1 beamline of the ELETTRA Synchrotron Facility (Trieste, Italy).

The experimental geometry (see figure 4.4) is such that the X-ray beam direction is fixed, while the sample holder can be rotated about the different diffractometer axes, in order to reach the sample surface alignment in the horizontal plane containing the X-ray beam, and subsequently rotate it around an axis (**Z**) perpendicular to this plane or, in alternative, vary the angle between beam and surface (angle of incidence α_i). The diffracted pattern is then collected by a 2D CCD detector (165 mm, MarResearch) perpendicular to the incident beam, which allows the simultaneous collection of the whole diffraction pattern, leading to a faster data collection procedure.

The X-ray beam wavelength used for our measurements is 0.99987 Å. It can be selected continuously from the white emission spectrum of the wiggler source by a double crystal Si(111) monochromator. The number of photons per second in the incident beam is 2.8×10^{10}. The beam cross-section at the sample is limited by double slits to 0.2 mm both in the horizontal and vertical directions. The desired angle of incidence has been selected by collecting a

series of diffractograms at different α_i values and then choosing the angle for which diffraction from the substrate was still clearly visible but did not interfere too much with the diffraction pattern coming from the overlayer. For our experiments an angle $\alpha_i = 0.2°$ was chosen.

Analysis of the diffraction patterns

At first, before any analysis can be carried out, the collected diffraction images need to be corrected for various factors depending on the experimental geometry: Lorentz-polarization factor[113], detector tilt, detector misalignment and distortions. Using the software Fit2D along with diffraction patterns collected from standard samples, it is possible to extract all the correction parameters by means of a calibration procedure and afterward to apply them to all the analyzed diffraction images[114]. By calibration it is also possible to get refined values for the radiation wavelength and the sample-detector distance. In order to carry on the calibration procedure we collected powder diffraction spectra from a LaB_6 NIST standard sample[115].

In general, a GIXD two-dimensional pattern looks like a semicircle with a homogeneous background over which various bright spots, corresponding to the various diffraction peaks, are superimposed (see for example figure 4.5). The first step for the analysis of the diffraction images is to index the observed reflections with the corresponding ($h\ k\ l$) indexes. This can be done by comparison with simulated diffraction patterns of a system with the same geometry. For the simulation of the two-dimensional diffraction patterns the *Mathematica* package *NANOCELL*, developed for the simulation of Grazing Incidence Small-Angle X-ray Scattering images[116], has been used. This software, which have been modified by us in order to account for our experimental geometry, is able to simulate two-dimensional diffraction patterns originating from an arbitrary crystalline structure and to superimpose it to the collected image, for easier peak identification.

The exact position of the measured diffraction peaks, corrected according to the calibration factors, can be determined by radial integration of the two-dimensional diffraction pattern. This procedure, which has also been carried out by using the Fit2D software, gives as a result a one-dimensional diffractogram, which can be analyzed with standard analysis techniques.
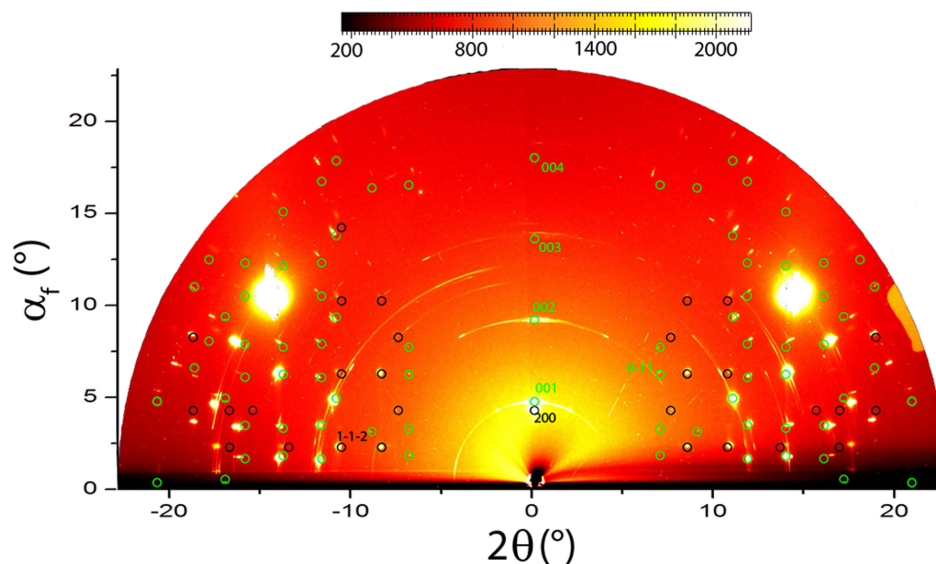
Figure 4.5: Two-dimensional GIXD pattern collected while rotating the sample by a full turn about the normal to the sample surface. The circles superimposed on the CCD image represent the position of the simulated diffraction spots from polycrystalline tetracene with the (0 0 1) planes parallel to the sample surface (green circles), and from polycrystalline rubrene with the (2 0 0) planes parallel to the sample surface (black circles). Also, the Miller indexes of the reflections cited in the text are reported. The positions of the peaks in the experimental image are not corrected for detector misalignment.

Determining the out-of-plane film orientation

In order to identify the different crystalline phases present in a molecular thin film, the first step is to carry out 'survey scans', in which the sample is rotated around the surface normal ($\mathbf{Z}$) while the pattern is being collected [117]. This way all the reflections coming from the sample are collected and can be used as fingerprints for the identifications of the different crystalline phases present in the sample.

In figure 4.5, a GIXD pattern collected while rotating the sample by a full turn about the normal to the sample surface, for a total exposure time of 1400 s, is shown. In general, such patterns are a superposition of the diffraction patterns originated from the different families of lattice planes of the overlayer and substrate structures. If either the overlayer or the substrate are a mixture of different crystalline phases, then in the measured pattern there will be diffraction spots coming from all the different crystalline phases

present in the sample. Moreover, if the film is constituted by different grains with a completely random orientation then the diffraction pattern will consist of several concentric circles, resembling that of a powder sample.

Tetracene single crystals grown by physical vapor transport usually expose the (0 0 1) surface[118]; in addition, the results of the preliminary AFM characterization suggested that the molecules in the rubrene thin film are packed in the orthorhombic phase, with the (1 0 0) plane parallel to the substrate surface. Thus, in order to identify the origin of the various spots constituting the observed pattern, we first compared it with the simulated GIXD patterns of orthorhombic rubrene and tetracene crystals with the same relative orientations.

In figure 4.5, the simulated diffraction pattern of polycrystalline orthorhombic rubrene with the (2 0 0) plane parallel to the substrate surface and with random azimuthal orientation of the grains, chosen in order to account for the rotation of the sample around the vertical axis during the collection of the diffraction pattern, is superimposed in black to the experimental pattern, while the simulated pattern of polycrystalline tetracene with the same out-of-plane orientation as our substrate is shown in green. For both patterns, some of the pertinent crystallographic indexes are also reported (in accordance to the structures reported in [46] and [112]).

The presence of many spots originating from the tetracene substrate is due to the extremely low thickness of the rubrene film, while the two bigger spots are originated from the silicon crystal used as a sample holder. The presence of the diffraction spots of the substrate is also necessary in order to determine the epitaxial relationship between the substrate and the overlayer, as will be shown in the next section.

It can be noticed that the whole measured diffraction pattern can be obtained by the superposition of the two simulated diffraction patterns, with no spots being left out. This means that the substrate is indeed crystalline tetracene exposing the (0 0 1) surface and, moreover, that the rubrene thin film is entirely formed by molecules packed in the rubrene orthorhombic crystalline phase, all with the same out-of-plane orientation, i.e. with the rubrene (2 0 0) lattice plane parallel to the surface of the substrate. Hence, we can rule out the presence of other rubrene polymorphs in the film.

The progressive deviation of the positions of the observed spots with respect to the simulated ones with the increase of the distance from the

Peak number	Measured position (Å)	Corresponding reflection	Calculated position (Å)	$\Delta(\%)$
1	13.47112	RUB (200)	13.43000	0.3
2	12.25517	TEN (001)	12.10344	1.3
3	6.13478	TEN (002)	6.05172	1.4
4	4.08760	TEN (003)	4.03448	1.3

Table 4.2: Experimental positions of the peaks (converted to the corresponding lattice spacing d and corrected according to the calibration parameters) observed in the diffractogram reported in figure 4.6. In the third column the Miller indexes corresponding to each peak are reported, and in the fourth column the expected position of each reflection, as calculated from the known structural parameters, is reported. In the fifth column the relative difference between calculated and measured peak positions is reported.

center is due to the non perfect orthogonality of the detector with respect to the incident beam and is one of the effects that can be corrected thanks to the calibration procedure. Once the calibration parameters have been applied to the measured data, performing a radial integration of the image, we found a good correspondence also for the higher order reflections (see table 4.2, where the corrected positions of the out-of-plane peaks are reported).

In figure 4.6 the central vertical region of a GIXD pattern is reported. In general the spots appearing along the vertical axis of the diffraction pattern are due to reflections from lattice planes parallel to the substrate surface and are therefore labeled as out-of-plane reflections. Below the 2D CCD image, the 1D diffraction spectrum obtained by radial integration and calibration of the 2D pattern is shown. The positions of the four peaks visible in the pattern are reported in table 4.2, along with the calculated positions of the corresponding rubrene $(h\,0\,0)$ and tetracene $(0\,0\,l)$ reflections. The first peak corresponds to the $(2\,0\,0)$ reflection of the orthorhombic phase of rubrene, which is the only reflection originating from the $(h\,0\,0)$ family of planes of the orthorhombic rubrene crystal with a non-negligible intensity. The three other peaks correspond to the reflections originating from the $(0\,0\,1)$, $(0\,0\,2)$ and $(0\,0\,3)$ planes of a triclinic tetracene crystal.

The measured peak positions are in good agreement with the calculated ones and the larger shift between measured and calculated positions of the tetracene diffraction peaks, with respect to the rubrene peak, can be accounted for by noticing that the calculated peak positions for tetracene are derived from the data reported in ref. [112], which refer to measurements
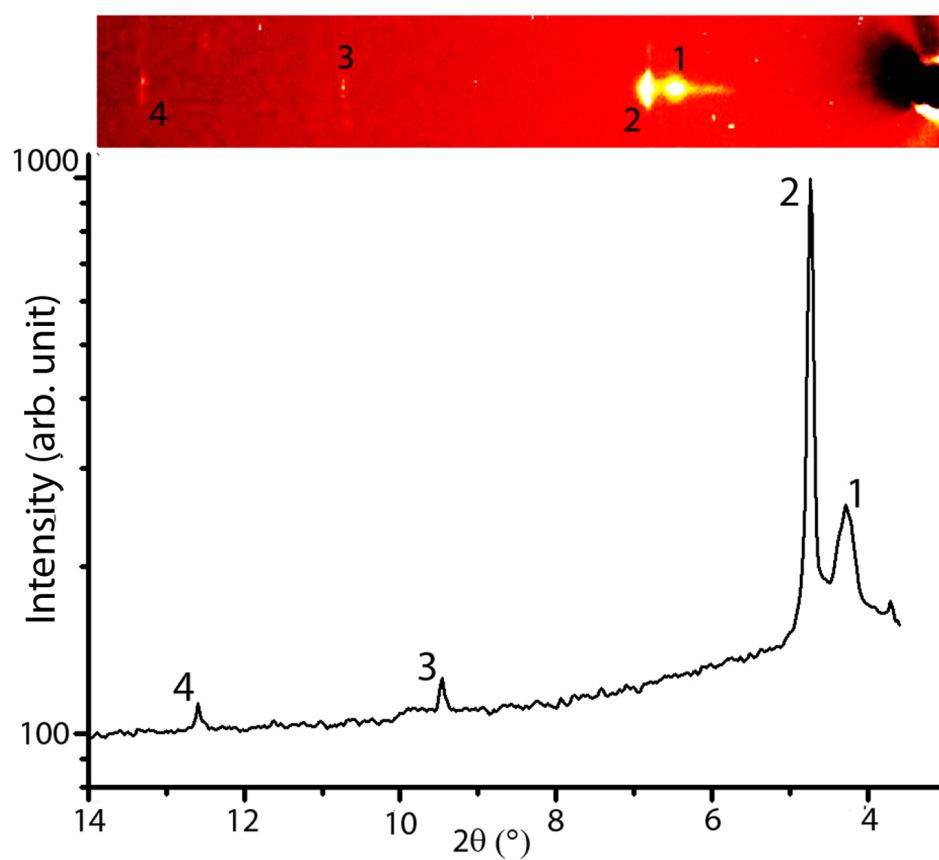
Figure 4.6: *Top*: magnification of the out-of-plane region of the GIXD diffraction pattern of a rubrene thin film grown on a tetracene substrate. *Bottom*: one-dimensional diffractogram obtained by radial integration of the two-dimensional pattern reported at the top. The numbers indicating the peaks refer to table 4.2. Peak 1 originates from rubrene, while the other three peaks originate from the tetracene substrate.

carried out at 175 °K, while our measurements have been carried out at room temperature. These data thus confirm that the tetracene crystals used as substrate expose the (0 0 1) surface, and that rubrene thin films are grown with the (2 0 0) crystallographic plane parallel to the substrate surface.

Finally, in the GIXD pattern in figure 4.5 one can also observe the presence of some ring-like features, mainly originating from the out-of-plane tetracene diffraction spots and from some other bright spots. On the other hand, there is no ring associated to the rubrene diffraction spots. Such ring-like features indicate the presence of a high degree of texture of some parts of the sample and are probably due to disordered fragments of crystalline tetracene disposed around the main one and probed by the beam during sample rotation. This explanation is confirmed by the fact that, collecting a series of images at different azimuthal orientations of the sample, the rings are present only in some of the images, i.e. when the sample is rotated such that the disordered tetracene crystals enter the X-ray beam.

In-plane film orientation and epitaxial relationship with the substrate

In order to verify the existence of an in-plane order of the crystalline structure of the film, i.e. that the film is not constituted by different grains with random azimuthal orientations, we collected a series of GIXD patterns rotating the sample by a total rotation angle of 180° in 2° steps around the vertical axis, with a total scan time of about 8 h. If the grains constituting the film are not distributed with a random azimuthal orientation, then for each sample orientation only some of the diffraction spots should appear in the collected pattern. Plotting the intensity of a given reflection as a function of the azimuthal orientation of the sample, one can obtain a plot with one or more peaks, corresponding to the azimuthal orientations at which the reflection appears. This procedure is equivalent to collecting a pole figure for the given reflection, making it possible to get some insights on the in-plane order of the overlayer by comparison with the simulated pole figures of the reflections under exam [108, 119, 120].

In crystallography a pole figure is a polar plot over which the intensities of specific reflections are plotted as a function of the azimuthal angle φ of the sample at which they appear and of the polar angle ψ (defined in figure 4.4) at which they appear in the collected diffraction pattern. The simulation of
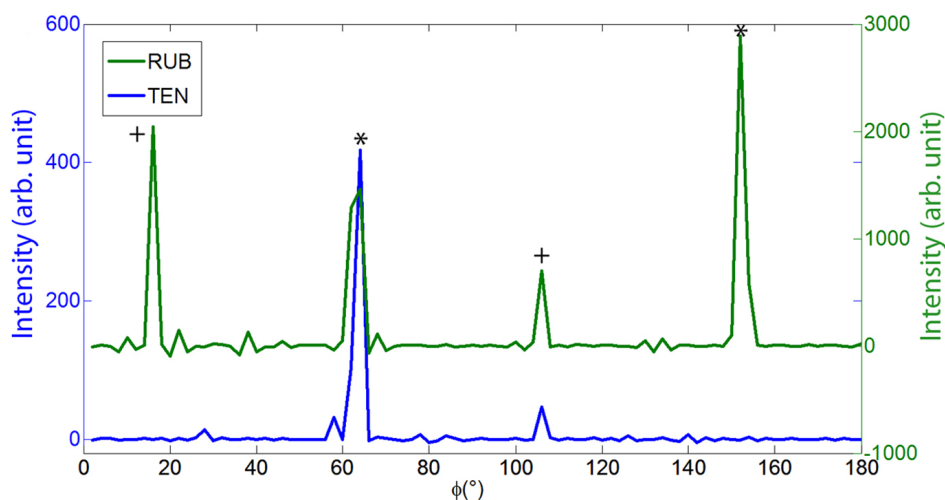
Figure 4.7: Measured intensity of the $(1\ \bar{1}\ \bar{2})$ reflection of the rubrene thin film (upper curve) and of the $(0\ \bar{1}\ 1)$ reflection of the tetracene substrate (lower curve) as a function of the azimuthal orientation of the sample (φ). The rubrene plot has been shifted to the left by $36°$ in order to show the correspondence between rubrene and tetracene reflections. The two (*) and (+) symbols indicate reflections from differently oriented crystals.

the pole figures of the crystalline structures of our interest have been carried out with the STEREOPOLE software[121].

In figure 4.7 we report the measured intensity *versus* azimuth plots for the $(0\ \bar{1}\ 1)$ reflection of tetracene and the $(1\ \bar{1}\ \bar{2})$ reflection of rubrene, respectively, while in figure 4.8 we report the superposition of the simulated pole figures of those two reflections, calculated for a tetracene and a rubrene single crystals with the $(0\ 0\ 1)$ and the $(2\ 0\ 0)$ planes, respectively, normal to the azimuthal rotation axis.

In the lower curve of figure 4.7, due to the triclinic symmetry of the tetracene unit cell, the $(0\ \bar{1}\ 1)$ diffraction spot should appear only once for each complete revolution of the crystal around its vertical axis, as can be observed in the simulated pole figure reported in figure 4.8, where no reflection equivalent by symmetry to the $(0\ \bar{1}\ 1)$ one is present. The presence of two clearly distinct peaks in the lower plot of figure 4.7, thus, indicating the appearance of the $(0\ \bar{1}\ 1)$ reflection for two different azimuthal orientations of the sample, means that the substrate is constituted by two differently oriented crystals. The angular separation between the two peaks in the plot relative to the tetracene $(0\ \bar{1}\ 1)$ reflection, as determined by the
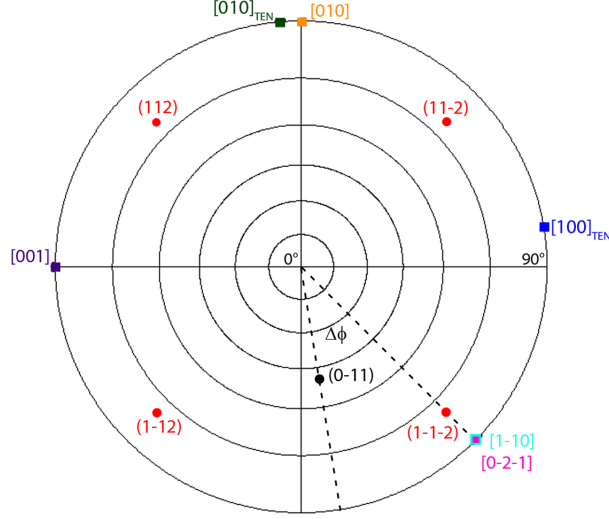
Figure 4.8: Superposition of the simulated pole figures of a rubrene crystal with the (1 0 0) plane parallel to the image plane and of a tetracene crystal with the (0 0 1) plane parallel to the image plane. The {1 1 2} and the (0 $\bar{1}$ 1) reflections are reported for rubrene and tetracene, respectively. The concentric circles are separated by $\Delta\psi = 15°$. The two pole figures are superimposed with an azimuth such that the azimuthal angle between the (1 $\bar{1}$ $\bar{2}$) reflection of rubrene and the (0 $\bar{1}$ 1) reflection of tetracene, labelled as $\Delta\varphi$, is consistent with the experimentally determined one (36°). On the outer circle (corresponding to $\psi = 90°$) the [0 1 0], [0 0 1] and [0 $\bar{2}$ $\bar{1}$] rubrene direct lattice directions and the [1 0 0], [0 1 0] and [1 $\bar{1}$ 0] tetracene direct lattice directions are also reported, as used in the text to determine the epitaxial relationship between the overlayer and the substrate.

plot reported in figure 4.7, is 42°. This must correspond to the in-plane angle between the lattice orientations of the two crystals constituting the substrate. Indeed, careful observation of the sample with a light-polarized optical microscope shows that the substrate actually consists of two differently oriented tetracene single crystals that coalesced together during their growth, and that the angular difference in their orientation is equal to $\sim 42°$.

In the upper curve in figure 4.7, the intensity of the (1 $\bar{1}$ $\bar{2}$) reflection of the overlayer as a function of the azimuthal orientation of the sample is plotted. In this case one can notice the presence of few clearly defined peaks over a uniform background. This means that the rubrene (1 $\bar{1}$ $\bar{2}$) reflection is present only at some specific azimuthal orientations of the sample and, thus, that the film crystalline domains are oriented along few definite directions. The angular separation between two successive appearances of the (1 $\bar{1}$ $\bar{2}$) diffraction spot, or one of its symmetrically equivalent reflections,

for a rubrene orthorhombic crystal is 90°, as can be observed in the simulated
pole figure reported in figure 4.8. This means that in the intensity plot
reported in figure 4.7, which refers to a 180° range, the intensity of the
$(1\,\overline{1}\,\overline{2})$ reflection of rubrene should show only two peaks for each in-plane
orientation of the overlayer lattice. The plot reported in figure 4.7 shows four
different peaks; the separation between the first and the third peak is 90°
and is equal to that between the second and the fourth peak. This means
that the overlayer has two different in-plane orientations, with an angular
separation between each other corresponding to that between the first and
the second peak in the plot, namely 42°.

The angular separation between the two different in-plane orientations
of the rubrene thin film thus corresponds to the angular separation between
the two different orientations of the substrate. This, along with the fact
that the overlayer lattice have a unique out-of-plane orientation, means that
for each orientation of the substrate there is only one possible orientation of
the thin film crystalline lattice, i.e. there is a unique epitaxial relationship
between the film and the substrate. The two plots reported in figure 4.7
were shifted in order to show more clearly the correspondence between the
azimuthal positions of the rubrene and tetracene reflections. The actual
angular separation between the appearance of the tetracene $(0\,\overline{1}\,1)$ reflection
and that of the successive rubrene $(1\,\overline{1}\,\overline{2})$ reflection is $(36 \pm 2)°$. Starting
from such an angular separation, and referring to the two simulated pole
figures reported in figure 4.8, on which we also plotted some relevant direct
lattice directions of rubrene and tetracene, the exact epitaxial relationship
between the two layers can now be determined. In order to do so, the two
pole figures reported in figure 4.8 have been reciprocally oriented such that
the angle $\Delta\varphi$ between the tetracene $(0\,\overline{1}\,1)$ reflection and the rubrene $(1\,\overline{1}$
$\overline{2})$ reflection is equal to the experimentally determined one $(36 \pm 2)°$. This
way, it can be clearly concluded that the experimental data are compatible
with an orientation of the overlayer crystalline lattice with respect to the
substrate such that the $[1\,0\,0]$ direction of the tetracene lattice forms an
angle of ̃80° with the $[0\,1\,0]$ lattice direction of the rubrene film, and the b
axis of rubrene forms an angle of ̃5° with the b axis of tetracene. Moreover,
there is a coincidence between the $[0\,\overline{2}\,\overline{1}]$ and $[1\,\overline{1}\,0]$ lattice directions of
rubrene and tetracene, respectively . This situation is equivalent to the
epitaxial relationship rubrene$[0\,2\,1]$‖tetracene$[1\,\overline{1}\,0]$, previously suggested

by molecular resolution atomic force microscopy results[73], therefore related to a local scale. This epitaxial relationship, corresponding to an alignment between non primitive reciprocal lattice vectors of the substrate and the overlayer, can be classified as an example of *line-on-line* epitaxy, which is the most common kind of epitaxy between small molecule organic materials[106].

In figure 4.9a the structural model of the interface between a rubrene molecular layer and a tetracene molecular layer, reciprocally oriented according to our experimental results and observed along the [0 2 1] lattice direction of rubrene, is reported. Careful observation of the (1 0 0) surface of rubrene and the (0 0 1) surface of tetracene shows the presence on both surfaces of pronounced corrugations formed by hydrogen atoms protruding from them. The periodicity of the corrugation of the rubrene surface, corresponding to the spacing between the (0 1 2) lattice planes, is $d_{(012)} = 5.08$ Å, while the periodicity of the corrugation on the tetracene (0 0 1) surface, corresponding to the spacing between the (1 1 0) lattice planes, is $d_{(110)} = 4.96$ Å. Despite the absolute lack of commensurism between the lattices of the two materials, thus, the misfit between the periodicity of the most prominent corrugations at the interface between the substrate and the overlayer is of only 2.4%. This suggests that the driving force for the epitaxial growth of this heterostructure with a unique epitaxial relationship is indeed the alignment between pronounced surface corrugations at the interface, as is clearly visible in figure 4.9. These conclusions about the origin of the observed epitaxial relationship are reinforced by the fact that the role of surface corrugations in determining the epitaxial ordering of molecular thin films has already been assessed for several all-organic epitaxial heterostructures, for which often no commensurism between the respective crystalline lattices can be found[40, 83, 108, 110, 111].

The most important finding extracted from the GIXD experiment is that the rubrene overlayer possesses a unique orientation on a macroscopic scale, i.e. that rubrene crystalline thin films can be grown on tetracene single crystals with a single lattice orientation. As already noted in the introduction to this chapter, this is a result of particular importance for the development of efficient rubrene based devices, since it permits to fully exploit the highly anisotropic charge transport and optical properties of this material. Moreover the **b** lattice direction of the rubrene overlayer lays parallel to the substrate surface, permitting to easily build devices exploiting conduc-
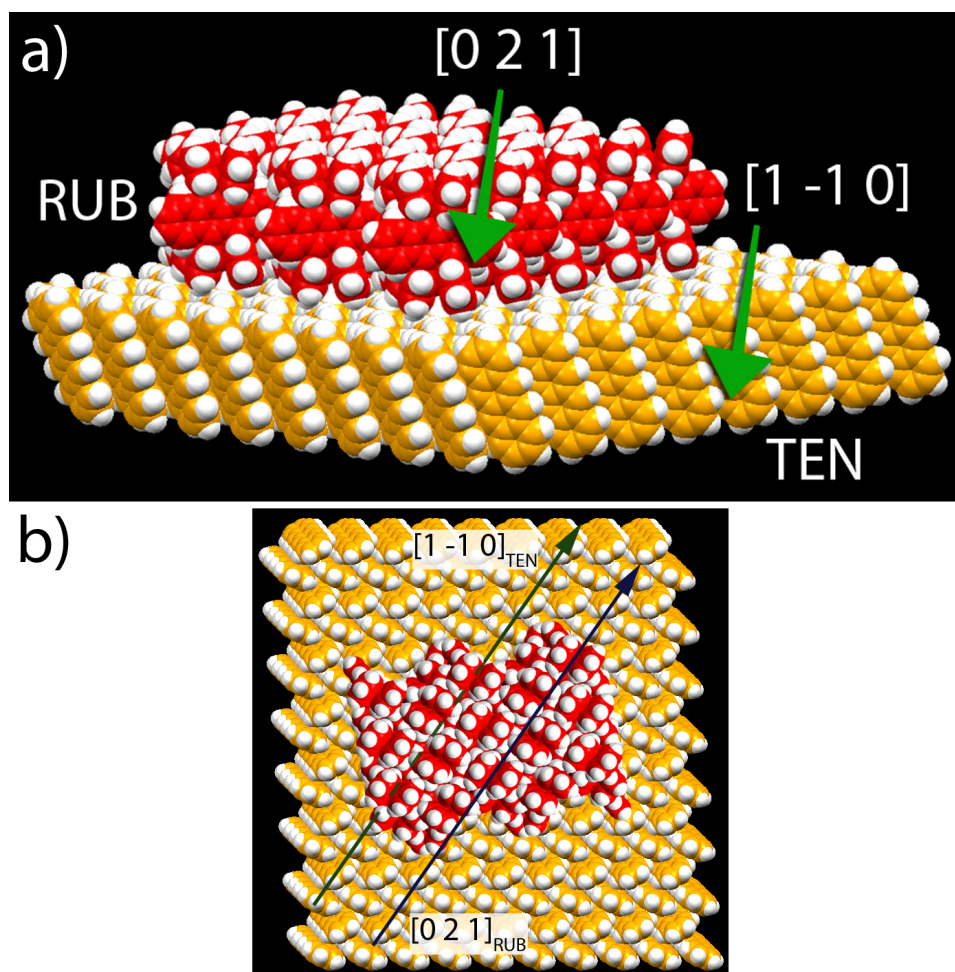
Figure 4.9: (*a*) Structural model of the arrangement of rubrene and tetracene molecules in the heterostructure, as deduced by the measurements described in the text. The pronounced surface molecular corrugations aligned along the [0 2 1] and [1 $\bar{1}$ 0] directions of rubrene and tetracene, respectively, are indicated by arrows. (*b*) Top view of the structural model reported in (*a*). The relevant directions of rubrene and tetracene crystals are indicated by the arrows.
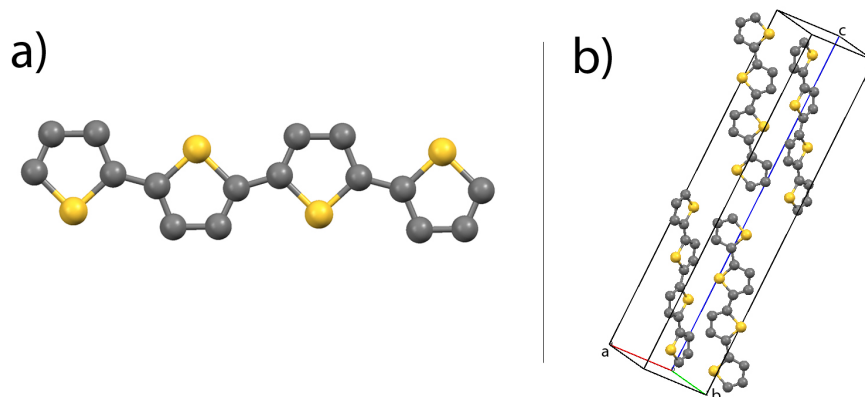
Figure 4.10: (*a*) Molecular structure of α-4T. (*b*) Unit cell and molecular packing of the monoclinic low-temperature polymorph of α-4T. The hydrogen atoms have been omitted for clarity.

tion along this direction, which is the most favorable with respect to charge carrier transport[49].

4.3 Rubrene thin films on α-4T films

This section is devoted to the description of the growth dynamics of rubrene epitaxial thin films deposited on top of an heterostructure constituted by an α-4T film grown on a KAP single crystal and to the characterization of their structural properties. In order to do so, we deposited by OMBE rubrene thin films of different thicknesses and studied the evolution of their morphology with increasing thickness by means of AFM and optical measurements. The combination of these two techniques, along with the comparison to the complementary system already reported in literature, will give us a deeper understanding of the structural properties of this heterostructure.

4.3.1 Growth of α-4T on KAP

α-4T (2,2':5',2":5",2"'-Quaterthiophene, $C_{16}H_{10}S_4$), whose molecular structure is reported in figure 4.10a, has been synthesized following the procedure reported in ref. [122]. It is a member of the oligothiophenes family, which comprises several already well-known semiconducting materials, comprising α-4T itself.

Commercially available KAP (potassium hydrogen phtalate, $C_8H_5KO_4$) single crystals (Eksma Optics, Vilnius, Lithuania) exposing the (0 1 0) sur-
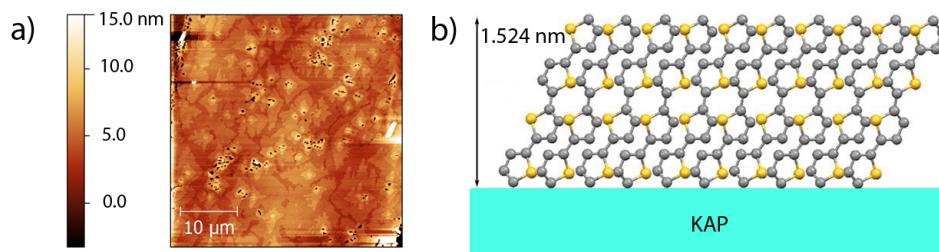
Figure 4.11: (*a*) Morphological AFM image of a 40×40 µm^2 region of an α-4T film with a nominal thickness of 8 nm epitaxially grown on the surface of a KAP single crystal. (*b*) Schematic representation of the molecular packing in the α-4T film shown in (*a*), according to ref. [108].

face are used as a substrate for OMBE deposition of the α-4T films. The α-4T powder is sublimated at 170 °C at a pressure lower then 2×10^{-9} mbar and with the substrate at room temperature. The nominal thickness of the α-4T films, as measured by the quartz microbalance, is of 8 nm, assuring a full coverage of the substrate.

In figure 4.11a is shown the AFM morphology image of a 40×40 µm^2 region of an as-grown α-4T film. The KAP substrate is completely covered by the α-4T film, which is formed by wide and flat crystalline islands that coalesced together during the film growth. It has already been demonstrated that α-4T grows on KAP with the molecular packing of its low temperature monoclinic polymorph[37] (as shown in figure 4.11b) and with an in-plane orientation of its crystalline domains described by the α-4T[1 0 0]//KAP[0 0 1] epitaxial relationship[108].

4.3.2   Rubrene thin films growth

Crystalline α-4T films grown as described in the previous section are used as a substrate for the subsequent deposition of rubrene thin films, in turn grown by OMBE, at a pressure lower then 2×10^{-9} mbar, with rubrene deposition temperature of 200 °C. By the same experimental conditions we grew several rubrene films with different thicknesses, in order to gain knowledge about their morphological evolution with increasing thickness.

AFM characterization

In figure 4.12a, 4.12b, 4.12c, 4.12d the morphologic AFM images of a 5×5 µm^2 region of samples with a nominal thickness of the rubrene overlayer of

0.1 nm, 0.5 nm, 1 nm and 5 nm, respectively, are reported. In figure 4.12a large and molecularly flat islands grown on top of each other are visible. All these structures have a thickness of (1.5 ± 0.1) nm, as shown in the height profile reported below the AFM image. This value corresponds to the interplanar spacing $d_{(002)}$ between the (0 0 2) lattice planes of the low-temperature monoclinic polymorph of α-4T, that is, to the height of a single layer of 'standing' α-4T molecules, as sketched in figure 4.11b[37]. These larger islands thus belong to the previously grown α-4T film. Similarly shaped structures, with the same height, are also visible in the background in figure 4.12b and c, even if they are covered by thicker rubrene layers. In figure 4.12d instead, the underlying α-4T film is completely hidden by the rubrene overlayer.

The AFM images reported in figure 4.12a and b show the surface morphology of samples covered respectively by a 0.1 nm and a 0.5 nm thick rubrene film. In both images the film consists of separated rubrene islands: in the 0.1 nm sample the islands are highly sparse, while in the thicker film they are larger and mainly concentrated in correspondence of the edges of the α-4T islands. The thickness of all the rubrene islands in both samples is (1.3 ± 0.1) nm. This value closely resembles the interplanar spacing $d_{(200)} = 1.343$ nm between the (2 0 0) planes of the rubrene orthorhombic crystalline phase, corresponding to the height of a single layer of rubrene molecules packed in the orthorhombic phase with the (1 0 0) plane parallel to the substrate surface. It can be observed that this film structure is the same found for rubrene thin films grown on tetracene (see section 4.2) and resembles also the molecular packing of rubrene thin films grown on other substrates[25].

In figure 4.12c we report the AFM morphological image of the sample covered by a rubrene overlayer with a nominal thickness of 1 nm. The shape of the underlying α-4T islands is still visible, but they are almost completely covered by a single layer of rubrene molecules (with the usual thickness of (1.3 ± 0.1) nm) on top of which a second layer with the same morphology of the previous one began growing.

Finally, in figure 4.12d we report the morphological AFM image of the surface of a sample covered by a 5 nm thick rubrene overlayer. In this case the morphology of the underlying α-4T film can not be distinguished anymore, being completely hidden by the multiple molecular layers constituting
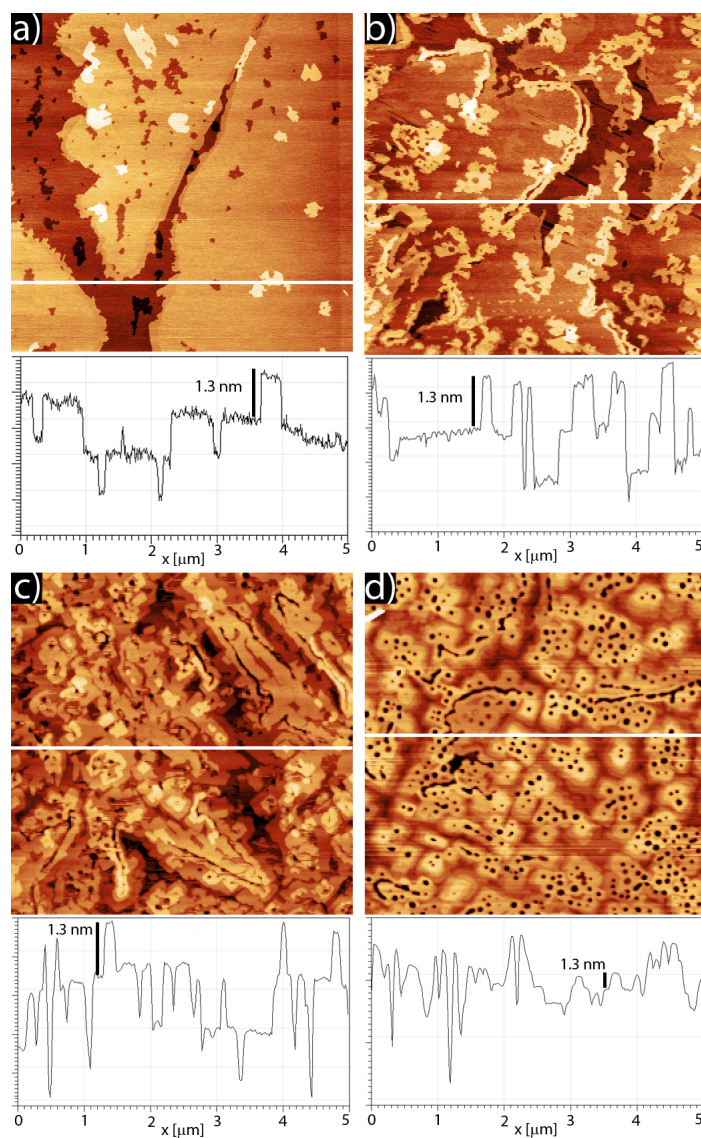
Figure 4.12: AFM morphological images of a 5×5 µm^2 area of the surface of four different rubrene/α-4T/KAP heterostructures. All the samples consist in an α-4T thin film with a nominal thickness of 8 nm deposited on the (0 1 0) surface of a KAP single crystal. On top of that heterostructure rubrene thin films with different nominal thicknesses has been grown. In (a), (b), (c) and (d) are reported the images referring to samples covered by a rubrene thin film with a nominal thickness of 0.1 nm, 0.5 nm, 1 nm, 5 nm, respectively. Below each image is reported the cross-sectional profile extracted along the scan line indicated on the respective AFM image.

the rubrene film. Consistently with the thinner films previously described, the rubrene film consists of successive layers all with the same thickness, corresponding to the height of single layers of rubrene molecules packed according to the rubrene orthorhombic crystalline phase with the (2 0 0) lattice plane parallel to the substrate surface. However, a distinctive feature of this film can be easily noticed, namely the presence of a number of holes spread on the whole surface. This kind of 'hole pattern' has been already observed for rubrene thin films films grown on tetracene single crystals (see also figure 4.3), and their origin has been explained as the result of a kinetic driven transformation of amorphous rubrene nano-dots, initially present on the surface of the film, into a crystalline molecular layer after the full deposition process[74].

X-ray diffraction measurements

In order to confirm the out-of-plane molecular packing inferred from the analysis of the surface morphology, X-ray diffraction measurements on the 5 nm thick rubrene film have been carried out in $\vartheta/2\vartheta$ configuration. During the measurements the sample was kept in a position such that the scattering vector **Q** remains normal to the sample surface for the whole scanning, so that the only observed reflections are those coming from the families of lattice planes parallel to the substrate surface. Using such a geometry most of the diffracted intensity would come from the thick KAP crystalline substrate, whose strong diffraction peaks would hide the weaker peaks originating from the thinner overlayers.

In order to get rid of this problem the whole rubrene/α-4T heterostructure has first been stripped out of the KAP substrate by a wet transfer method[123, 124] and attached to the surface of a Silicon (1 0 0) wafer, whose diffraction peaks are far from the diffraction peaks of the overlayers. After the transfer procedure the film have first been checked again with the AFM, in order to verify that the film morphology was not altered during transfer.

The measurements have been carried out using a Cu-K_α X-ray source, and the resulting diffractogram is shown in figure 4.13. All the observed diffraction peaks can be easily indexed, and all of them unambiguously correspond either to the (0 0 l) family of planes of the α-4T crystalline phase (labeled in black) or to the (h 0 0) family of planes of the rubrene orthorhom-
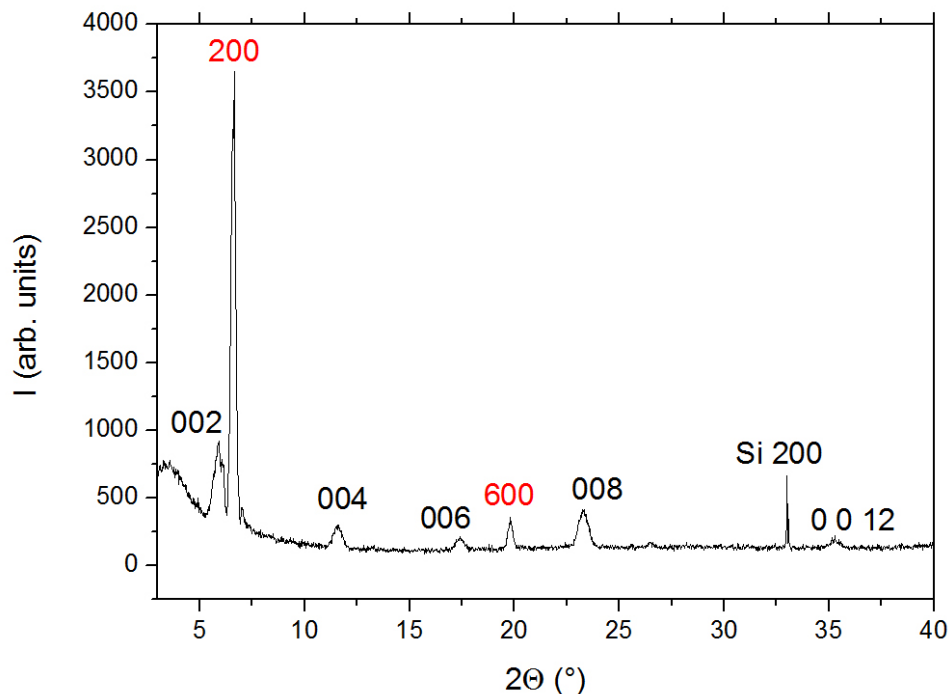
Figure 4.13: X-ray diffractogram collected in $\vartheta/2\vartheta$ geometry with a Cu-K_α X-ray source, from a rubrene thin film with a nominal thickness of 5 nm grown on top of a 8 nm thick α-4T film. The (0 0 l) peaks (labeled in black) arise from the α-4T substrate, while the (h 0 0) peaks (labeled in red) are due to the rubrene overlayer. The silicon (2 0 0) peak (Si 2 0 0) originates from the silicon substrate used as a rigid support for the heterostructure.

bic phase (labeled in red), thus confirming the out-of-plane packing of the rubrene molecules inferred from the AFM measurements. In the diffraction pattern the Silicon (2 0 0) peak can also be distinguished offering a mean to check the calibration of all the observed peaks positions. Also, the relative intensities of the α-4T and rubrene diffraction peaks perfectly corresponds to those expected from the ratio between the nominal thicknesses of the two layers, as measured during the deposition by the quartz microbalance. Finally, the rubrene diffraction peaks appear very sharp, even sharper than the α-4T ones, thus indicating a very high degree of crystalline quality of the rubrene overlayer, despite the lower order of the α-4T substrate[103].
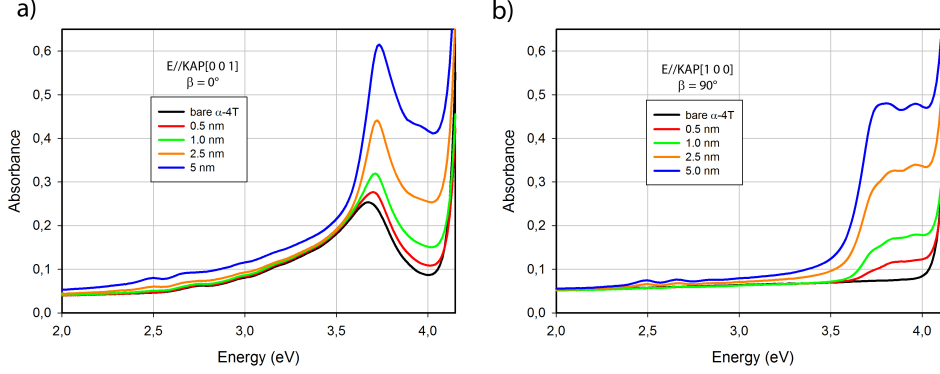
Figure 4.14: Normal incidence absorption spectra collected from samples with increasing film thickness and with light linearly polarized (*a*) with **E**//KAP[0 0 1] (*β* = 0°) and (*b*) with **E**//KAP[1 0 0] (*β* = 90°). The black line refers to the spectrum of the bare α-4T(0 0 1)/KAP(0 1 0) heterostructure.

Optical measurements

The results already reported in the literature regarding the characterization of α-4T films grown on rubrene single crystals show that the overlayer grows on the substrate according to the α-4T<1 1 0>//RUB<0 2 1> epitaxial relationship, leading to four possible in-plane orientations of the α-4T film[83]. In order to verify if the same is valid also for the inverse heterostructure we made use of polarized absorption spectroscopy. This way, exploiting the highly anisotropic absorption properties of rubrene and α-4T it is possible to get some insight into the relative in-plane ordering of the two layers.

The polarized absorption spectra analyzed in the following paragraphs have been collected by using a double-beam spectrometer (Lambda 900, Perkin Elmer) equipped with Glan-Taylor polarizers and a depolarizer. Before being inserted into the instrument the samples have been masked for avoiding stray-light collection, which negatively affects absorption lineshape.

Figure 4.14 shows the evolution with nominal thickness of the rubrene thin film of the normal incidence absorption spectra of the rubrene(2 0 0)/α-4T(0 0 1)/KAP(0 1 0) heterostructure. The spectra have been collected under linearly polarized light, with the electric field vector **E** parallel (figure 4.14a) and normal (figure 4.14b) to KAP[0 0 1] (*β* = 0° and 90°, here after). These two directions have been chosen since they give the maximum optical anisotropy.

The presence of optical anisotropy even for the thinner films is a clear signature of their crystallinity; in particular, the typical optical response of rubrene can be clearly detected in the spectra collected for $\beta = 90°$, where the α-4T thin film is almost transparent (see for comparison the spectrum collected before rubrene deposition, reported in black). Indeed, a broad peak centered about 3.8 eV increases in intensity and becomes more and more structured with increasing film thickness.

For $\beta = 0°$, the optical response of rubrene can not be easily detected, being overlapped to that of α-4T. Nonetheless, for higher thicknesses the strong absorption peak at 3.68 eV, attributed to α-4T, increases in intensity, shifts towards higher energy (at 3.72 eV for the 5 nm thick rubrene film) and becomes sharper. Moreover, a further broad peak at about 3.9 eV arises. All these features of the high energy region of the spectra clearly give the optical signature of crystalline rubrene, which is characterized by the presence of strong and polarized optical transitions at about 3.7, 3.8 and 3.9 eV, which in amorphous rubrene films are merged in a unique broader peak centered at about 4 eV[29, 58, 83, 125].

Looking at the low energy portion of the spectra, two peaks at 2.49 and 2.66 eV can be clearly detected under any light polarization only in the spectra relative to the 5 nm thick rubrene thin film. These two peaks are typically observed for light polarized along any lattice direction of crystalline rubrene or even in amorphous rubrene[125], but they display an absorption coefficient about one order of magnitude lower than the higher energy peaks, thus being detectable only in the thicker films.

It is known that both amorphous and crystalline rubrene display another absorption peak at a lower energy, namely at 2.33 eV, not detected under these experimental conditions. Since in crystalline rubrene this peak originates from an excitonic transition polarized along rubrene[1 0 0], its absence from the normal incidence absorption spectra is a further confirmation that the rubrene crystalline domains have their (1 0 0) surface parallel to the substrate surface, as already suggested by AFM and X-ray diffraction measurements. Indeed, by means of oblique incidence absorption spectroscopy, whose results are shown in figure 4.15, it has been possible to observe that the peak at 2.33 eV arises again, since a component of the electric field probes the [1 0 0] direction, perpendicular to the film surface.

Notwithstanding the complete out-of-plane orientation of rubrene crys-
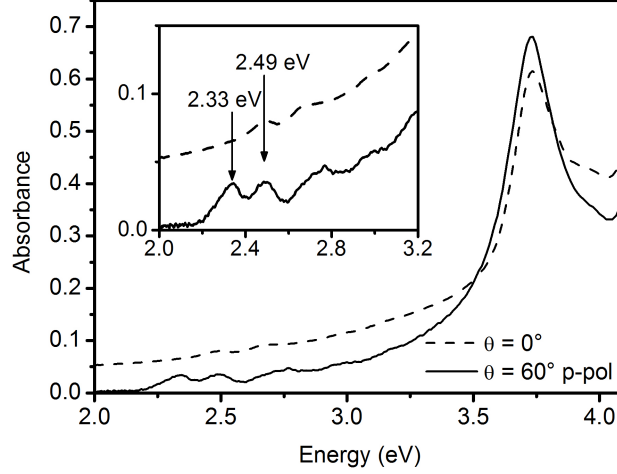
Figure 4.15: Normal incidence absorption spectrum of a 5 nm thick rubrene thin film on an α-4T(0 0 1)/KAP(0 1 0) heterostructure for $\beta = 0°$ (dashed line) together with an oblique incidence absorption spectrum (straight line) collected by selecting KAP(1 0 0) (and thus α-4T(0 1 0)) as plane of incidence and p-polarization. Inset: magnification of the same spectra in the $(2 \div 3.2)$ eV energy range.

talline domains, their in-plane orientation with respect to that of the underneath α-4T(0 0 1) layers is not unique. By taking into consideration the optical response of rubrene single crystals, the high energy peak of crystalline rubrene centered at about 3.7 eV should be detectable for light polarized along rubrene[0 0 1], whilst the peaks at about 3.8 and 3.9 eV along rubrene[0 1 0] [58]. In figure 4.14 these absorption peaks possess similar intensity: this is particular evident in the $\beta = 90°$ spectra, being not affected by the strong absorption of α-4T. The presence of several in-plane orientations which can be identified is therefore assessed. In the previous studies on the inverted heterostructure, we found that RUB(1 0 0) and α-4T(0 0 1) surfaces are characterized by the presence of peculiar surface corrugations along α-4T<1 1 0> and rubrene<0 2 1>, driving the epitaxial growth. Therefore four azimuthal orientations of the α-4T(0 0 1) domains could be found, identified by $\vartheta = \pm7°$ and $\vartheta = \pm83°$, ϑ being the angle between rubrene[0 1 0] and α-4T[1 0 0]. Considering that a similar scenario takes place even in this case (since the contact surfaces are the same) and by taking into consideration the sensitivity of our macroscopic optical measurements, it is possible to conclude that two 'macroscopic' azimuthal domains at $\vartheta = 0°$ and $\vartheta = 90°$ are

present. Since the high energy peaks (in the $\beta = 90°$ spectra) of rubrene possess similar intensities, it can be also concluded that the two 'macroscopic' azimuthal orientations also have a similar statistical weight.

Comparison with calculations

The analysis presented in the previous paragraphs gave consistent and clear results, but, due to its macroscopic nature, it can not give insights neither on the true epitaxial relationship between the two materials nor on the microscopic orientation mechanisms. Empirical force-field atom-atom potential simulations, on the other hand, were found to be a powerful tool for predicting and explaining the occurrence of specific azimuthal orientations in terms of adhesion energy of the overlayer-substrate interface[74, 77, 83, 110, 126–130].

Simulations of possible epitaxial relationships between an α-4T(0 0 1) substrate and a rubrene(2 0 0) overlayer were thus carried out by means of atom-atom empirical potentials[131] and exploiting the capability of Lamarckian genetic algorithms to efficiently explore the configuration space. A monomolecular (2 0 0) slice of the rubrene orthorhombic polymorph made of 16 rubrene molecules is considered as overlayer, while the substrate is built with a bulk terminated α-4T(0 0 1) slab of the low temperature polymorph. The slab comprised $21 \times 15 \times 1$ unit cells along the a, b, and c axis, respectively, giving rise to a total of 1260 molecules. The size of overlayer and substrate models were selected on the basis of the results of the previously cited studies about other organic-organic and organic-inorganic systems. Simulation of the rubrene(1 0 0)$\|\alpha$-4T(0 0 1) interface was performed by means of 1240 docking runs with a rigid overlayer free to move and interact with a rigid substrate surface. The AutoDock3 package[132] was used to efficiently explore the configuration space without biases over the azimuthal orientations.

The results of these calculations for the rubrene(1 0 0)$\|\alpha$-4T(0 0 1) interface are reported in figure 4.16 in terms of adhesion energy averaged over the number of rubrene molecules defining the overlayer island. The data have also been symmetry averaged to span the $0° \div 180°$ range, owing to the C_2 symmetry of the rubrene(2 0 0) layers, and the isolated dots at the bottom of each peak are the best estimate of the adhesion energy for each azimuthal angle, obtained by full minimization after the docking trials. The azimuthal
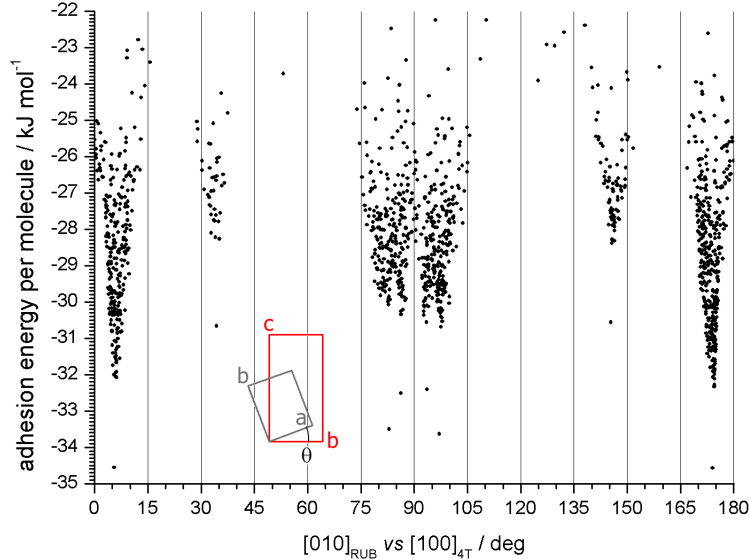
Figure 4.16: Results of empirical force-field atom-atom potential simulations for the adhesion energy of the rubrene(100)$\|\alpha$-4T(001) interface. Each point in the plot represents the result of a single calculation, carried out at a different reciprocal orientation of the two molecular layers. The energy values reported in the vertical axis represent the adhesion energy averaged over the number of rubrene molecules defining the overlayer island. The azimuthal angle ϑ is that defined by the scheme superimposed to the plot, where the rubrene primitive cells of rubrene and α-4T are reported in red and gray, respectively.

angle ϑ is measured between the **a** axis of α-4T and the **b** axis of rubrene, as shown in the scheme of the unit cells superimposed to figure 4.16.

These results show that the potential energy of the heterostructure interface is strongly dependent on the azimuthal orientation of the rubrene(2 0 0) island with respect to the α-4T(0 0 1) substrate. In particular, eight peaks corresponding to favorable azimuthal orientations are present:

- Two quasi symmetrical and sharp peaks, characterized by the lowest adhesion energy of $-34.6\,\mathrm{kJ\,mol}^{-1}$ per molecule in the overlayer, centered at $\vartheta = 6°$ and $\vartheta = 174°$;

- four poorly resolved peaks, differing by $\approx 1 \div 2\,\mathrm{kJ\,mol}^{-1}$ per molecule, compared to the previous ones, and centered at $\vartheta \approx 83°$, $86°$, $94°$ and $97°$. This distribution could be symptomatic of frustration of the overlayer in finding the best azimuth around $\vartheta = 90°$, a feature than could have been partly induced by the limited size of the simulated system. The minimized configurations with $\vartheta = 82.9°$ and $\vartheta = 97.1°$ lie at

$\approx -33.5\,\mathrm{kJ\,mol^{-1}}$, while those at $\vartheta = 86.3°$ and $\vartheta = 93.7°$ correspond to an adhesion energy of $\approx -32.5\,\mathrm{kJ\,mol^{-1}}$;

- two other minima, definitely less relevant for describing potential epitaxial relationships, centered at $\vartheta \approx 34°$ and $145°$ and corresponding to an adhesion energy of $-30.6\,\mathrm{kJ\,mol^{-1}}$ per molecule.

Compared to the experimental findings previously discussed, suggesting two almost equivalent epitaxial populations with ϑ close to $0°$ and $90°$, these results are in good agreement, providing values of $\vartheta = 6°$ and $174°$ for the absolute minima and $\vartheta = 83°$ and $97°$ for the next energy minima. This leads to an epitaxial relationship close to rubrene<0 2 1>||α-4T<1 1 0> for the rotational domains with $\vartheta = 6°$ (rubrene[0 2 1]||α-4T[1 1 0]) and $\vartheta = 83°$ (rubrene[0 2 1]||α-4T[1 $\bar{1}$ 0]). Since there is a quasi coincidence of non-primitive reciprocal lattice vectors, the epitaxy is of the line-on-line kind, as previously found for the case of rubrene films grown on tetracene and for most organic-organic epitaxial systems[106]. A molecular model of the heterostructure, showing both the possible azimuthal orientations of the rubrene crystalline domains along with the relevant lattice directions of the system, is reported in figure 4.17.

4.4 Conclusions

In this chapter the results of the structural characterization of rubrene crystalline thin films grown by OMBE on top of two different substrates, has been reported. In the first case the substrate consisted of centimeter sized tetracene single crystals exposing the (0 0 1) surface and grown by physical vapor transport. Rubrene thin films grown on these substrates have been characterized by means of AFM imaging and GIXD measurements and it has been observed that the molecules forming these films are packed according to the rubrene orthorhombic crystalline phase, with the (2 0 0) lattice plane parallel to the substrate surface and with a unique in-plane orientation, described by the epitaxial relationship rubrene[0 2 1]//tetracene[1 $\bar{1}$ 0]. This result is of particular importance, since it demonstrates the possibility to grow rubrene crystalline thin films with a single in-plane orientation by selecting the proper substrate. This opens up the possibility to fabricate electronic devices with rubrene thin films as their active layer and with transport properties close to those of rubrene single crystal based devices.
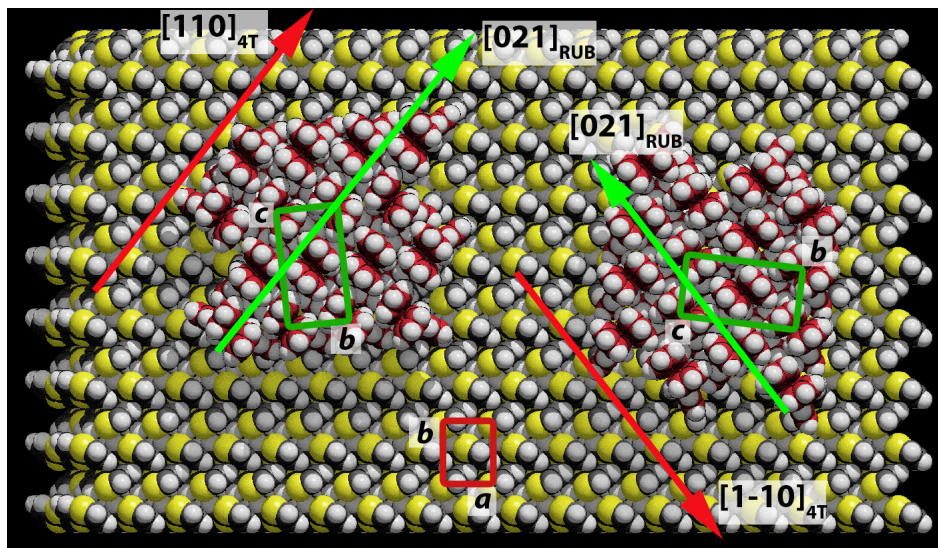
Figure 4.17: Top view of the molecular model of the rubrene/α-4T heterostructure, showing two different rubrene crystalline domains with an azimuthal angle $\vartheta = 6°$ (*left*) and $\vartheta = 83°$ (*right*). The unit cell and the relevant lattice directions for both α-4T and the two differently orientated rubrene domains are reported in red and green, respectively.

In the second part of this chapter, the epitaxial growth of rubrene over an α-4T/KAP heterostructure have been studied by means of polarized optical absorption and AFM measurements and, also thanks to a comparison with the results of numerical calculations, it has been possible to fully determine the in-plane ordering of the overlayer. In particular it has been demonstrated that rubrene epitaxial thin films grown on α-4T films are crystalline, and grow with four different in-plane orientations, all due to the same epitaxial relationship: rubrene<0 2 1>//α-4T<1 1 0>. This result demonstrates the feasibility of exploiting α-4T and rubrene as coupled layers in the fabrication of organic cascade solar cells, in which the α-4T layer serves also to induce the growth of rubrene crystalline thin films.

Chapter 5

Oxidation dynamics of rubrene epitaxial thin films

5.1 Introduction

As shown in chapter 4, rubrene crystalline thin films with a unique in-plane orientation can be grown on the surface of tetracene single crystals. In order for such films to be exploited for the development of electronic devices it is mandatory to get some knowledge about the effects of their exposure to ambient conditions, in particular with respect to their oxidation, which is particularly relevant for rubrene, as discussed in chapter 2.

In this chapter we thus present the results of the study the evolution of the morphological and electrostatic properties of rubrene epitaxial thin films grown on tetracene upon their exposure to ambient conditions. The films used for these studies have a thickness of few molecular layers (up to 3 or 4 molecular layers); this way their surface-to-volume ratio is maximized, thus enhancing the effects of the interaction with air and making such effects more easily noticeable. Additionally, the presence of uncovered substrate areas permits a direct comparison of the surface potential of the rubrene thin film, which evolves with time, with the constant surface potential of the tetracene crystal surface.

By a combination of Kelvin probe force microscopy (KPFM) and AFM morphology and phase contrast mapping with measurements and calculation of the electrostatic and structural properties of pure rubrene endoperoxide layers, it has been possible to determine the oxidation dynamics of such films,

in correlation with the evolution of their surface morphological, structural, and dielectric properties. The results reported in this chapter demonstrate that the oxidation of rubrene crystalline thin films leads to the formation of ordered crystalline layers of rubrene endoperoxide, opening up an interesting scenario in the field of organic electronics, revealing the possibility to control the growth of a *native* crystalline oxide layer on the surface of a crystalline thin film of an organic semiconductor. This prerogative allows the prediction of rubrene technology as somehow similar to the well assessed silicon technology, with the significative advantage of easier technological steps and much lower process temperatures.

5.2   Growth of rubrene thin films

Tetracene (2,3-benzanthracene, $C_{18}H_{12}$) single crystals were grown from commercial powder (Sigma-Aldrich, 99.9%) by physical vapor transport at $186\,°C$ and with a constant $20\,ml\,min^{-1}$ flux of nitrogen. The crystals obtained expose the (0 0 1) surface, have a lateral size of few millimeters, and a thickness of some hundreds nanometers.

In order to be able to carry out KPFM measurements these crystals have been attached to the surface of glass substrates covered by an indium-tin-oxide (ITO) layer, where they spontaneously adhere thanks to electrostatic interactions. The ITO layer has a sheet resistance of $30 \div 60\,\Omega/\square$ and a surface roughness of $3.6\,nm$ (rms) over a $1\,\mu m^2$ area.

Rubrene thin films with a nominal thickness of $1\,nm$ were grown on the surface of the tetracene crystals in ultra high vacuum conditions (pressure lower than $10^{-9}\,mbar$) by OMBE. During the growth process, the substrate has been kept at room temperature. Rubrene powder has been sublimated in the Knudsen cell at $160\,°C$ reaching a deposition rate of about $1\,Å\,min^{-1}$. This whole procedure is the same already reported in chapter 4, leading to well organized and highly crystalline rubrene thin films.

5.3   Results

5.3.1   Film morphology and time evolution

Once the growth process ended, the samples have been brought to ambient pressure and, after a brief exposure to ambient light for triggering oxygen

diffusion within the film[32], observed *ex-situ* with a Nanoscope Multimode V (Veeco) AFM, equipped with a J type piezoelectric scanner.

The tips used to collect the images were silicon nitride tips coated with platinum (NT-MDT), with a typical force constant of $40\,\mathrm{N\,m^{-1}}$ and a tip curvature radius of $36\,\mathrm{nm}$. The conductive Pt coating is needed in order to be able to later carry out KPFM measurements. All the collected images have a 512×512 pixels lateral resolution and have been collected at a $0.7\,\mathrm{Hz}$ scan rate. The analysis carried out on the collected AFM images were conducted with the SPM image analysis software Gwyddion (version 2.20) and with the Nanoscope software (version 7.30).

Figure 5.1 shows the morphological AFM image of a $10 \times 10\,\mathrm{\mu m^2}$ region of the surface of a $1\,\mathrm{nm}$-thick rubrene film deposited on the (0 0 1) surface of a tetracene single crystal, collected $80\,\mathrm{min}$ after sample extraction from the growth chamber and subsequent exposure to air. Observing the surface of the sample, one can notice the presence of the surface steps of the original surface of the tetracene crystal, roughly parallel to the horizontal axis of the image, and of several rubrene islands (the brighter areas of the image), some of which are lined up with the steps on the substrate surface. Magnifications of the four areas evidenced in figure 5.1 are reported in the first row of figure 5.2. All the rubrene islands have a molecularly flat surface, displaying a height of $(1.4 \pm 0.1)\,\mathrm{nm}$ or $(2.7 \pm 0.1)\,\mathrm{nm}$, as can be seen from the cross-sectional profile reported below the AFM image in figure 5.1. These two values match, within the experimental error, with integer multiples of the spacing between (2 0 0) planes of the rubrene orthorhombic crystal ($d_{(200)} = 1.343\mathrm{nm}$)[46]. Considering that the surface of the islands is molecularly flat, that their thickness is an integer multiple of the separation between the (2 0 0) planes of orthorhombic rubrene, and that these planes separate single molecular layers, we can conclude that the rubrene islands are indeed crystalline and exposing the (2 0 0) surface of the orthorhombic phase, in agreement with the results already reported in chapter 4.

In the four columns of figure 5.2, the evolution with time of the morphology of the film surface in the four regions highlighted in figure 5.2 is shown. AFM images were collected, going from top to bottom, after 80(1.3), 210(3.5), 4200(70) and 18880(315) min(hours) of exposure to air. It can be observed that the islands with the thickness of a single rubrene molecular layer can evolve in two different ways. They can either disappear, with the
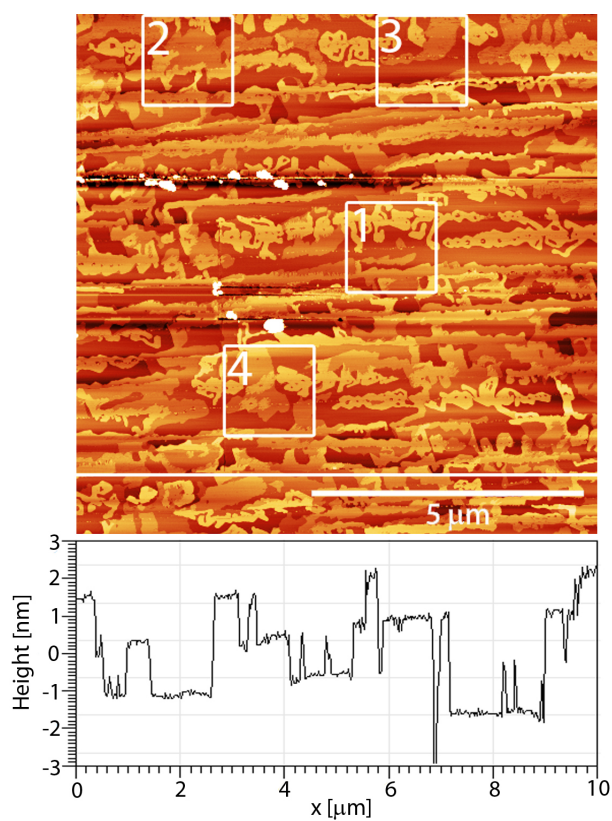
Figure 5.1: *Top*: Morphological AFM image of a $10 \times 10 \ \mu m^2$ area of the surface of a tetracene single crystal covered by rubrene islands, collected $80 \ min$ after its exposure to air. The numbers identify four specific $1 \times 1 \ \mu m^2$ regions of the sample surface, whose evolution with time is tracked in figures 5.2 and 5.4. *Bottom*: Cross-sectional profile taken along the scan line highlighted on the AFM image.
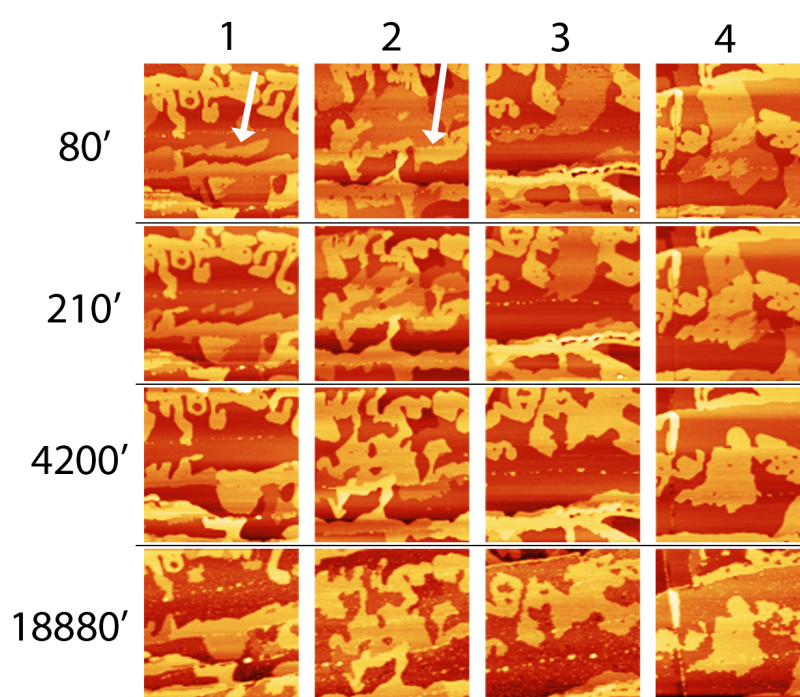
Figure 5.2: AFM morphology images collected over the four 1×1 µm² areas evidenced in figure 5.1. In each column are reported the images of a specific area, while each row, from top to bottom, corresponds to images collected respectively 80, 210, 4200 and 18 880 min after the extraction of the sample from the deposition chamber. The arrows in the first two images indicate specific features of the surface that will also be identified in the KPFM images reported in figure 5.4, in order to make the comparison between morphological and KPFM images easier.

progressive migration and/or desorption of the rubrene molecules constituting them (as for the island indicated by the arrow in the first column of figure 5.2), or they can be progressively covered by another layer of molecules (as the widest island in the second column of figure 5.2). For most of the islands, however, the two processes occur simultaneously, with progressive erosion of the island borders and the formation of a new monomolecular layer starting from the central region of the island (as for the larger islands shown in the third and fourth columns of figure 5.2). These observations can be explained assuming that there is a mass transfer from the edge of the one-layer thick islands to the top of them or to nearby islands, until all islands have a thickness of about two molecular layers. Indeed, after enough time has passed (figure 5.2, third row), all the islands that were previously only partially covered by a second molecular layer have reached a thickness of at least two molecular layers. Due to the long time the sample is left unscanned in between consecutive frames, we can definitely exclude a major effect of the scanning itself on the observed structural modifications. Finally, in the fourth row of figure 5.2, where images collected after 13 days of exposure to air are reported, the surface exhibits a spotted background, giving evidence of the onset of a deeper and less controlled degradation[133].

In figure 5.3a and b, morphological and phase contrast images of areas 3 and 4 from figure 5.1, respectively, are reported, as collected simultaneously to those reported in the first three rows of figure 5.2. It can be noticed that in both regions, while the bare tetracene surface always appears with a dark contrast in the background of the phase images, rubrene domains may appear with one of two different contrasts, and that the phase contrast evolves with the passing of time. By comparison between the evolution of morphological and phase contrast images, one can realize that the molecular layers growing during observation appear with a bright contrast, whereas the surface of islands already present on the sample from the beginning appears with dark contrast. Since, in general, collecting phase contrast images permits to distinguish areas of a surface with different structural and/or mechanical and/or chemical properties (see chapter 3), this means that the new molecular layers forming in air are structurally and/or chemically different from those formed during film deposition in vacuum.

Phase contrast images are particularly useful since they permit an easy and fast discrimination between surface areas with different intrinsic proper-
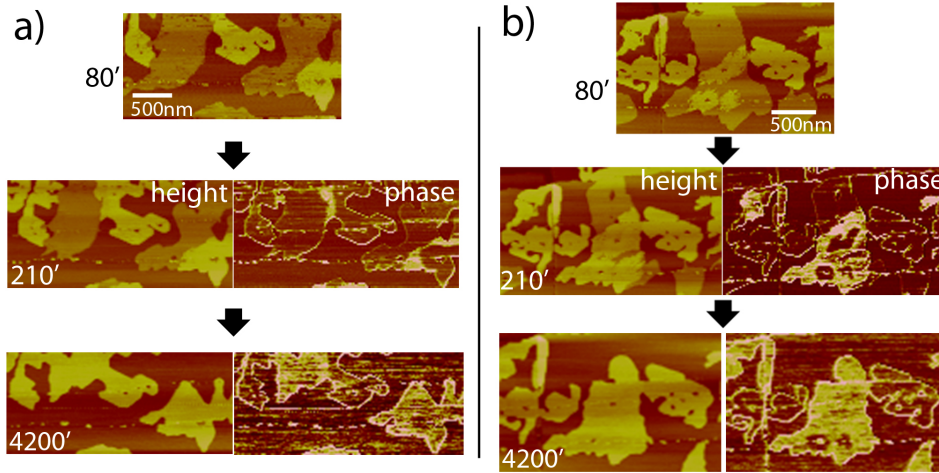
Figure 5.3: (*a*) In the first row the magnification of area 3 highlighted in the morphological AFM image in figure 5.1 is reported. On the second and third row are reported the morphological (*left*) and phase contrast (*right*) images of the same area collected 130 min and 4120 min afterward, respectively. (*b*) The same as panel (*a*) but for area 4 of figure 5.1.

ties but that look indistinguishable with respect to their morphology. Unfortunately, phase contrast images alone can not provide quantitative information about the actual nature of regions with different phase contrast. Thus, in order to get some insights into the differences between the pristine molecular layers and those formed in air, we simultaneously measured the surface potential (SP) of the samples, by collecting KPFM images of its surface. By these means it has been possible to both follow the evolution with time of the SP and to extract quantitative data from the measured SP values that help to understand the actual nature of the new layer.

5.4   Surface potential measurements

In order to be able to collect KPFM images, the surface of the ITO covered glass has been grounded, contacting it to the AFM scanner using conductive carbon paste. KPFM images were collected simultaneously to the corresponding morphological images in *lift-mode*, with a lift height of 5 nm, in order to maximize the lateral resolution[134] and in-between successive measurements the samples were kept under ambient conditions. All the measurements were performed under ambient light and in air. Relevant effects of water adsorption on the measurements have been excluded
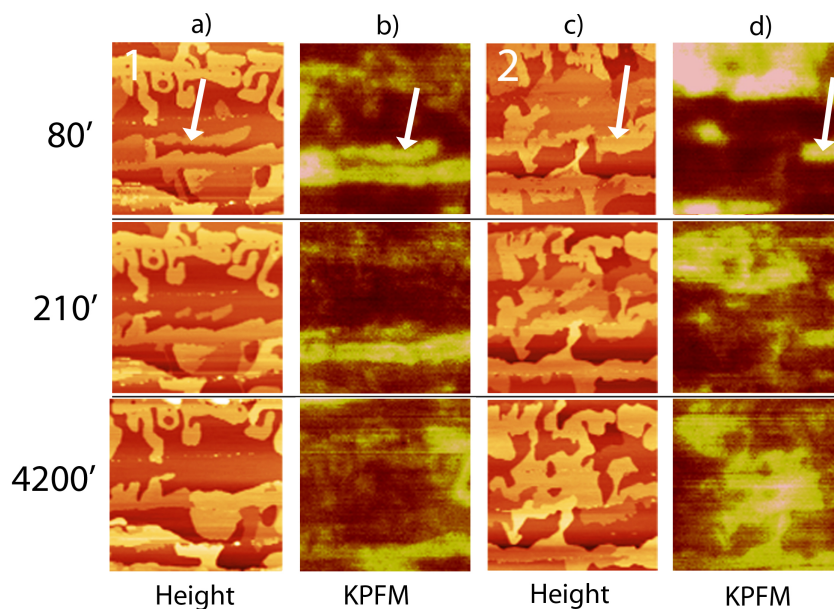
Figure 5.4: AFM morphology and KPFM images collected over the areas 1 and 2 of figure 5.1: column a) shows morphological images of area 1 (as the first column of figure 5.2); column b) shows KPFM images of area 1; column c) shows morphological images of area 2 (as the second column of figure 5.2); column d) shows KPFM images of area 2. From top to bottom, the rows correspond to images collected 80 min, 210 min, and 4200 min after the extraction of the sample from the growth chamber, respectively. The potential scale for all the KPFM images is 200 mV. The arrows in the first row indicate specific features of the images, in order to make the comparison between morphological and KPFM images easier.

by checking that no substantial variation of the measured surface potential occurred when dry nitrogen atmosphere was used. We estimated that in our case the typical statistical error in surface potential estimation using the KPFM technique is about ± 40 mV.

In columns b) and d) of figure 5.4, KPFM images of the same areas shown in the morphological images reported in columns a) and c) of the same figure (and in the first two columns of figure 5.2), respectively, and collected simultaneously to them, are reported. Comparing each KPFM image with the corresponding morphological image, it is clear that some of the islands show the same SP as the substrate, while others have a higher SP value. In particular, while all the islands with a thickness corresponding to that of a single molecular layer do show a difference between their SP and that of the substrate, some of the thicker islands do not. As can be observed for the area indicated by the arrow in the columns a) and b) of figure 5.4,

the regions of the substrate that become uncovered with time acquire the same SP of the rest of the substrate surface, while all the layers growing in air during observation have, from the beginning, a larger SP with respect to that of the substrate (like the layer whose progressive formation is shown in columns c) and d)). From these first observations it is clear that both the tetracene substrate and the pristine rubrene molecular layers have the same SP value and that, while the SP of the substrate does not change with time, the SP of the rubrene layers formed during the sample exposition to air is different (larger) from that of the layers formed during the ultra high vacuum deposition.

In order to obtain quantitative and reliable data from KPFM measurements, and thus to be able to identify the newly formed molecular layer, one has first to keep into account the broadening effects due to the tip finite size and to its long range interactions with the sample surface. Indeed, the longer range of the electrostatic interactions involved in KPFM measurements, in comparison to the shorter range of the van der Waals interactions responsible for the standard AFM working modes (see chapter 3), leads to lower lateral resolution with respect to that of AFM morphology images and, for the smaller structures (with lateral dimensions of the order of the effective sample area interacting with the tip, or smaller), to measured SP values different from the real ones[94, 95]. Thus, the actual SP values can only be obtained by following one of two possible routes:

1. measuring only the SP of structures wider than the tip-sample interaction area;

2. carrying out a deconvolution of the measured signal from the transfer function describing the tip and its interactions with the sample surface.

Carrying out the deconvolution is in general a complex process, since one has first to identify the proper transfer function describing the particular tip-sample interaction in play[135, 136]. Nevertheless, there are specific situations in which this process can be simplified; for instance, when measuring structures with an high aspect ratio, it is possible to carry out the deconvolution in one dimension following Ref. [137], greatly simplifying the required calculations. This can be done by fitting the KPFM profile of the imaged

structure with the following function:

$$Y = \Delta SP \cdot \frac{1}{1 + e^{\left(\frac{x - w_m/2}{d}\right)}} \cdot \frac{1}{1 + e^{\left(-\frac{x + w_m/2}{d}\right)}} + SP_2 \qquad (5.1)$$

where $\Delta SP = SP_1 - SP_2$, SP_1 is the absolute SP of the structure, SP_2 is the substrate absolute SP, w_m is the structure width (as measured from the topographic image), and d is a parameter accounting for the effective area $w_{eff} \approx 4d$ of the sample interacting with the tip during KPFM imaging. If the uncovered substrate area surrounding the measured structure is large enough, the measured and effective SP values of the substrate are equal, and then, fitting the measured profile to equation (5.1), it is possible to determine both ΔSP and d as best fit values.

Following this procedure for some of the structures with higher aspect ratio in our KPFM images, it has been possible to determine that, under our experimental conditions, $w_{eff} \approx 200$ nm. Thus, it is possible to get reliable SP values without the need for further calculations from structures with lateral size larger than 200 nm.

Another effect to be considered when measuring the SP of a molecular layer with KPFM is the contribution of the polarization induced on the molecules by the potential difference applied between the AFM tip and the sample surface to the measured SP. However, in our case the contribution of this effect to the measured SP can be neglected if compared to the contribution of the permanent dipole of the rubrene endoperoxide molecule (see next section for more details).

Thanks to these considerations, it has been possible to measure the actual values of the ΔSP between several islands and the substrate, performing KPFM measurements also on other regions of the previously observed film and on other rubrene films prepared under the same conditions, in order to get larger statistics. In figure 5.5, some selected morphological and KPFM images of the surface of some samples are reported. It is worth noting that some of the tetracene crystals showed a lower density of steps on their surface, enabling the growth of well-separated islands and then a more accurate estimation of their potential (see, e.g., figure 5.5c and d). The characteristics of the KPFM images are the same as those of figure 5.4, described above.

The SP values of all the observed islands appear to be distributed around two values, as shown in figure 5.6a and b, where the direct comparison of
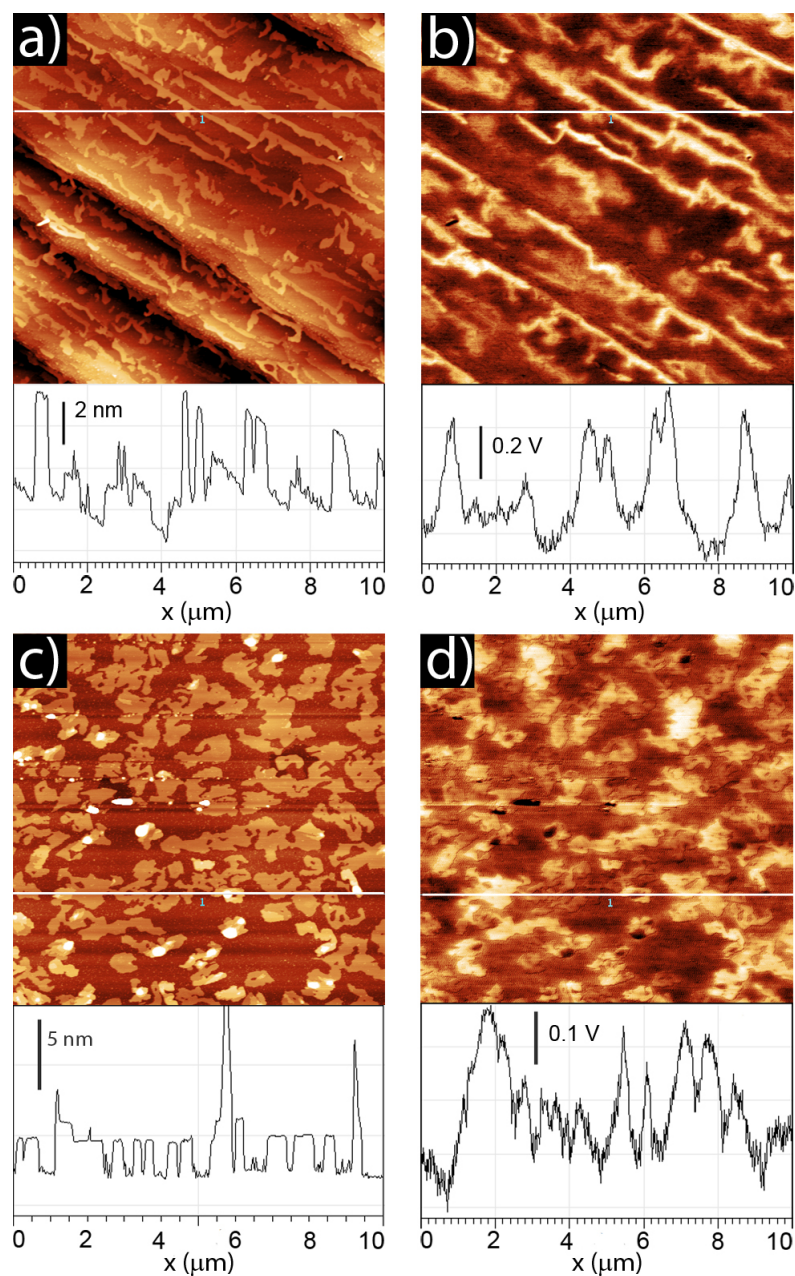
Figure 5.5: Height (a, c) and surface potential (b, d) maps of a 10×10 µm^2 region of the surface of two different rubrene thin films deposited on tetracene. Below each image, the cross-sectional profile taken along the highlighted scan line is reported.
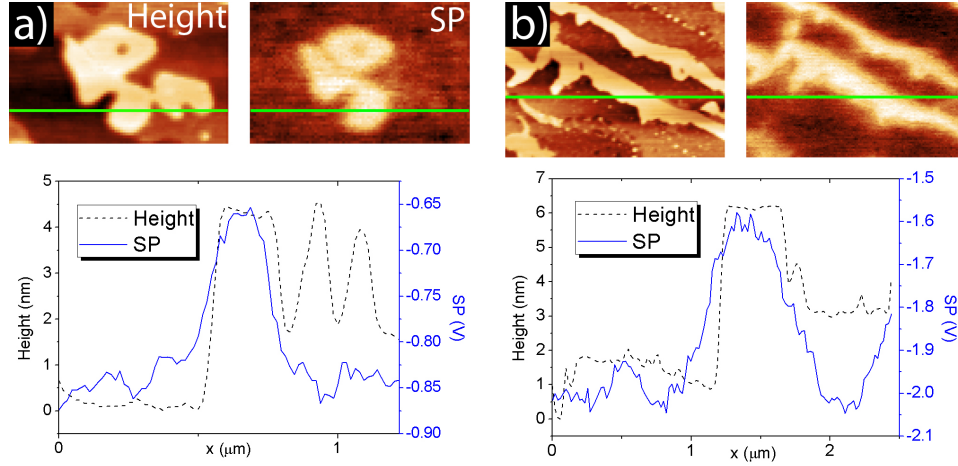
Figure 5.6: (*a* and *b*) Morphological (*left*) and KPFM (*right*) images of two selected rubrene islands collected from two different samples along with the respective cross-sectional profiles taken along the highlighted scan lines.

the KPFM and height images of two islands along with their cross-sectional profiles is reported. Considering all the ΔSP values measured for several islands of different films, we obtained the following estimates for the two ΔSP values: $\Delta SP_1 = (0.20 \pm 0.04)$ V and $\Delta SP_2 = (0.42 \pm 0.04)$ V.

5.5   Rubrene endoperoxide crystals and their electrostatic properties

All the morphological, physical-chemical and electrostatic transformations described so far are consistent with the formation of a foreign chemical species on the surface of the pristine rubrene crystalline domains, possibly induced by the sample interaction with air and ambient light. Since it is known that even crystalline rubrene oxidizes[19, 69], we now want to verify that what we are observing is indeed the progressive oxidation of rubrene molecules to rubrene endoperoxide. In order to do this it is necessary to quantitatively compare the experimental results reported above with the structural and electrostatic properties of rubrene endoperoxide crystals, considering their differences with those of crystalline rubrene. Thus, we present here the results of the structural characterization of rubrene endoperoxide crystals and of the calculations of their electrostatic properties, on which the full discussion of our results will be based.
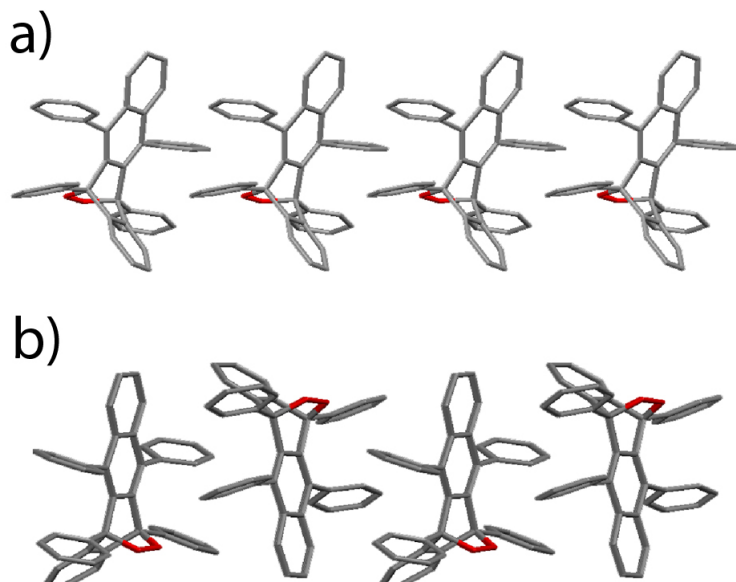
Figure 5.7: (*a*) Structural model of a molecular layer of rubrene endoperoxide molecules as arranged in the triclinic structure obtained from dioxane solution. (*b*) Structural model of a molecular layer of rubrene endoperoxide molecules, as arranged in the monoclinic structure obtained from anisole solution.

5.5.1 Growth and structural characterization of rubrene endoperoxide crystals

The source material for the crystal growth, rubrene endoperoxide, can be readily obtained by exposure to light of rubrene solutions, whose oxidation can be considered complete when their absorption spectra present negligible light absorption in the visible range[29, 125]. Rubrene endoperoxide powder can subsequently be obtained by recrystallization of the photo-oxidized product. Regrettably, rubrene endoperoxide is thermally unstable, giving rise to a reddish product if heated above 160 °C[43] and thus preventing the possibility to grow single crystals by thermal evaporation. Therefore, a number of methods for crystal growth from solution has been explored, leading to the identification of two different crystal structures for rubrene endoperoxide crystals.

Rubrene endoperoxide single crystals were grown from dioxane ($C_4H_8O_2$) and from anisole ($CH_3OC_6H_5$, methoxybenzene) solutions by slow isothermal solvent evaporation at 22 °C. The starting rubrene endoperoxide solutions were obtained by photo-oxidation of 10^{-3} M rubrene solutions kept in air un-

	Structure 1	Structure 2
Solvent	Dioxane	Anisole
Symmetry	Triclinic	Monoclinic
Space group	P$\bar{1}$	P2$_1$/c
a [Å]	7.62	11.26
b [Å]	11.16	21.33
c [Å]	22.66	13.62
α [°]	101.70	90
β [°]	94.31	101.80
γ [°]	97.87	90
Z	2	4

Table 5.1: Structural properties of the two different rubrene endoperoxide crystalline phases obtained by solution growth in dioxane (first column) and anisole (second column).

der a halogen lamp (16 W), whose complete oxidation, bringing to a colorless solution, was checked by a UV/Vis spectrophotometer.

The structure of the two kind of crystals has been determined by X-ray diffractometry carried out with a Bruker SMART APEX CCD diffractometer using Mo-K$_\alpha$ radiation ($\lambda = 0.71073$ Å). The structures were solved by applying direct methods techniques, as developed in program SIR2004[138]. Full-matrix least-squares refinement with anisotropic displacement parameters for non-hydrogen atoms was applied with SHELXL-97[139]. The procedure SQUEEZE as implemented in program PLATON was applied to the diffracted intensities giving a substantial improvement on the structural refinement[140]. All hydrogen atoms were riding about their pertinent carbon atoms.

The results of the structural characterization, showing that the crystals obtained from the two solutions belong to two different crystal systems, are reported in table 5.1.

Regrettably, both types of crystals include solvent molecules; however, an interesting common feature of both structures is the presence of segregated monomolecular layers of rubrene endoperoxide molecules, enabling the identification of a characteristic packing motif of aggregates of pure rubrene endoperoxide, which could eventually form on the surface of crystalline rubrene thin films. Models of these molecular packings within monomolecular layers of rubrene endoperoxide are reported in figure 5.7a and b, as extracted from
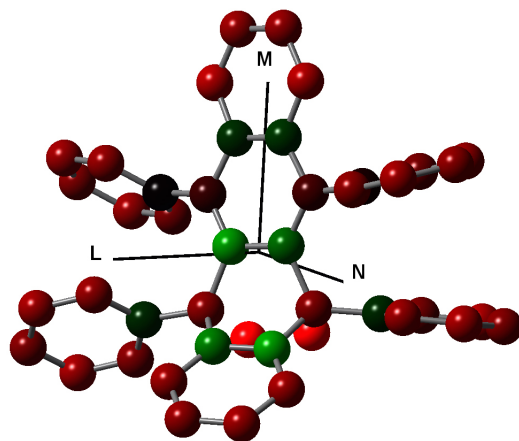
Figure 5.8: Ball-and-stick model of the molecular conformation of rubrene endoperoxide in its triclinic crystal polymorph (obtained from dioxane solution). The model is represented with a color scale evidencing partially negative (reddish) and positive (greenish) atoms, as obtained from Mulliken population analysis.

the structures of single crystals grown from dioxane and anisole solutions, respectively. Starting from these results it is now possible to determine the electrostatic properties of rubrene endoperoxide molecular layers.

5.5.2 Electrostatic properties of rubrene endoperoxide crystalline molecular layers

While a single rubrene molecule has no net dipole moment, the same do not apply for rubrene endoperoxide molecules, due to the bonding with two oxygen atoms and the consequent disruption of the planarity of the molecule tetracene backbone. The electrostatic properties of rubrene endoperoxide molecules were determined by performing density functional calculation using the Gaussian03 software and employing the B3LYP hybrid functional along with the 6-31G basis set[141]. Ground state properties of the rubrene endoperoxide single molecule have been obtained by geometry optimization in vacuum, starting from the available atomic positions of rubrene endoperoxide in crystals grown from dioxane solution. The ground state dipole moment has been found to be $\mathbf{d} = \{$-0.60, 1.04, -2.43$\}$ D in the $\mathbf{L},\mathbf{M},\mathbf{N}$ frame of reference of the molecular axes (shown in figure 5.8). Very similar results have been obtained starting from the slightly different geometry of rubrene

endoperoxide molecules in the other crystals, grown from anisole solutions.

In general, assuming a surface covered by an infinite homogeneous monomolecular layer of rubrene endoperoxide molecules, we can estimate the change in its electrostatic potential due to the dipole moment of the molecules to be: $\Delta V = d\varrho \cos(\vartheta_{tilt})/\varepsilon_0$, where d is the molecular dipole, ϱ is the surface density of molecules, ϑ_{tilt} is the angle formed by the molecular dipole with the surface normal, and ε_0 is the vacuum permittivity[142].

From the crystallographic data of rubrene endoperoxide crystals grown in dioxane, considering an (a,b) two-dimensional layer with one molecule per cell, we find $\varrho \approx 1.2$ nm^{-2} and $\vartheta_{tilt} \approx 79°$, obtaining $\Delta V \approx 0.23$ V. The sign of the change in the potential depends on the orientation of the molecules (and thus dipoles); in the special case we considered, both signs are allowed due to the presence of inversion symmetry in the packing structure. In the case of rubrene endoperoxide crystals grown in anisole, there are two molecules per two-dimensional cell, whose dipole moments have opposite projections on the surface normal, thus producing no net change in the electrostatic potential of the layer.

5.6   Discussion

In section 5.4 we have shown that, after enough time of sample exposure to ambient conditions, all the observed islands have one of two possible ΔSP values with respect to the substrate SP, namely: $\Delta SP_1 = (0.20 \pm 0.04)$ V or $\Delta SP_2 = (0.42 \pm 0.04)$ V. The smaller of these two ΔSP values corresponds, within the experimental error, to the ΔSP calculated in section 5.5 for a single rubrene endoperoxide molecular layer packed according to the triclinic structure of rubrene endoperoxide crystals, the other ΔSP value being almost exactly twice. Then, considering that rubrene molecules have no net dipole moment, and thus that a layer of rubrene molecules should not show a different SP with respect to the bare substrate, the measured SP values suggest the presence of islands comprising one or two molecular layers of rubrene endoperoxide molecules packed according to the motif shown in figure 5.7a. This direct correlation between the presence of a layer of permanent dipoles on a surface and the SP shift measured by KPFM has been already exploited in the study of self-assembled-monolayers formed on the surface of rubrene single crystals[143].
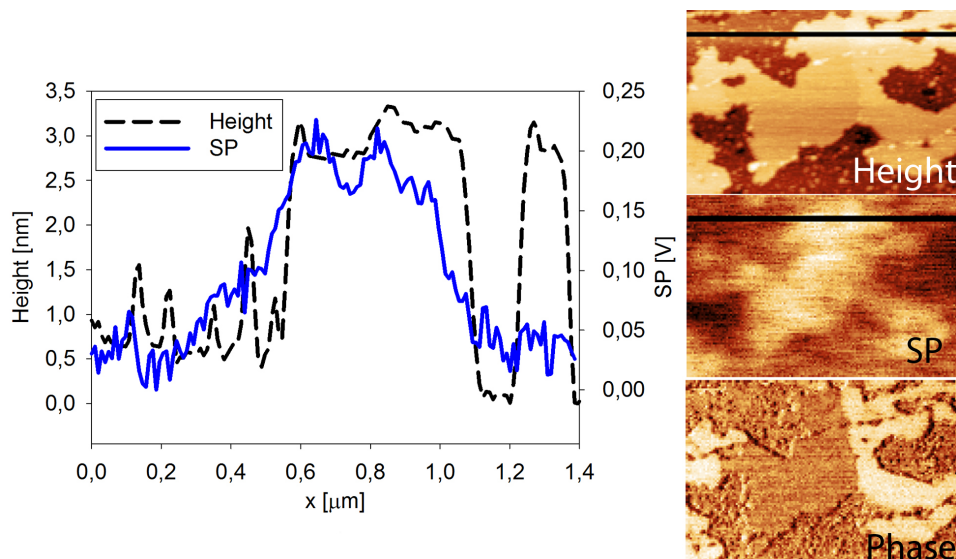
Figure 5.9: (*Right*) Here are shown, from top to bottom, the height image, the KPFM image and the phase contrast image of area 3 of figure 5.1, collected after 4200 min of exposure to air. (*Left*) Height (black dashed line) and surface potential (blue line) profiles taken along the same horizontal scan line, highlighted over the height image reported on the right.

As shown in the previous section about rubrene endoperoxide structure, the different configuration assumed by the oxidized rubrene molecule leads to different lattice parameters between the rubrene orthorhombic phase and the corresponding rubrene endoperoxide crystalline phase, in particular the triclinic one, leading to a matching with our findings about ΔSP. Indeed, if the observed ΔSP values are due to the formation of a rubrene endoperoxide molecular layer, there should be a thickness difference between islands showing a non-zero ΔSP and islands with zero ΔSP. In particular, a slightly different interlayer spacing between rubrene molecular layers in the **a** lattice direction of the orthorhombic phase and rubrene endoperoxide molecular layers in the triclinic phase is expected, the latter having a thickness lower by $\approx 0.2\,\text{nm}$. Indeed, as can be observed in figure 5.9, in which are reported the height, KPFM, and phase contrast images of area 3 of figure 5.1 (collected after 4200 min of exposure to air), differences in the SP and phase contrast directly correspond to a difference in the height of the island. In particular, the superposition of the height and SP profiles collected along the same scan line shows that an increase of the SP does correspond to a decrease in the height of the island. Measuring the height difference between adjacent

zones showing both a different SP and a different phase contrast, an average value of (0.25 ± 0.02) nm has been obtained, compatible with the value calculated for the height of a single rubrene endoperoxide molecular layer from the known crystalline structure of rubrene endoperoxide crystals grown from dioxane (figure 5.7a). This result corroborates the assumption that what we are observing are indeed crystalline rubrene endoperoxide molecular layers nucleated on top of rubrene crystalline domains.

Starting from these arguments it is finally possible to propose a feasible mechanism leading to the oxidation of epitaxially grown rubrene thin films. As already shown in chapter 2 it is known that, while amorphous rubrene films tend to completely oxidize very rapidly, rubrene single crystals do not, being the presence of rubrene endoperoxide molecules limited to the outermost molecular layers[19]. In full agreement with these findings, we found here that rubrene epitaxial domains with a thickness of two or more molecular layers behave as single crystals, oxidizing very slowly in comparison to the one-layer thick domains. In addition, the latter are also morphologically unstable, as demonstrated by the transfer of mass from their borders to their top, until a more stable configuration is reached. Moreover, rubrene molecules from these less stable layers oxidize, concurring to the formation of new molecular layers entirely constituted of rubrene endoperoxide molecules, packed accordingly to the crystalline structure of rubrene endoperoxide single crystals grown from dioxane solution. Nonetheless, after enough time has passed, also the thicker islands oxidize, as can be noticed in figure 5.5b and d, where all the islands have a positive ΔSP. This observation is also in accordance with the literature data cited in chapter 2, which shows the presence of rubrene endoperoxide in the outermost layers of rubrene monolithic crystals[19].

Finally, the positive sign of the measured ΔSP indicates an arrangement of the rubrene endoperoxide molecules with the oxygen atoms pointing downwards, as depicted in the model in figure 5.7a. These newly formed layers appear to be stable, possibly due to the interaction of both H- and O-atoms with the (2 0 0) surface of the underlying rubrene crystalline domains, enhancing surface adhesion. Such stability is definitely a very positive property, which permits to envisage a future rubrene-based technology in organic electronics, exploiting this native oxide layer.
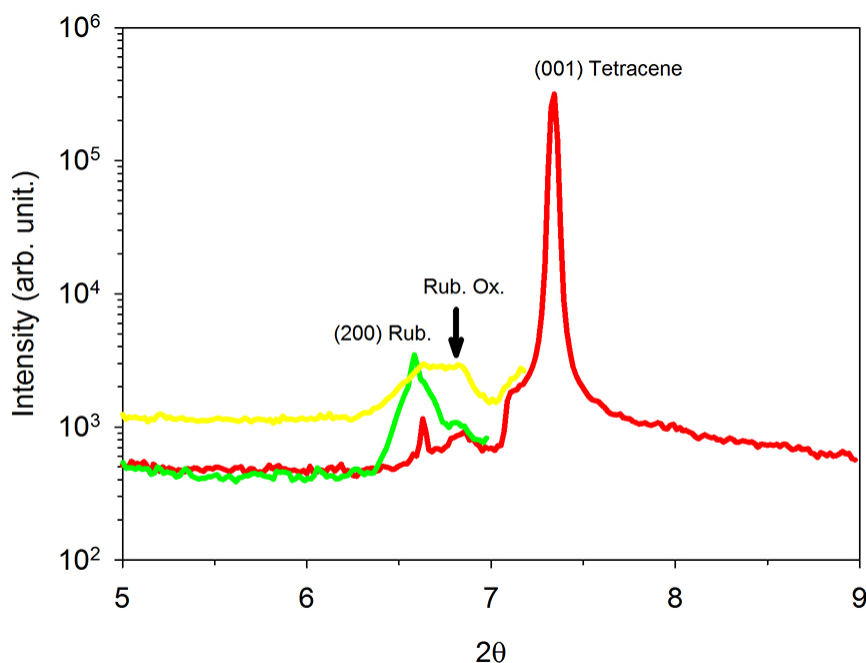
Figure 5.10: X-ray diffraction spectra collected in $\vartheta/2\vartheta$ configuration from three different rubrene thin films grown on tetracene with a thickness of $\approx 15\,\text{nm}$ and exposed to ambient air for several days. The measurements have been carried out with the sample surface parallel to the horizontal plane and with a Cu-K$_\alpha$ X-ray source.

5.7 Further evidence of the process

The formation of a native oxide layer upon rubrene thin film oxidation, proposed in section 5.6 as the mechanism behind the observed morphological and electrostatic evolution of such films during their exposition to air, is confirmed also by other experimental findings, briefly reported in this section.

5.7.1 X-ray diffraction measurements

In figure 5.10 several X-ray diffraction spectra collected with a $\vartheta/2\vartheta$ diffractometer using the Cu-K$_\alpha$ wavelength are reported as collected from various rubrene thin films with a thickness of $\approx 15\,\text{nm}$, grown by OMBE on tetracene single crystals and exposed to ambient air for several days. The measurements have been carried out with the samples oriented with their surface parallel to the horizontal plane, thus, according to the results
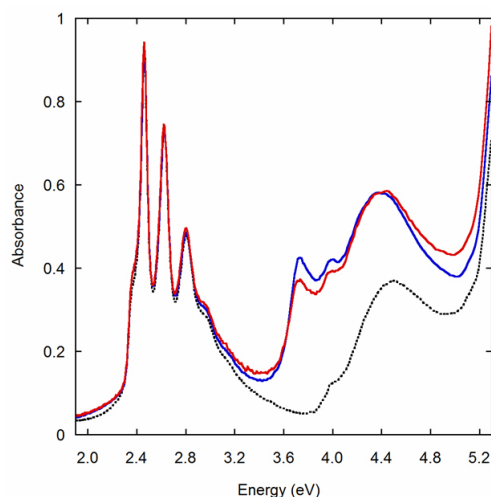
Figure 5.11: Absorption spectra of a bare tetracene (0 0 1) single crystal (black dotted line), of a rubrene film grown on a tetracene (0 0 1) single crystal (blue line) and of the same sample after one year of exposure to ambient conditions (red line).

reported in chapter 4, only diffraction peaks corresponding to the $(h\ 0\ 0)$ and $(0\ 0\ l)$ planes of rubrene and tetracene, respectively, should appear in the spectra. Indeed, in the 2ϑ range reported in figure 5.10, the $(2\ 0\ 0)$ and $(0\ 0\ 1)$ diffraction peaks of orthorhombic rubrene and tetracene, respectivly, are visible, but also a third peak, in-between those two, is present. The angular position of this peak corresponds to an interplanar spacing compatible with the height of a single crystalline layer of rubrene endoperoxide as determined by the AFM measurements reported in the previous sections. This is thus a strong confirmation of the actual formation of a native oxide layer on top of rubrene crystalline thin films upon their oxidation.

5.7.2   Absorption spectra evolution

Figure 5.11 shows the normal incidence optical absorption of a 10 nm thick rubrene thin film grown on a few hundred nanometers thick tetracene single crystal. The spectra have been collected with depolarized light immediately after the extraction from the deposition chamber (blue line) and after about one year of exposure to light and air in ambient conditions (red line). The optical response of the bare tetracene single crystal substrate is also reported for comparison (black dotted line).

The overall line-shape of the absorption spectrum of the bare tetracene single crystal is almost unchanged by the presence of rubrene till about

3.2 eV, either immediately after the exposure to ambient conditions or after one year. The known rubrene absorption peaks from about 2.3 to 3.0 eV are indeed superimposed to the tetracene ones (see e.g. Refs. [144] and [58]).

On the other hand, the contribution of the rubrene thin film can be clearly detected at higher energy, where tetracene crystals are almost transparent ($3.5 \div 4.0$ eV); here, a well-defined peak is indeed observed at about 3.7 eV and can be attributed to a rubrene absorption peak [58]. Above 4 eV, the spectral response of rubrene is once again overlapped to the tetracene one, and separating the contributions of the two materials is not straightforward.

One year exposure to ambient conditions led to a change in rubrene optical response just in the energy range above 3.5 eV. In particular, the intensity of the peak at about 3.7 eV decreased by about 15%, while absorption around 5 eV increased. This behavior can be easily ascribed to the photo-oxidation process, as described by the findings by Kykta *et al.* reported in Ref. [29], where a real-time observation of the optical response of an amorphous rubrene thin film undertaking oxidation is presented (see also figure 2.2b); the rubrene absorption peaks around 2.5 eV and 4 eV rapidly decrease in intensity during the oxidation process, whilst a new, broad spectral feature appears at about 5 eV, interpreted as the oxide spectral signature. A similar behaviour is also observed for other rubrenes, as described in Ref. [125].

5.8 Conclusions

The real-time observation of the oxidation dynamics of crystalline rubrene thin films carried out by a combination of different AFM-based imaging techniques has been reported and discussed in details. From the simultaneous observation of surface morphology and surface potential evolution of such films, it has been shown that the effect of oxidation of rubrene molecules is the formation of a crystalline layer of rubrene endoperoxide molecules covering the surface of the pristine films, somehow resembling the formation of the native oxide layer on silicon. This picture is also confirmed by X-ray diffraction measurements, demonstrating the presence, on top of rubrene crystalline thin films exposed to air for some time, of crystalline molecular layers with an interplanar spacing compatible with the height of a layer of rubrene endoperoxide molecules, and by the evolution of the absorption

spectra of rubrene crystalline thin films upon their exposition to ambient air, showing the characteristic signature of rubrene oxidation.

These results show that oxidation is a relevant phenomenon even for crystalline rubrene thin films, and thus its influence over their electrical transport properties can not be neglected. Thus, the next chapter will be devoted to the study of the influence of oxidation over the transport properties of crystalline rubrene.

Chapter 6

Influence of oxygen on electrical transport in crystalline rubrene

6.1   Introduction

As already shown in chapter 2, oxygen seems to strongly affect the transport properties of rubrene single crystals. However it is still unclear whether oxidation of rubrene has a detrimental or enhancing effect over rubrene single crystals conductivity and photoconductivity. Among of the main difficulties that need to be overcome in order to get a deeper knowledge about this topic there are the lack of control over the actual degree of oxidation of different samples and the uncertainty about the actual form in which oxygen is included in the crystals. In this chapter thus, the electrical transport and photocurrent generation properties of several crystals grown from different rubrene derivatives, with different stability toward oxidation, will be compared, in order to find a direct correlation between the transport properties of rubrene and its interactions with oxygen.

6.2   Substituted rubrenes

The substitution of two of the phenyl rings on opposite sides of a rubrene molecule with different electron withdrawing or donating groups is in general a way to affect the molecule stability toward oxidation[125, 145] without
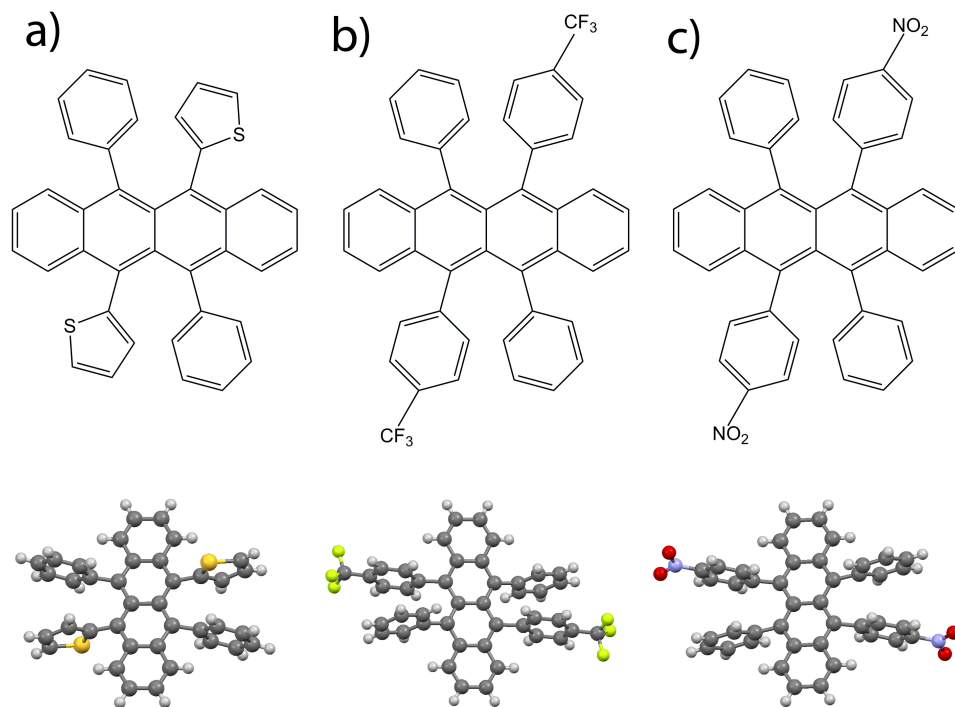
Figure 6.1: Structural formula (*top*) and molecular structure (*bottom*) of thiophene substituted rubrene (*a*), 4-trifluoromethyl substituted rubrene (*b*) and 4-nitrophenyl substituted rubrene (*c*).

significantly altering the electron density distribution around the tetracenic core of the molecule and the molecular packing in the solid and, therefore, also the transport properties of the material, which are directly connected to the interactions between the π systems of adjacent molecules (see chapter 2).

Several rubrene derivatives have been synthesized in the frame of a research project (Fondazione Cariplo, n. 2009/2551), and we focused on three of them, whose structural formulas and molecular structures are reported in figure 6.1: one molecule of rubrene with two thiophene groups substituted to two phenyl rings (Rub-Thio), 4-trifluoromethyl substituted rubrene (Rub-CF_3) and 4-nitrophenyl substituted rubrene (Rub-NO_2).

In principle, due to the different electron withdrawing or donating strength of the various groups substituted to the phenyl rings, the reactivity toward oxygen of these molecules should vary with respect to that of rubrene. One possible way to verify that this is indeed the case is to study the time evolu-
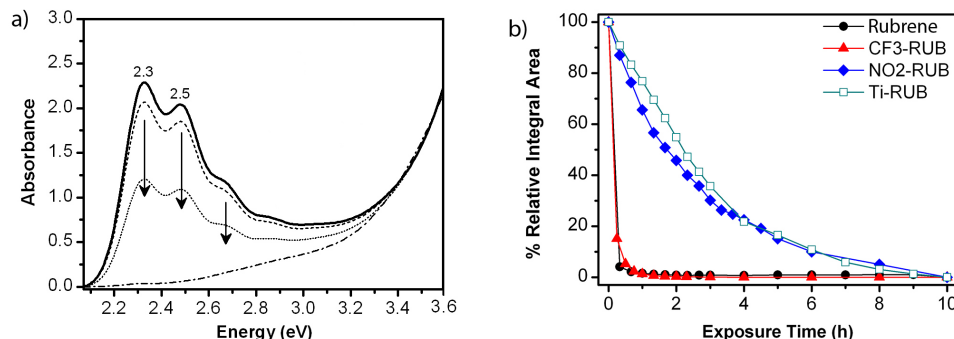
Figure 6.2: (*a*) Absorption spectra of a 2.2×10^{-4} M Rub-NO$_2$ solution taken just after preparation (*continuous line*), after 20 min (*dashed line*), after 2 h (*dotted line*) and after 6 h (*dashed-dotted line*) of exposition to ambient under light. (*b*) Relative area of the $(2.1 \div 2.8)$ eV region of the absorption spectra of rubrene, Rub-CF$_3$ and Rub-NO$_2$ as a function of exposure time to air and light.

tion of the absorption spectra of these molecules in solution, since, as shown in figure 2.2b, oxidation leaves a strong signature over the absorption spectra of rubrene, due to the disruption of the conjugation of the tetracene backbone of the molecule upon the formation of the endoperoxide and to the consequent disappearance of the corresponding absorption peaks.

In figure 6.2a the absorption spectra of a 2.2×10^{-4} M solution of Rub-NO$_2$ molecules taken right after the preparation of the solution and then after different times of exposure to ambient air and light are shown. An evolution with time of the absorption spectrum, with the progressive decrease of the absorption peaks below 3 eV, is clearly noticeable. This behavior is in line with that of the absorption spectrum of rubrene (reported in figure 2.2b) and thus clearly indicates the onset of oxidation. By comparing the time evolution of the absorption spectra of the different rubrene derivatives it is then possible to compare their stability toward oxidation. In order to carry out a quantitative comparison, the relative area of the $(2.1 \div 2.8)$ eV region of the absorption spectra as a function of exposure time to light and air has been measured; the results are shown in figure 6.2b, where the relative area of the $(2.1 \div 2.8)$ eV region of the absorption spectra of rubrene, Rub-NO$_2$, Rub-CF$_3$ and Rub-Thio solutions with the same concentration is reported as a function of time.

The results of these measurements clearly show that the different rubrene derivatives behave differently with respect to their stability toward oxidation. In particular Rub-CF$_3$ is slightly more stable than standard rubrene, with
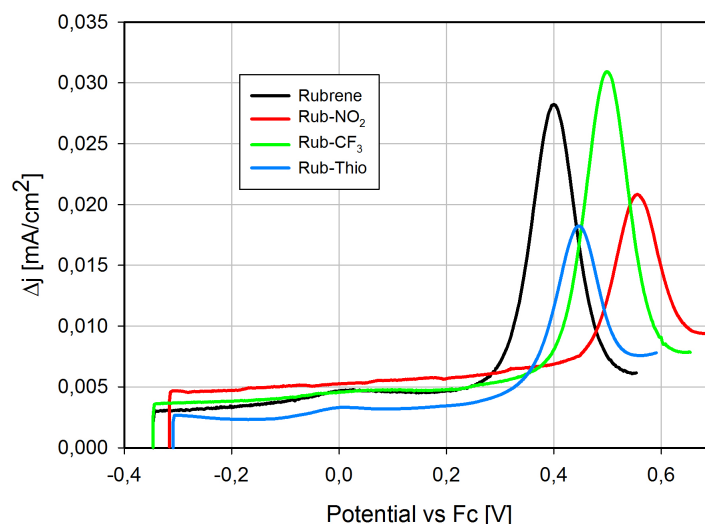
Figure 6.3: Results of cyclic voltammetry measurements carried out on rubrene, Rub-Thio, Rub-CF$_3$ and Rub-NO$_2$ solutions. On the horizontal axis is reported the oxidation potential relative to that of ferrocene.

a little longer time required for the absorption intensity to drop to 0. Rub-NO$_2$, on the other hand, is way more stable, and it takes $\approx$ 10 h to get completely oxidized; finally Rub-Thio appears to be as stable as Rub-NO$_2$, with a decay time of several hours.

In order to get more insights into the properties of the rubrene derivatives described so far, in particular with respect to their reactivity toward oxygen, cyclic voltammetry measurements in solution have been carried out for all the molecules, since this kind of measurements give information on the position of the HOMO levels of a molecule and thus on the reactivity toward oxygen. The results are reported in figure 6.3, and the HOMO values extracted from these measurements are summarized in table 6.1. These results clearly indicate that rubrene can indeed be oxidized more easily with respect to all the other derivatives. Also in the case of Rub-CF$_3$ and Rub-NO$_2$, the results of cyclic voltammetry are in agreement with the oxidation rates determined from the evolution of the optical absorption spectra shown in figure 6.2, with Rub-NO$_2$ having the largest oxidation potential and a correspondingly high stability toward oxidation. The interpretation of the results is not as straightforward in the case of Rub-Thio, since, to a stability toward oxidation equivalent to that of Rub-NO$_2$, correspond the lowest

Molecule	HOMO (eV)
Rubrene	-5.63
Rub-Thio	-5.71
Rub-CF$_3$	-5.73
Rub-NO$_2$	-5.78

Table 6.1: HOMO levels of rubrene and of its three derivatives in solution, as determined by cyclic voltammetry measurements.

oxidation potential among all the studied rubrene derivatives, whose value is the nearest to the rubrene one.

The results of the cyclic voltammetry and solution stability measurements for Rub-Thio are even more surprising considering that the thiophene groups are electron donors and thus, by purely chemical considerations, this molecule would be expected to be more easily oxidized and thus more reactive toward oxygen than rubrene itself. A possible explanation for this behavior, and also for the discrepancy between the results of the cyclic voltammetry measurements and the measurements of the absorption spectrum evolution for Rub-Thio, could lie in the contribution of conformational effects over molecular stability. Indeed, it is known that tetracene and rubrene molecules in solution can be twisted, with a consequent loss of molecular planarity[146]. This loss of planarity leads to a decrease in the aromatic stability of the molecule, which in turn leads to an increase of the molecule reactivity with oxygen. In the rubrene derivatives, the replacement of some of the phenyl groups with different groups could hinder molecular twisting, due to the interactions between the phenyl rings and the newly added functional groups. The lack of twisting in some of the rubrene derivatives (*e.g.* in the case of Rub-Thio) would make them more stable, due to the effects of the so-called aromatic stabilization, which is instead lost in the case of twisted molecules. This conformational effect could prevail on the effect of the electronic properties of the substituents, leading, in the case of Rub-Thio to a molecule which is more stable then all the other rubrene derivatives and has a larger oxidation potential then rubrene, even if an electron donating group has been added. In order to test this hypothesis molecular dynamics calculations of the isolated molecule conformations of all the rubrene derivatives are needed.

Anyway, we now have a set of rubrene-like molecules with different intrin-
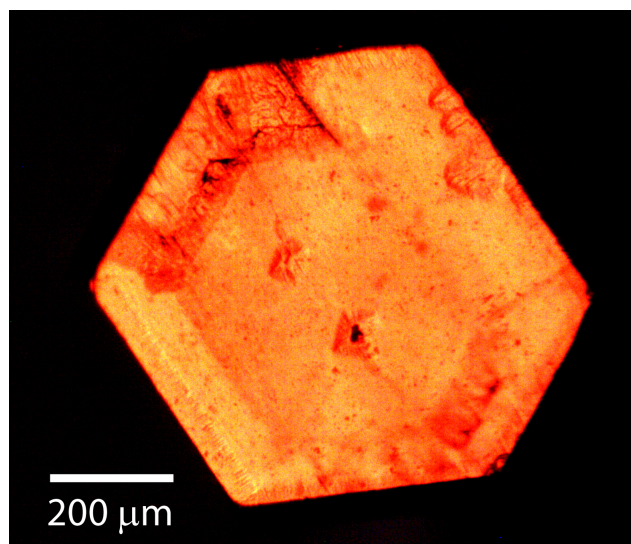
Figure 6.4: Optical microscope image of a rubrene single crystal grown by sublimation in vacuum and observed under polarized light.

sic stability toward oxidation that can be used to probe the dependance of rubrene transport properties on oxidation. In order to do so it has been first necessary to grow single crystals from the whole series of rubrene derivatives and to check their structure.

6.2.1   Crystal structure of rubrene derivatives

The growth and characterization of single crystals of the three rubrene derivatives presented before and of commercial rubrene powder have been carried out in the frame of the same research project (Fondazione Cariplo, n. 2009/2551).

Single crystals have been grown by vacuum sublimation or slow solvent evaporation methods. By these means it has been possible to obtain several crystals with lateral sizes of the order of hundreds of µm and with a thickness of tens of µm. All crystals, grown from different starting materials, have the same appearance at a first visual inspection, exemplified by the optical microscope image reported in figure 6.4 and referring to one of the vacuum grown rubrene single crystals.

The crystal structure of the crystals grown from all the rubrene derivatives has been determined by single crystal X-ray diffraction measurements. All the measurements have been carried out at a temperature of 120 K with

	Rub-Thio	Rub-CF$_3$	Rub-NO$_2$
Symmetry	Monoclinic	Monoclinic	Monoclinic
Space group	P2$_1$/c	P2$_1$/c	P2$_1$/c
a [Å]	13.5679(5)	15.9903(6)	15.0992(4)
b [Å]	7.0143(2)	7.2750(2)	7.1710(2)
c [Å]	14.3020(7)	13.9890(7)	14.2503(5)
β [°]	103.954(2)	102.856(2)	100.638(2)
Z	2	2	2
h [Å]	3.531	3.520	3.584

Table 6.2: Crystal structure parameters of single crystals grown from Rub-Thio, Rub-CF$_3$ and Rub-NO$_2$. h is the intermolecular distance along the direction indicated in figure 6.5b. All these values refer to measurements carried out at 120 K.

a Rigaku RAPID II single crystal X-ray diffractometer. The results of the structure determination are reported in table 6.2.

It can be noticed that all the crystals present a monoclinic structure and very similar unit cell parameters. What is particularly remarkable, however, is the fact that the molecular packing in the (1 0 0) plane is the same for all the crystals and, even more remarkably, the same observed for rubrene molecules in the (1 0 0) plane of its orthorhombic phase; this can be cleary seen in figures 6.5a, b, c and d, where the molecular arrangements in rubrene, Rub-Thio, Rub-NO$_2$ and Rub-CF$_3$ crystals are reported, respectively, as they appear if observed through the **a*** reciprocal lattice direction. As already clear at a visual inspection, it is also confirmed by measurements: even the intermolecular distances are close to each other for all the structures (see last row of table 6.2; intermolecular distance in orthorhombic rubrene is 3.721 Å). As shown in chapter 2 this is the plane where the direction of maximum mobility for rubrene single crystals is measured, namely the [0 1 0] lattice direction.

A final notable element is the fact that even the vertical alignment between adjacent molecules is perfect for all the crystalline structures, leading to the same ideal condition for charge transport found in the case of rubrene crystals.

All these similarities between the molecular packing in all the crystals are particularly welcome, since they permit to carry out transport measurements on all the samples with the same geometry, and to directly compare the results obtained from different crystals, in view of focusing on the oxidation
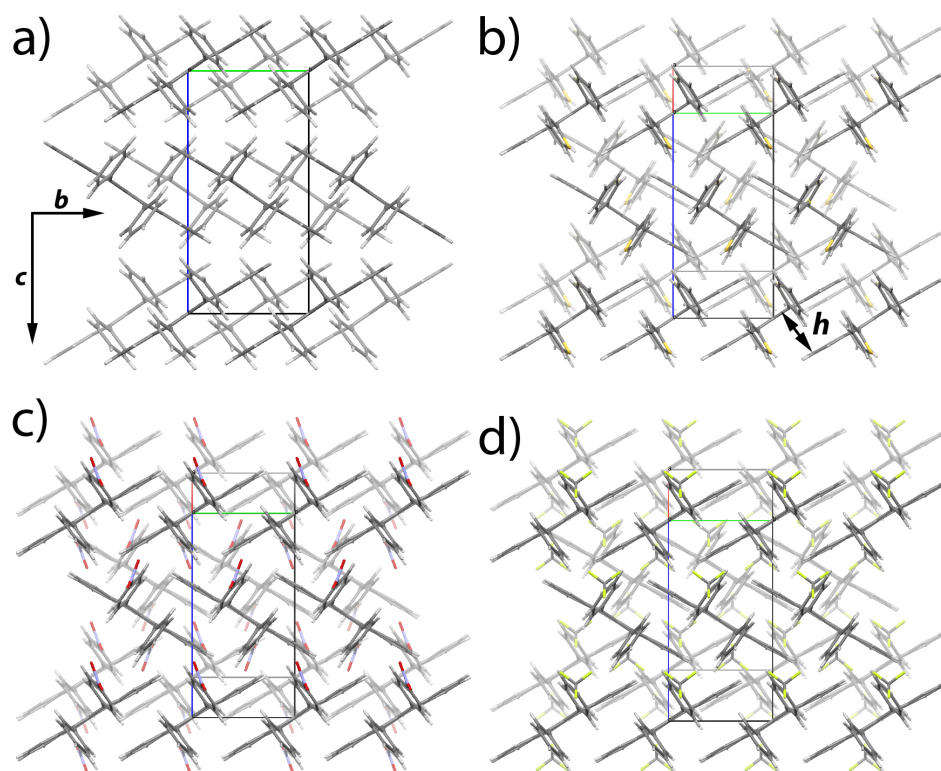
Figure 6.5: Molecular arrangement in the orthorhombic crystalline phase of rubrene
(a) and in the monoclinic crystalline phase of Rub-Thio (b), Rub-NO$_2$ (c) and Rub-
CF$_3$, as observed through the $\mathbf{a^*}$ reciprocal lattice direction. The direction of the
$\mathbf{b}$ and $\mathbf{c}$ lattice directions is reported in (a) and is the same for all the images. The
arrow labeled with h in (b) indicates the direction along which the intermolecular
distances reported in table 6.2 have been measured.
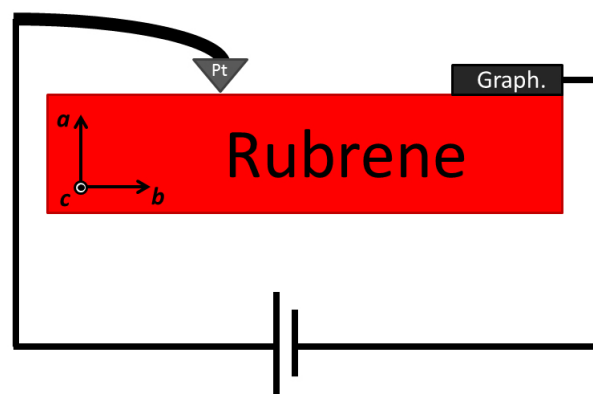
Figure 6.6: Scheme of the experimental setup used for the C-AFM measurements carried out on all the rubrene derivatives single crystals. The orientation of the crystalline axes is also indicated, with the **a** axis vertically oriented, the **b** axis horizontally oriented and the **c** axis pointing out of the page.

influence.

6.3 Dark current measurements

The transport properties in a dark environment of all the crystals described in the previous section have been probed by conductive AFM (C-AFM, see chapter 3 for a full description of this technique). In order to probe the transport properties along the **b** lattice direction of the crystals, which corresponds both to the direction of maximum mobility for rubrene and to the direction in which the molecular packing is the same for all the crystals, we used the experimental set-up sketched in figure 6.6.

The tip used for these measurements is entirely made of platinum (Rocky Mountain Nanotechnology) with a force constant of $0.3\,\mathrm{N\,m^{-1}}$, a resonance frequency of $5\,\mathrm{kHz}$ and a tip curvature radius below $20\,\mathrm{nm}$. The use of this kind of tip, with respect to standard silicon nitride tips with metallic coatings, permits to obtain more reproducible results, since there are not any issues related to coating damage due to current induced heating or scratching of the tip. The other electrode has been fabricated by depositing colloidal graphite paint (Agar Scientific) next to one of the two edges at the opposite sides of the **b** lattice direction of the crystals and letting it dry for one day (see the sketch reported in figure 6.6). This operation have been carried out under an optical microscope, in order to be sure that the contact area was
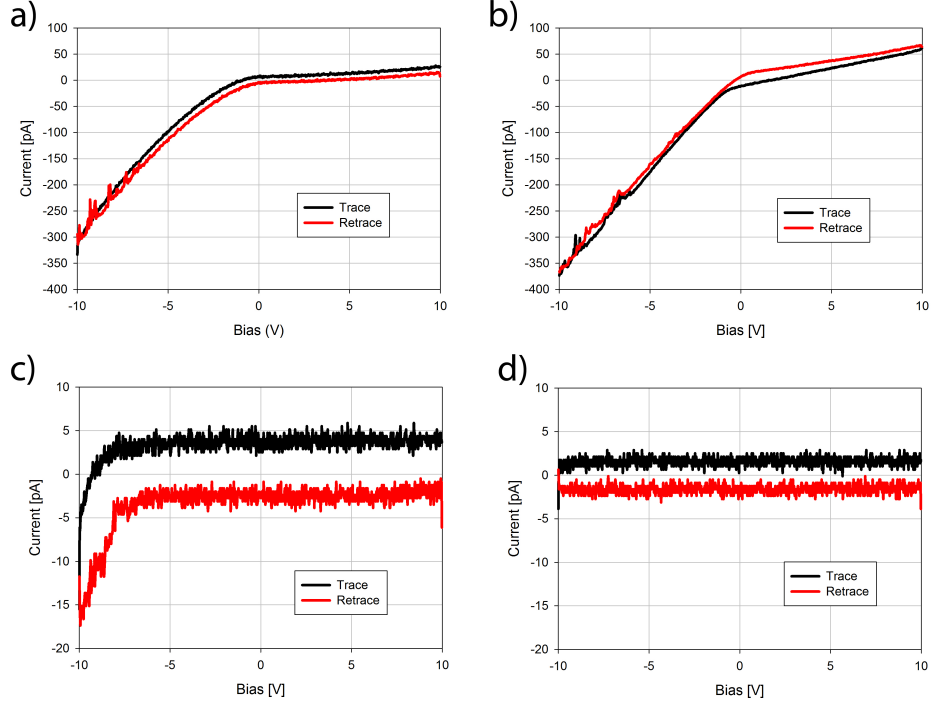
Figure 6.7: C-AFM I-V curves collected from rubrene (a), Rub-Thio (b), Rub-CF$_3$ (c) and Rub-NO$_2$ (d) single crystals for current flowing in the **b** lattice direction. In each plot are reported the trace (*black*) and retrace (*red*) curves, corresponding to -10 V -> 10 V and 10 V -> -10 V bias sweeping, respectively.

the same for all the samples. Colloidal graphite has been chosen in spite of other contacting materials, such as silver paint, since it provides particularly low contact resistance with rubrene[147].

C-AFM has been used to collect I-V curves in the $(-10 \div 10)$ V range (the maximum bias range allowed by the instrument) from all the four crystals. The tip have been placed at a distance of ≈ 100 µm from the graphite electrode along the **b** lattice direction and the tip load was 50 nN for all the measurements (in order to have the same tip contact area for all the samples). The I-V curves have been collected sweeping the voltage between -10 V and 10 V (trace) and then sweeping it back (retrace), with a repetition rate of 0.5 Hz and measuring the current at each ≈ 0.02 V step. The results are reported in figure 6.7.

A general feature of all the curves (except for that collected from Rub-NO$_2$, shown in figure 6.7d) is their asymmetry between the negative and positive bias regions. This is due to the fact that rubrene is an unipolar

material, with an hole mobility much higher than electron mobility, combined with the asymmetry between the two electrodes, with graphite having a much lower contact resistance with respect to platinum. Thus, transport of holes toward the graphite contact is favored over transport toward the tip. Apart from this, a clear trend in the measured current can be observed: on the Rub-NO$_2$ crystal no current at all can be measured in the whole bias range, in the case of Rub-CF$_3$ a current of the order of $10\,\mathrm{pA}$ is measured, while rubrene and Rub-Thio both show similar I-V curves, with a maximum current, reached at $-10\,\mathrm{V}$, around $300\,\mathrm{pA}$.

This trend shows a correlation with the results of cyclic voltammetry measurements reported in table 6.1, showing that the molecules with the lower oxidation potential are also the ones with better transport properties. In particular Rub-NO$_2$, which has the larger oxidation potential among the rubrene derivatives, shows no current at all, while Rub-Thio, whose oxidation potential is the nearest to that of rubrene, shows current values comparable to those of rubrene itself. This, in combination with the fact that the molecular packing, and thus the interaction between the π systems of adjacent molecules, is the same for all the samples, proves that the interaction with oxygen plays an essential role with respect to electrical transport in rubrene single crystals, in accordance with the results reported in Ref. [31] (see also figure 2.11b). With respect to the measurements of the absorption spectra evolution (figure 6.2b) no clear correlation can instead be found. This can be explained if the enhancing effect over rubrene transport properties is due to the interaction of molecules with interstitial molecular oxygen and not to the formation of endoperoxide, which is the process probed by the measurements of the absorption spectra evolution. A role of interstitial oxygen in enhancing rubrene photoconductivity is suggested in Ref. [71] and is discussed in more detail in the next section; a similar process could play a role in the case of dark conductivity, but further experiments are needed to clarify this aspect.

6.4   Photoconductivity measurements

As already discussed in chapter 2, oxidation of rubrene seems to play a key role also in enhancing the photocurrent generation efficiency of rubrene single crystals, by increasing the dissociation rate of excitons into couples
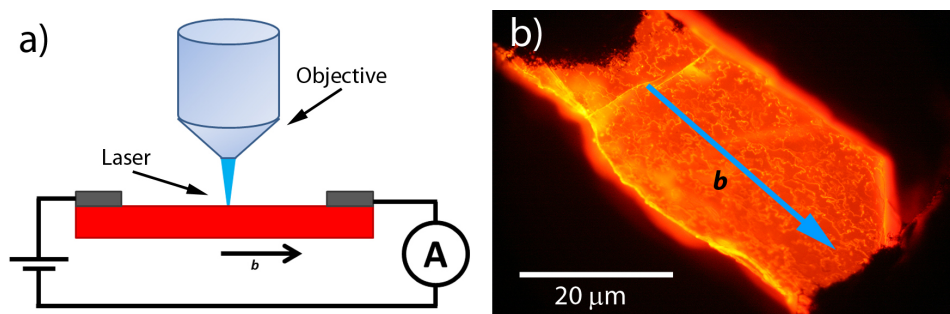
Figure 6.8: (*a*) Experimental set-up used for the photoconductivity measurements. On the two ends of the sample, along the **b** lattice direction, are deposited two electrodes, used both to apply the bias and to measure the current. The excitation light comes from a laser beam focused by a microscope objective in-between the two electrodes. (*b*) Photograph of one of the crystals used for the photoconductivity measurements, taken with a confocal microscope. The two graphite contacts deposited over the crystal are visible at the two ends of the crystal. The **b** lattice direction is indicated by the blue arrow.

of free charge carriers. In order to confirm this picture, which is up to now only based over the collection of various pieces of evidence, the photocurrent generation efficiency of single crystals grown from the various rubrene derivatives presented above has been measured.

The experimental set-up used for this experiment is sketched in figure 6.8a. A series of rubrene, Rub-CF$_3$ and Rub-NO$_2$ single crystals with similar dimensions has been selected; Rub-Thio crystals could not be used to carry out these measurements, since there wasn't enough starting material for the growth of more crystals. Nonetheless, the synthesis of new starting material is ongoing, and the measurements will be soon integrated. Colloidal graphite paint was used to deposit two contacts at the two ends along the **b** lattice direction of each crystal (see the photo reported in figure 6.8b). The current passing through the crystals has been measured with a Keithley 2400 SourceMeter, used also to apply the desired bias between the two electrodes. The light source used for photocurrent generation was a laser at a wavelength of 473 nm, with an incident intensity of 15 mW. The laser beam, focused thanks to a confocal microscope, had a spot size of $\approx 2\,\mu m^2$ and have been carefully positioned in-between the two electrodes. The use of a laser spot of such a small size and the high control over its position ensure that the experimental conditions used for the different measurements are always the same, in particular with respect to the total amount of photons absorbed by
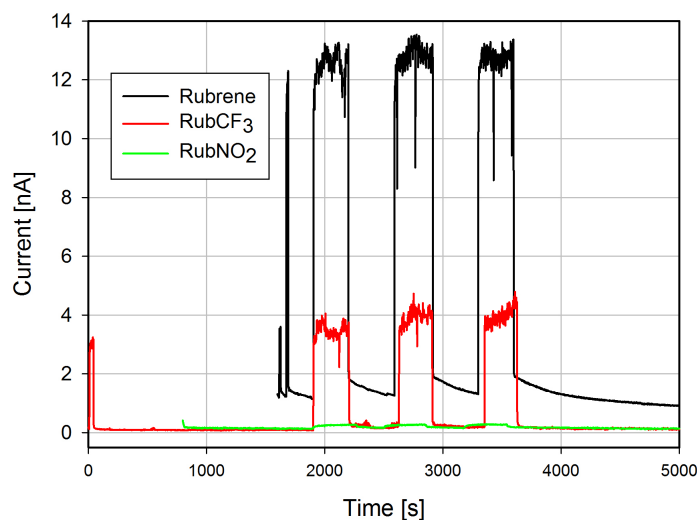
Figure 6.9: Current values measured from rubrene, Rub-CF$_3$ and Rub-NO$_2$ single crystals repeatedly switching the excitation light on and off. All the measurements have been carried out with the experimental set-up shown in figure 6.8a and with an 80 V bias.

each crystal. The channel between the two electrodes was $\approx 40\,\mu$m for all the samples.

The measurements were carried out by applying to each sample an 80 V bias and measuring the current passing between the electrodes both in the dark and during illumination, and led to the results shown in figure 6.9, where the current measured while switching the excitation light on and off several times is reported. In the case of rubrene, as expected, there is a huge increase in the measured current upon the exposition to light, with a photocurrent of ≈ 13 nA. Also Rub-CF$_3$ shows a large current increase after the excitation light is turned on, with a photocurrent of almost 4 nA. On the other hand, the Rub-NO$_2$ crystal shows no appreciable photocurrent generation, with only a little increase in the measured current (a fraction of a nA), below the noise margin of our measurements. These data are summarized in table 6.3.

These data, if compared with those reported in section 6.3 for the dark current measurements and with the stability and cyclic voltammetry data for the two rubrene derivatives, are in perfect agreement with the idea that the interaction of rubrene with oxygen has a positive effect over photocurrent generation efficiency. In particular the Rub-CF$_3$ crystal shows once again an

Sample	Photocurrent [nA]
Rubrene	11.6 ± 0.4
Rub-CF$_3$	3.8 ± 0.2
Rub-NO$_2$	0.12 ± 0.01

Table 6.3: Photocurrent values measured for rubrene, Rub-CF$_3$ and Rub-NO$_2$ single crystals.

intermediate behavior between that of rubrene and that of Rub-NO$_2$, which is way more stable than the other two.

A possible mechanism behind the oxygen related enhancement of rubrene photoconductivity has already been proposed by Maliakal *et al.* [71]. According to the authors, there is an electron transfer between the excited state of rubrene molecules and adjacent oxygen molecules. This charge transfer process leads to the formation of a couple of free charge carriers that can then be separated by the application of an electric field. In order to confirm this picture the authors carried out electron paramagnetic resonance (EPR) measurements, which indicated the presence in the rubrene crystals of rubrene radical cation and superoxide radical anion pairs during the irradiation of the samples in an oxygen atmosphere.

Our measurements strongly support this picture, showing that the photoconductivity of rubrene is highly related to its reactivity toward oxygen and to its oxidation potential.

6.5   Conclusions

In this chapter the influence of oxidation over the transport properties of rubrene single crystals has been studied by the comparison of dark conduction and photoconduction measurements carried out on a series of rubrene derivatives with different stability toward oxidation but with the same molecular packing of rubrene in their crystalline phase. The results show that the rubrene derivatives with larger reactivity toward oxygen also have better transport and photocurrent generation properties. This result, indicating the importance of oxygen for electrical transport and photocarrier generation in rubrene, also suggests a possible route for the improvement of rubrene based devices. In particular, the careful tailoring of rubrene derivatives with the right substituents could lead to new materials with even better trans-

port properties than rubrene itself. Before these results can be pursued it will be necessary to get more insights into the properties of the various rubrene derivatives. In particular, the reasons behind the peculiar behavior of Rub-Thio, with the lack of agreement between the results of the cyclic voltammetry and absorption spectrum evolution measurements, have to be understood. With this respect, molecular dynamics simulations of the ground state conformation of all the rubrene derivatives are needed in order to understand the role of conformational stability in determining their overall stability toward oxidation.

For a full understanding of this topic, carrying out photoconductivity measurements over Rub-Thio is also needed, in order to confirm the expected trend, as well as to compare our results with theoretical calculations of the electrostatic and transport properties of the various rubrene derivatives crystal structures. It is also necessary to fabricate working devices based on the crystals grown from the various rubrene derivatives, in order to quantitatively determine their charge carrier transport parameters, such as their mobility, permitting then a quantitative comparison with the transport properties of other materials and a better understanding of the relationship between the oxidation potentials of rubrene derivatives and their transport properties. Moreover, the possibility of growing crystalline thin films starting from rubrene derivatives showing potentially better transport properties than rubrene itself, like Rub-Thio or newly synthesized derivatives, needs to be explored, in order to be able to fabricate working thin film devices starting from those materials.

Conclusions and Perspectives

The focus of the present thesis is on rubrene, a very promising molecule in the field of organic electronics due to its outstanding charge transport properties and photoconductivity.

On one hand, the properties of pure rubrene, grown as crystalline thin films by OMBE, have been studied. Rubrene thin films have been grown over two different substrates: tetracene single crystals and α-4T thin films previously grown on the surface of KAP single crystals. It has been shown that in both cases highly ordered films, with the molecules packed according to the rubrene orthorhombic crystalline phase can be obtained. In particular, in the case of tetracene substrates, the use of grazing incidence X-ray diffraction techniques allowed us to demonstrate that the rubrene thin films had a unique in-plane orientation, as determined by the epitaxial relationship: rubrene[0 2 1]//tetracene[1 $\bar{1}$ 0]. This result is of particular importance, since it opens up the possibility to build all-organic electronic devices based on rubrene crystalline thin films with a unique and controlled in-plane orientations, making it possible for these devices to reach efficiencies near to those of single crystal based devices.

In the second case instead, a multiplicity of in-plane orientations of the rubrene crystalline film have been observed by a combination of AFM and optical absorption measurements. Moreover, by comparison with the results of numerical calculations, it has been possible to demonstrate that all the observed in-plane orientations correspond to the same epitaxial relationship, namely rubrene<0 2 1>//α-4T<1 1 0>, which gives rise to multiple in-plane orientations due to symmetry reasons. All-organic multilayer heterostructures are of particular interest with respect to their possible use in the fabrication of organic cascade solar cells, in which multiple layers of different materials with complementary light absorption regions are exploited in order to enhance spectral coverage and thus power conversion efficiency.

Once the possibility to grow crystalline and well oriented rubrene thin films has been assessed, the effects of oxidation over such films have been studied. In order to do so the evolution of the morphological and electrostatic properties of rubrene thin films grown on tetracene single crystals have been monitored by a combination of several AFM based techniques. As a result it has been shown that the exposure of the films to ambient air leads to the formation of a crystalline, native layer of rubrene endoperoxide molecules on top of the pristine rubrene film, somehow in analogy with the formation of the native oxide layer on silicon. This result demonstrate that upon oxidation rubrene molecules retain a crystalline order and that oxidation also affects crystalline rubrene.

After some conclusive results on crystalline rubrene have been reached, in particular with respect to the effects of oxidation over its structural and electrostatic properties, we moved to the study of the relationship between the transport properties of crystalline rubrene and its oxidation, a topic which is still subject to strong debate. In order to do so several rubrene derivatives, with different stability toward oxidation have been synthesized. From all those derivatives single crystals have been grown, all showing the same molecular packing of rubrene crystals, and their transport properties have been probed by C-AFM. The results showed strong variations between the transport properties of the different derivatives, and a clear link between interaction with oxygen and transport properties seems to exists, with the latter being worse when oxidation potential is increased.

The photoconductivity of the crystals grown from the same rubrene derivatives has also been probed, showing how also in this case a clear link between reactivity to oxygen and crystal photoconductivity exists, as already suggested in the literature.

In conclusion, the overall research work discussed in this thesis opens some interesting and promising perspectives.

First, the possibility to use rubrene crystalline thin films for the fabrication of organic field-effect transistors or photovoltaic cells, exploiting the possibility to induce specific in-plane orientations of the film by selecting the proper substrate. In this respect, the study of the optical and electrical transport properties of crystalline rubrene endoperoxide is being pursued, in order to be able to exploit the native rubrene endoperoxide layer forming over rubrene crystalline thin films for the fabrication of electronic devices.

Second, the study of the role of oxygen in enhancing rubrene transport properties, other than suggesting an essential role being played by oxygen in electrical transport in crystalline rubrene, indicates a possible route for tailoring the transport properties of crystalline rubrene by substituting the peripheral phenyl rings with proper functional groups, in order to affect its reactivity toward oxygen without affecting the molecular packing in the crystalline phase. A study of how specific substituents affect rubrene stability toward oxidation is therefore of particular importance, since our results showed that the relationship between rubrene endoperoxide formation and the electronic properties of specific substituents is not straightforward, suggesting a role of the substituents in affecting the conformational stability of the molecule. More in details, some work is to be devoted to widen the study of Rub-Thio, which seems to show transport properties comparable to those of rubrene while being highly stable with respect to endoperoxide formation. The growth of crystalline thin films of different rubrene derivatives is also to be addressed in the near future, in order to be able to compare their properties with those of rubrene thin films, in view of their possible use in electronic devices.

Bibliography

[1] A. Tsumura, H. Koezuka, and T. Ando, *Macromolecular electronic device: Field-effect transistor with a polythiophene thin film*, Applied Physics Letters **49** (1986), no. 18, 1210–1212.

[2] G. Horowitz, D. Fichou, X. Peng, Z. Xu, and F. Garnier, *A field-effect transistor based on conjugated alpha-sexithienyl*, Solid State Communications **72** (1989), no. 4, 381–384.

[3] F. Garnier, G. Horowitz, X. Peng, and D. Fichou, *An all-organic "soft" thin film transistor with very high carrier mobility*, Advanced Materials **2** (1990), no. 12, 592–594.

[4] J. H. Burroughes, D. D. C. Bradley, A. R. Brown, R. N. Marks, K. Mackay, R. H. Friend, P. L. Burns, and A. B. Holmes, *Light-emitting diodes based on conjugated polymers*, Nature **347** (1990), no. 6293, 539–541.

[5] S. Chen, L. Deng, J. Xie, L. Peng, L. Xie, Q. Fan, and W. Huang, *Recent developments in top-emitting organic light-emitting diodes*, Advanced Materials **22** (2010), no. 46, 5227–5239.

[6] N. T. Kalyani and S. J. Dhoble, *Organic light emitting diodes: Energy saving lighting technology - a review*, Renewable and Sustainable Energy Reviews **16** (2012), no. 5, 2696–2723.

[7] C. W. Tang and S. A. VanSlyke, *Organic electroluminescent diodes*, Applied Physics Letters **51** (1987), no. 12, 913–915.

[8] C. W. Tang, *Two-layer organic photovoltaic cell*, Applied Physics Letters **48** (1986), no. 2, 183–185.

[9] C. Deibel and V. Dyakonov, *Polymer-fullerene bulk heterojunction solar cells*, Reports on Progress in Physics **73** (2010), no. 9, 096401.

[10] A. Mishra and P. B´auerle, *Small molecule organic semiconductors on the move: Promises for future solar energy technology*, Angewandte Chemie International Edition **51** (2012), no. 9, 2020–2067.

[11] C. Wöll, *Physical and chemical aspects of organic electronics*, Wiley-VCH Verlag GmbH & Co. KGaA, 2009.

[12] S. Chènais and S. Forget, *Recent advances in solid-state organic lasers*, Polymer International **61** (2012), no. 3, 390–406.

[13] D. A. Bernards, R. M. Owens, and G. G. Malliaras, *Organic semiconductors in sensor applications*, Springer Series in Materials Science, v. 107, Springer London, Limited, 2008.

[14] V. Podzorov, E. Menard, A. Borissov, V. Kiryukhin, J. A. Rogers, and M. E. Gershenson, *Intrinsic charge transport on the surface of organic semiconductors*, Physical Review Letters **93** (2004), no. 8, 086602.

[15] M. Yamagishi, J. Takeya, Y. Tominari, Y. Nakazawa, T. Kuroda, S. Ikehata, M. Uno, T. Nishikawa, and T. Kawase, *High-mobility double-gate organic single-crystal transistors with organic crystal gate insulators*, Applied Physics Letters **90** (2007), no. 18, 182117.

[16] H. Najafov, B. Lyu, I. Biaggio, and V. Podzorov, *Investigating the origin of the high photoconductivity of rubrene single crystals*, Phys. Rev. B **77** (2008), 125202.

[17] H. Najafov, B. Lee, Q. Zhou, L. C. Feldman, and V. Podzorov, *Observation of long-range exciton diffusion in highly ordered organic semiconductors*, Nat Mater **9** (2010), no. 11, 938–943.

[18] V. Podzorov, S. E. Sysoev, E. Loginova, V. M. Pudalov, and M. E. Gershenson, *Single-crystal organic field effect transistors with the hole mobility $\approx 8\ cm^2/Vs$*, Applied Physics Letters **83** (2003), no. 17, 3504–3506.

[19] D. Käfer and G. Witte, *Growth of crystalline rubrene films with enhanced stability*, Physical Chemistry Chemical Physics **7** (2005), no. 15, 2850.

[20] H. Zaglmayr, L.D. Sun, G. Weidlinger, Sh.M. A. Al-Baqi, H. Sitter, and P. Zeppenfeld, *Initial stage of crystalline rubrene thin film growth on mica (0 0 1)*, Synthetic Metals **161** (2011), no. 3-4, 271–274.

[21] Se-Woong Park, Jeong-Min Choi, K. H. Lee, H. W. Yeom, S. Im, and Y. K. Lee, *Amorphous-to-Crystalline phase transformation of thin film rubrene*, The Journal of Physical Chemistry B **114** (2010), no. 17, 5661–5665.

[22] S. Seo, B.-N. Park, and P. G. Evans, *Ambipolar rubrene thin film transistors*, Applied Physics Letters **88** (2006), no. 23, 232114.

[23] S. Sinha, C.-H. Wang, A. K. M. Maidul Islam, Y.-W. Yang, and M. Mukherjee, *Improvement of rubrene thin film transistor with self assembled monolayer of octadecyltrichlorosilane (OTS)*, AIP Conference Proceedings **1447** (2012), no. 1, 977–978.

[24] Y. Su, J. Liu, L. Zheng, Z. Ding, and Y. Han, *Polymer assisted solution-processing of rubrene spherulites via solvent vapor annealing*, RSC Adv. **2** (2012), 5779–5788.

[25] W. S Hu, S. Z Weng, Y. T Tao, H. J Liu, and H. Y Lee, *Oriented growth of rubrene thin films on aligned pentacene buffer layer and its anisotropic thin-film transistor characteristics*, Organic Electronics **9** (2008), no. 3, 385–395.

[26] H. M. Lee, H. Moon, H.-S. Kim, Y. N. Kim, S.-M. Choi, S. Yoo, and S. O. Cho, *Abrupt heating-induced high-quality crystalline rubrene thin films for organic thin-film transistors*, Organic Electronics **12** (2011), no. 8, 1446 –1453.

[27] M. Lan, Zu-Hong Xiong, Guo-Qing Li, Ting-Na Shao, Jia-Le Xie, Xiu-Fan Yang, Jun-Zhong Wang, and Y. Liu, *Strain-driven formation of rubrene crystalline films on bi(001)*, Physical Review B **83** (2011), no. 19, 195322.

[28] D. Liu, Z. Li, Z. He, J. Xu, and Q. Miao, *Induced crystallization of rubrene with diazapentacene as the template*, J. Mater. Chem. **22** (2012), 4396–4400.

[29] M. Kytka, A. Gerlach, F. Schreiber, and J. Kováč, *Real-time observation of oxidation and photo-oxidation of rubrene thin films by spectroscopic ellipsometry*, Applied Physics Letters **90** (2007), no. 13, 131911.

[30] C. Krellner, S. Haas, C. Goldmann, K. P. Pernstich, D. J. Gundlach, and B. Batlogg, *Density of bulk trap states in organic semiconductor crystals: Discrete levels induced by oxygen in rubrene*, Physical Review B **75** (2007), no. 24, 245115.

[31] K. K. Zhang, K. Tan, C. Zou, M. Wikberg, L. E. McNeil, S. G. Mhaisalkar, and C. Kloc, *Control of charge mobility in single-crystal rubrene through surface chemistry*, Organic Electronics **11** (2010), no. 12, 1928–1934.

[32] H. Najafov, D. Mastrogiovanni, E. Garfunkel, L. C. Feldman, and V. Podzorov, *Photon-Assisted oxygen diffusion and Oxygen-Related traps in organic semiconductors*, Advanced Materials **23** (2011), no. 8, 981–985.

[33] Y. Nakayama, S. Machida, T. Minari, K. Tsukagishi, Y. Noguchi, and H. Ishii, *Direct observation of the electronic states of single crystalline rubrene under ambient condition by photoelectron yield spectroscopy*, Applied Physics Letters **93** (2008), no. 17, 173305.

[34] L. Tsetseris and S.T. Pantelides, *Modification of the electronic properties of rubrene crystals by water and oxygen-related species*, Organic Electronics **10** (2009), no. 2, 333–340.

[35] X. Song, L. Wang, Q. Fan, Y. Wu, H. Wang, C. Liu, N. Liu, J. Zhu, D. Qi, X. Gao, and A. T. S. Wee, *Role of oxygen incorporation in electronic properties of rubrene films*, Applied Physics Letters **97** (2010), no. 3, 032106.

[36] M. Schwoerer and H. C. Wolf, *Organic molecular solids*, Wiley-VCH Verlag GmbH, 2008.

[37] T. Siegrist, C. Kloc, R. A Laudise, H. E Katz, and R. C Haddon, *Crystal growth, structure, and electronic band structure of α-4T polymorphs*, Advanced Materials **10** (1998), no. 5, 379–382.

[38] T. Siegrist, R. M. Fleming, R. C. Haddon, R. A. Laudise, A. J. Lovinger, H. E. Katz, P. Bridenbaugh, and D. D. Davis, *The crystal structure of the high-temperature polymorph of α-hexathienyl (α-6T/HT)*, Journal of Materials Research **10** (1995), no. 9, 2170–2173.

[39] A. S. Davydov, *Theory of molecular excitons*, McGraw-Hill series in advanced chemistry, McGraw-Hill, 1962.

[40] A. Sassella, M. Campione, and A. Borghesi, *Organic epitaxy*, Rivista del Nuovo Cimento **31** (2008), no. 8, 457 –490.

[41] V. Coropceanu, J. Cornil, D. A. da Silva Filho, Y. Olivier, R. Silbey, and J.-L. Brèdas, *Charge transport in organic semiconductors*, Chemical Reviews **107** (2007), no. 4, 926–952.

[42] D. A da Silva Filho, E. G Kim, and J. L Brèdas, *Transport properties in the rubrene crystal: electronic coupling and vibrational reorganization energy*, Advanced Materials **17** (2005), no. 8, 1072–1076.

[43] R. M. Hochstrasser and M. Ritchie, *The photoformation and thermal decomposition of rubrene peroxide*, Transactions of the Faraday Society **52** (1956), 1363.

[44] T. Takahashi, Y. Harada, N. Sato, K. Seki, H. Inokuchi, and S. Fujisawa, *Gas and solid phase photoelectron spectra of 5,6,11,12-tetra-phenylnaphthacene (rubrene)*, Bulletin of the Chemical Society of Japan **52** (1979), no. 2, 380–382.

[45] S. Erkoç, *Structural and electronic properties of rubreneperoxides*, Journal of Molecular Structure: THEOCHEM **578** (2002), no. 1-3, 99–101.

[46] O. D Jurchescu, A. Meetsma, and T. Palstra, *Low-temperature structure of rubrene single crystals grown by vapor transport*, Acta Crystallographica Section B **62** (2006), no. 2, 330–334.

[47] L. Huang, Q. Liao, Q. Shi, H. Fu, J. Ma, and J. Yao, *Rubrene micro-crystals from solution routes: their crystallography, morphology and optical properties*, Journal of Materials Chemistry **20** (2010), 159–166.

[48] T. Matsukawa, M. Yoshimura, M. Uchiyama, M. Yamagishi, A. Nakao, Y. Takahashi, J. Takeya, Y. Kitaoka, Y. Mori, and T. Sasaki, *Polymorphs of rubrene crystal grown from solution*, Japanese Journal of Applied Physics **49** (2010), no. 8, 085502.

[49] C. Reese and Z. Bao, *High-resolution measurement of the anisotropy of charge transport in single crystals*, Advanced Materials **19** (2007), no. 24, 4535–4538.

[50] S. Z. Bisri, T. Takenobu, T. Takahashi, and Y. Iwasa, *Electron transport in rubrene single-crystal transistors*, Applied Physics Letters **96** (2010), no. 18, 183304.

[51] A. Troisi, *Prediction of the absolute charge mobility of molecular semiconductors: the case of rubrene*, Advanced Materials **19** (2007), no. 15, 2000–2004.

[52] Z. Rang, M. I. Nathan, P. P. Ruden, V. Podzorov, M. E. Gershenson, C. R. Newman, and C. D. Frisbie, *Hydrostatic pressure dependence of charge carrier transport in single-crystal rubrene devices*, Applied Physics Letters **86** (2005), no. 12, 123501.

[53] J. Takeya, J. Kato, K. Hara, M. Yamagishi, R. Hirahara, K. Yamada, Y. Nakazawa, S. Ikehata, K. Tsukagoshi, Y. Aoyagi, T. Takenobu, and Y. Iwasa, *In-crystal and surface charge transport of electric-field-induced carriers in organic single-crystal semiconductors*, Physical Review Letters **98** (2007), 196804.

[54] V. Podzorov, E. Menard, J. A. Rogers, and M. E. Gershenson, *Hall effect in the accumulation layers on the surface of organic semiconductors*, Phys. Rev. Lett. **95** (2005), 226601.

[55] K. P. Pernstich, B. Rossner, and B. Batlogg, *Field-effect-modulated Seebeck coefficient in organic semiconductors*, Nature Materials **7** (2008), no. 4, 321–325.

[56] S.-i. Machida, Y. Nakayama, S. Duhm, Q. Xin, A. Funakoshi, N. Ogawa, S. Kera, N. Ueno, and H. Ishii, *Highest-Occupied-Molecular-Orbital band dispersion of rubrene single crystals as observed by angle-resolved ultraviolet photoelectron spectroscopy*, Phys. Rev. Lett. **104** (2010), 156401.

[57] S. Duhm, Q. Xin, S. Hosoumi, H. Fukagawa, K. Sato, N. Ueno, and S. Kera, *Charge reorganization energy and small polaron binding energy of rubrene thin films by ultraviolet photoelectron spectroscopy*, Advanced Materials **24** (2012), no. 7, 901–905.

[58] S. Tavazzi, L. Silvestri, M. Campione, A. Borghesi, A. Papagni, P. Spearman, A. Yassar, A. Camposeo, and D. Pisignano, *Generalized ellipsometry and dielectric tensor of rubrene single crystals*, Journal of Applied Physics **102** (2007), no. 2, 023107.

[59] S. Tavazzi, A. Borghesi, A. Papagni, P. Spearman, L. Silvestri, A. Yassar, A. Camposeo, M. Polo, and D. Pisignano, *Optical response and emission waveguiding in rubrene crystals*, Phys. Rev. B **75** (2007), 245416.

[60] P. Irkhin, A. Ryasnyanskiy, M. Koehler, and I. Biaggio, *Absorption and photoluminescence spectroscopy of rubrene single crystals*, Phys. Rev. B **86** (2012), 085143.

[61] H. Najafov, I. Biaggio, V. Podzorov, M. F. Calhoun, and M. E. Gershenson, *Primary photoexcitations and the origin of the photocurrent in rubrene single crystals*, Phys. Rev. Lett. **96** (2006), 056604.

[62] H. Najafov, B. Lyu, I. Biaggio, and V. Podzorov, *Two mechanisms of exciton dissociation in rubrene single crystals*, Applied Physics Letters **96** (2010), no. 18, 183302.

[63] A. Ryasnyanskiy and I. Biaggio, *Triplet exciton dynamics in rubrene single crystals*, Physical Review B **84** (2011), no. 19.

[64] L. Ma, K. Zhang, C. Kloc, H. Sun, M. E. Michel-Beyerle, and G. G. Gurzadyan, *Singlet fission in rubrene single crystal: direct observation by femtosecond pump-probe spectroscopy*, Physical Chemistry Chemical Physics **14** (2012), no. 23, 8307–8312.

[65] M. B. Smith and J. Michl, *Singlet fission*, Chemical Reviews **110** (2010), no. 11, 6891–6936.

[66] P. Irkhin and I. Biaggio, *Direct imaging of anisotropic exciton diffusion and triplet diffusion length in rubrene single crystals*, Phys. Rev. Lett. **107** (2011), 017402.

[67] C. Kloc, K. J. Tan, M. L. Toh, K. K. Zhang, and Y. P. Xu, *Purity of rubrene single crystals*, Applied Physics A **95** (2008), no. 1, 219–224.

[68] O. Mitrofanov, C. Kloc, T. Siegrist, D. V. Lang, Woo-Young So, and A. P. Ramirez, *Role of synthesis for oxygen defect incorporation in crystalline rubrene*, Applied Physics Letters **91** (2007), no. 21, 212106.

[69] O. Mitrofanov, D. V. Lang, C. Kloc, J. M. Wikberg, T. Siegrist, Woo-Young So, M. A. Sergent, and A. P. Ramirez, *Oxygen-Related band gap state in single crystal rubrene*, Physical Review Letters **97** (2006), no. 16, 16601.

[70] Y. Chen, B. Lee, D. Fu, and V. Podzorov, *The origin of a 650 nm photoluminescence band in rubrene*, Advanced Materials **23** (2011), no. 45, 5370–5375.

[71] A. J. Maliakal, J. Y.-C. Chen, Woo-Young So, S. Jockusch, B. Kim, M. F. Ottaviani, A. Modelli, N. J. Turro, C. Nuckolls, and A. P. Ramirez, *Mechanism for Oxygen-Enhanced photoconductivity in rubrene: Electron transfer doping*, Chemistry of Materials **21** (2009), no. 22, 5519–5526.

[72] M. Haemori, J. Yamaguchi, S. Yaginuma, K. Itaka, and H. Koinuma, *Fabrication of highly oriented rubrene thin films by the use of atomically finished substrate and pentacene buffer layer*, Japanese Journal of Applied Physics **44** (2005), no. No. 6A, 3740–3742.

[73] M. Campione, *Rubrene heteroepitaxial nanostructures with unique orientation*, Journal of Physical Chemistry C **112** (2008), no. 42, 16178–16181.

[74] M. Campione, M. Moret, L. Raimondo, and A. Sassella, *Kinetic phase selection of rubrene heteroepitaxial domains*, The Journal of Physical Chemistry C **113** (2009), no. 49, 20927–20933.

[75] C. Kloc, P. G. Simpkins, T. Siegrist, and R. A. Laudise, *Physical vapor growth of centimeter-sized crystals of α-hexathiophene*, Journal of Crystal Growth **182** (1997), no. 3-4, 416–427.

[76] R. A. Laudise, C. Kloc, P. G. Simpkins, and T. Siegrist, *Physical vapor growth of organic semiconductors*, Journal of crystal growth **187** (1998), no. 3-4, 449–454.

[77] S. R. Forrest, *Ultrathin organic films grown by organic molecular beam deposition and related techniques*, Chemical Reviews **97** (1997), no. 6, 1793–1896.

[78] M. A. Herman and H. Sitter, *Molecular beam epitaxy*, Springer, 1999.

[79] M. Campione, M. Cartotti, E. Pinotti, A. Sassella, and A. Borghesi, *Thickness measurements by quartz microbalance during thin-film growth by organic-molecular-beam deposition*, Journal of Vacuum Science & Technology A: Vacuum, Surfaces, and Films **22** (2004), no. 3, 482.

[80] C. Goletti, G. Bussetti, P. Chiaradia, A. Sassella, and A. Borghesi, *Highly sensitive optical monitoring of molecular film growth by organic molecular beam deposition*, Applied Physics Letters **83** (2003), no. 20, 4146–4148.

[81] G. Binnig, C. F. Quate, and Ch. Gerber, *Atomic force microscope*, Phys. Rev. Lett. **56** (1986), 930–933.

[82] F. J. Giessibl, *Advances in atomic force microscopy*, Rev. Mod. Phys. **75** (2003), 949–983.

[83] M. Campione, L. Raimondo, M. Moret, P. Campiglio, E. Fumagalli, and A. Sassella, *Organic-organic heteroepitaxy of semiconductor crystals: α-quaterthiophene on rubrene*, Chemistry of Materials **21** (2009), no. 20, 4859–4867.

[84] M. Campione, E. Fumagalli, L. Raimondo, A. Monguzzi, F. Meinardi, and A. Sassella, *Control of π-π interactions in epitaxial films of platinum(ii) octaethyl porphyrin*, Chemistry of Materials **23** (2011), no. 3, 832–840.

[85] A. Alessandrini and P. Facci, *Afm: a versatile tool in biophysics*, Measurement Science and Technology **16** (2005), no. 6, R65.

[86] R. M. Overney, H. Takano, M. Fujihira, W. Paulus, and H. Ringsdorf, *Anisotropy in friction and molecular stick-slip motion*, Physical Review Letters **72** (1994), no. 22, 3546.

[87] V. Kalihari, E. B. Tadmor, G. Haugstad, and C. D. Frisbie, *Grain orientation mapping of polycrystalline organic semiconductor films by transverse shear microscopy*, Advanced Materials **20** (2008), no. 21, 4033–4039.

[88] M. Campione and E. Fumagalli, *Friction anisotropy of the surface of organic crystals and its impact on scanning force microscopy*, Physical Review Letters **105** (2010), no. 16, 166103.

[89] R. M. Overney, L. Howald, J. Frommer, E. Meyer, and H.-J. Güntherodt, *Molecular surface structure of tetracene mapped by the atomic force microscope*, The Journal of Chemical Physics **94** (1991), no. 12, 8441.

[90] J. P. Cleveland, B. Anczykowski, A. E. Schmid, and V. B. Elings, *Energy dissipation in tapping-mode atomic force microscopy*, Applied Physics Letters **72** (1998), no. 20, 2613.

[91] M. Nonnenmacher, M. P. O'Boyle, and H. K. Wickramasinghe, *Kelvin probe force microscopy*, Applied Physics Letters **58** (1991), no. 25, 2921.

[92] V. Palermo, M. Palma, and P. Samorì, *Electronic characterization of organic thin films by kelvin probe force microscopy*, Advanced Materials **18** (2006), no. 2, 145–164.

[93] A. Liscio, V. Palermo, K. M͑ullen, and P. Samorì, *Tip-Sample interactions in kelvin probe force microscopy: Quantitative measurement of the local surface potential*, Journal of Physical Chemistry C **112** (2008), no. 44, 17368–17377.

[94] H. O. Jacobs, P. Leuchtmann, O. J. Homan, and A. Stemmer, *Resolution and contrast in kelvin probe force microscopy*, Journal of Applied Physics **84** (1998), no. 3, 1168–1173.

[95] U. Zerweck, C. Loppacher, T. Otto, S. Grafstr͑om, and L. Eng, *Accuracy and resolution limits of kelvin probe force microscopy*, Physical Review B **71** (2005), no. 12.

[96] B. L. M. Hendriksen, F. Martin, Y. Qi, C. Mauldin, N. Vukmirovic, JunFeng Ren, H. Wormeester, A. J. Katan, V. Altoe, S. Aloni, J. M. J. Fréchet, Lin-Wang Wang, and M. Salmeron, *Electrical transport properties of Oligothiophene-Based molecular films studied by current sensing atomic force microscopy*, Nano Lett. **11** (2011), no. 10, 4107–4112.

[97] V. Palermo, A. Liscio, M. Palma, M. Surin, R. Lazzaroni, and P. Samorì, *Exploring nanoscale electrical and electronic properties of organic and polymeric functional materials by atomic force microscopy based approaches*, Chemical Communications **32** (2007), 3326.

[98] *Nanoscope software 7.30 user guide*, Veeco, 2008.

[99] D. Nečas and P. Klapetek, *Gwyddion: an open-source software for spm data analysis*, Central European Journal of Physics **10** (2012), 181–188.

[100] N. W. Ashcroft and D. N. Mermin, *Solid State Physics*, Thomson Learning, Toronto, 1976.

[101] C. Kittel, *Introduction to solid state physics*, Wiley, 1971.

[102] E. Prince (ed.), *International Tables for Crystallography Volume C: Mathematical, physical and chemical tables*, IUCr, 2004.

[103] M. Birkholz, *Thin film analysis by x-ray scattering*, Wiley-VCH Verlag GmbH, 2006.

[104] C. W. Schlenker, V. S. Barlier, S. W. Chin, M. T. Whited, R. E. McAnally, S. R. Forrest, and M. E. Thompson, *Cascade organic solar cells*, Chem. Mater. **23** (2011), no. 18, 4132–4140.

[105] F. C. Frank and J. H. van der Merwe, *One-dimensional dislocations. ii. misfitting monolayers and oriented overgrowth*, Proceedings of the Royal Society of London. Series A. Mathematical and Physical Sciences **198** (1949), no. 1053, 216–225.

[106] S. Mannsfeld, K. Leo, and T. Fritz, *Line-on-Line coincidence: A new type of epitaxy found in Organic-Organic heterolayers*, Physical Review Letters **94** (2005), no. 5.

[107] D. E Hooks, T. Fritz, and M. D Ward, *Epitaxy and molecular organization on solid substrates*, Advanced Materials **13** (2001), no. 4, 227–241.

[108] M. Campione, A. Sassella, M. Moret, A. Papagni, S. Trabattoni, R. Resel, O. Lengyel, V. Marcon, and G. Raos, *Organic-organic epitaxy of incommensurate systems: α-quaterthiophene on potassium hydrogen phthalate single crystals*, Journal of the American Chemical Society **128** (2006), no. 41, 13378–13387.

[109] M. Campione, L. Raimondo, and A. Sassella, *Heteroepitaxy of α-Quaterthiophene on tetracene single crystals*, Journal of Physical Chemistry C **111** (2007), no. 51, 19009–19014.

[110] T. Haber, R. Resel, A. Thierry, M. Campione, A. Sassella, and M. Moret, *Epitaxially grown sexiphenyl nanocrystals on the organic KAP (0 1 0) surface*, Physica E: Low-dimensional Systems and Nanostructures **41** (2008), no. 1, 133–137.

[111] Detlef-M. Smilgies and E. J. Kintzel, *Epitaxial orientations of para-sexiphenyl platelets grown on alkali halide (001) surfaces*, Physical Review B **79** (2009), no. 23, 235413.

[112] D. Holmes, S. Kumaraswamy, A. J Matzger, and K. P. C Vollhardt, *On the nature of nonplanarity in the [N]Phenylenes*, Chemistry - A European Journal **5** (1999), no. 11, 3399–3412.

[113] H. Lipson, J. I. Langford, and H.-C. Hu, *Trigonometric intensity factors*, International tables for crystallography, 2006.

[114] Hammersley, *FIT2D: an introduction and overview*, Technical Report ESRF97HA02T, 1997.

[115] C. T. Chantler, N. A. Rae, and C. Q. Tran, *Accurate determination and correction of the lattice parameter of LaB_6 (standard reference material 660) relative to that of Si (640b)*, Journal of Applied Crystallography **40** (2007), no. 2, 232–240.

[116] M. P. Tate, V. N. Urade, J. D. Kowalski, T.-c. Wei, B. D. Hamilton, B. W. Eggiman, and H. W. Hillhouse, *Simulation and interpretation of 2D diffraction patterns from Self-Assembled nanostructured films at arbitrary angles of incidence:Â from grazing incidence (Above the critical angle) to transmission perpendicular to the substrate*, The Journal of Physical Chemistry B **110** (2006), no. 20, 9882–9892.

[117] Detlef-M Smilgies and D. R Blasini, *Indexation scheme for oriented molecular thin films studied with grazing-incidence reciprocal-space mapping*, Journal of Applied Crystallography **40** (2007), no. 4, 716–718.

[118] C. Seoul and H.-L. Zheng, *Preparation of tetracene single crystal: Determination of crystal orientation by electron diffraction*, Materials Science Forum **408-412** (2002), 1753.

[119] R. Resel, N. Koch, F. Meghdadi, G. Leising, W. Unzog, and K. Reichmann, *Growth and preferred crystallographic orientation of hexaphenyl thin films*, Thin Solid Films **305** (1997), no. 1-2, 232–242.

[120] O. Lengyel, T. Haber, O. Werzer, W. Hardeman, D. M De Leeuw, H. J Wondergem, and R. Resel, *Wide-range three-dimensional reciprocal-space mapping: a novel approach applied to organic monodomain thin films*, Journal of Applied Crystallography **40** (2007), no. 3, 580–582.

[121] I. Salzmann and R. Resel, *STEREOPOLE: software for the analysis of x-ray diffraction pole figures with IDL*, Journal of Applied Crystallography **37** (2004), no. 6, 1029–1033.

[122] S. Trabattoni, S. Laera, R. Mena, A. Papagni, and A. Sassella, *Preparation of highly pure quaterthiophene and role of impurities on its photoluminescence properties*, J. Mater. Chem. **14** (2004), 171–178.

[123] Y.-Y. Noh, J.-J. Kim, Y. Yoshida, and K. Yase, *Effect of molecular orientation of epitaxially grown platinum(II) octaethyl porphyrin films on the performance of field-effect transistors*, Advanced Materials **15** (2003), no. 9, 699–702.

[124] H. Yanagi, T. Morikawa, and S. Hotta, *Electroluminescence from low-dimensionally confined crystals of thiophene/p-phenylene co-oligomers*, Applied Physics Letters **81** (2002), no. 8, 1512–1514.

[125] S. Uttiya, L. Raimondo, M. Campione, L. Miozzo, A. Yassar, M. Moret, E. Fumagalli, A. Borghesi, and A. Sassella, *Stability to photo-oxidation of rubrene and fluorine-substituted rubrene*, Synthetic Metals **0** (2011).

[126] L. Raimondo, M. Moret, M. Campione, A. Borghesi, and A. Sassella, *Unique orientation of organic epitaxial thin films: The role of intermolecular interactions at the interface and surface symmetry*, The Journal of Physical Chemistry C **115** (2011), no. 13, 5880–5885.

[127] M. Moret, A. Borghesi, M. Campione, E. Fumagalli, L. Raimondo, and A. Sassella, *Organic-organic heteroepitaxy: facts, concepts and perspectives*, Crystal Research and Technology **46** (2011), no. 8, 827–832.

[128] L. Pastero, D. Aquilano, and M. Moret, *Selective adsorption/absorption of formamide in NaCl crystals growing from solution*, Crystal Growth & Design **12** (2012), no. 5, 2306–2314.

[129] C. Simbrunner, D. Nabok, G. Hernandez-Sosa, M. Oehzelt, T. Djuric, R. Resel, L. Romaner, P. Puschnig, C. Ambrosch-Draxl, I. Salzmann, G. Schwabegger, I. Watzinger, and H. Sitter, *Epitaxy of rodlike organic molecules on sheet silicates - a growth model based on experiments and simulations*, Journal of the American Chemical Society **133** (2011), no. 9, 3056–3062.

[130] D. Beljonne, J. Cornil, L. Muccioli, C. Zannoni, J.-L. Brèdas, and F. Castet, *Electronic processes at organic-organic interfaces: Insight from modeling and implications for opto-electronic devices*, Chemistry of Materials **23** (2011), no. 3, 591–609.

[131] A. Gavezzotti, *Molecular aggregation: Structure analysis and molecular simulation of crystals and liquids*, International Union of Crystallography Monographs on Crystallography, Oxford University Press, USA, 2007.

[132] G. M. Morris, D. S. Goodsell, R. S. Halliday, R. Huey, W. E. Hart, R. K. Belew, and A. J. Olson, *Automated docking using a lamarckian genetic algorithm and an empirical binding free energy function*, Journal of Computational Chemistry **19** (1998), no. 14, 1639–1662.

[133] H. Yang, L. Yang, Mang-Mang Ling, S. Lastella, D. D. Gandhi, G. Ramanath, Z. Bao, and C. Y. Ryu, *Aging susceptibility of Terrace-Like pentacene films*, Journal of Physical Chemistry C **112** (2008), no. 42, 16161–16165.

[134] A. Liscio, V. Palermo, D. Gentilini, F. Nolde, K. Müllen, and P. Samorì, *Quantitative measurement of the local surface potential of π-Conjugated nanostructures: A kelvin probe force microscopy study*, Advanced Functional Materials **16** (2006), no. 11, 1407–1416.

[135] T. Machleidt, E. Sparrer, D. Kapusi, and K. H. Franke, *Deconvolution of Kelvin probe force microscopy measurements-methodology and application*, Measurement Science and Technology **20** (2009), 084017.

[136] A. Bl´umel, H. Plank, A. Klug, E. Fisslthaler, M. Sezen, W. Grogger, and E. J. W. List, *Note: On the deconvolution of Kelvin probe force microscopy data*, Review of Scientific Instruments **81** (2010), no. 5, 056107.

[137] A. Liscio, V. Palermo, and P. Samorì, *Probing local surface potential of Quasi-One-Dimensional systems: A KPFM study of P3HT nanofibers*, Advanced Functional Materials **18** (2008), no. 6, 907–914.

[138] M. C. Burla, R. Caliandro, M. Camalli, B. Carrozzini, G. L. Cascarano, L. De Caro, C. Giacovazzo, G. Polidori, and R. Spagna, *SIR2004: an improved tool for crystal structure determination and refinement*, Journal of Applied Crystallography **38** (2005), no. 2, 381–388.

[139] G. Sheldrick, *SHELXL-97 - programme for structure refinement*, Göttingen, 1997.

[140] A. L. Spek, *Single-crystal structure validation with the program PLATON*, Journal of Applied Crystallography **36** (2003), no. 1, 7–13.

[141] M. J. Frisch, G. W. Trucks, H. B. Schlegel, G. E. Scuseria, M. A. Robb, J. R. Cheeseman, J. A. Montgomery Jr., T. Vreven, K. N. Kudin, J. C. Burant, J. M. Millam, S. S. Iyengar, J. Tomasi, V. Barone, B. Mennucci, M. Cossi, G. Scalmani, N. Rega, G. A. Petersson, H. Nakatsuji, M. Hada, M. Ehara, K. Toyota, R. Fukuda, J. Hasegawa, M. Ishida, T. Nakajima, Y. Honda, O. Kitao, H. Nakai, M. Klene, X. Li, J. E. Knox, H. P. Hratchian, J. B. Cross, V. Bakken, C. Adamo, J. Jaramillo, R. Gomperts, R. E. Stratmann, O. Yazyev, A. J. Austin, R. Cammi, C. Pomelli, J. W. Ochterski, P. Y. Ayala, K. Morokuma, G. A. Voth, P. Salvador, J. J. Dannenberg, V. G. Zakrzewski, S. Dapprich, A. D. Daniels, M. C. Strain, O. Farkas,

D. K. Malick, A. D. Rabuck, K. Raghavachari, J. B. Foresman, J. V. Ortiz, Q. Cui, A. G. Baboul, S. Clifford, J. Cioslowski, B. B. Stefanov, G. Liu, A. Liashenko, P. Piskorz, I. Komaromi, R. L. Martin, D. J. Fox, T. Keith, M. A. Al-Laham, C. Y. Peng, A. Nanayakkara, M. Challacombe, P. M. W. Gill, B. Johnson, W. Chen, M. W. Wong, C. Gonzalez, and J. A. Pople, *Gaussian 03, Revision D.02*. Gaussian, Inc., Wallingford, CT, 2004.

[142] V. De Renzi, R. Rousseau, D. Marchetto, R. Biagi, S. Scandolo, and U. del Pennino, *Metal Work-Function changes induced by organic adsorbates: A combined experimental and theoretical study*, Physical Review Letters **95** (2005), no. 4.

[143] D. J. Ellison, B. Lee, V. Podzorov, and C. D. Frisbie, *Surface potential mapping of SAM-Functionalized organic semiconductors by kelvin probe force microscopy*, Advanced Materials **23** (2011), no. 4, 502–507.

[144] S. Tavazzi, L. Raimondo, L. Silvestri, P. Spearman, A. Camposeo, M. Polo, and D. Pisignano, *Dielectric tensor of tetracene single crystals: The effect of anisotropy on polarized absorption and emission spectra*, The Journal of Chemical Physics **128** (2008), no. 15, 154709.

[145] D. Braga, A. Jaafari, L. Miozzo, M. Moret, S. Rizzato, A. Papagni, and A. Yassar, *The rubrenic synthesis: The delicate equilibrium between tetracene and cyclobutene*, European Journal of Organic Chemistry **2011** (2011), no. 22, 4160–4169.

[146] M. Kytka, L. Gisslen, A. Gerlach, U. Heinemeyer, J. Kovàč, R. Scholz, and F. Schreiber, *Optical spectra obtained from amorphous films of rubrene: Evidence for predominance of twisted isomer*, The Journal of Chemical Physics **130** (2009), no. 21, 214507.

[147] J. L. Zhenan Bao and J. J. Locklin, *Organic field-effect transistors*, Optical Science And Engineering Series, CRC Press, 2007.

PhD activity

Publications

- M. Campione, L. Raimondo, M. Moret, P. Campiglio, E. Fumagalli, A. Sassella, *Organic-Organic Heteroepitaxy of Semiconductor Crystals: α-Quaterthiophene on Rubrene*, Chemistry of Materials **21**, 4859 (2009)

- M. Campione, E. Fumagalli, L. Raimondo, A. Monguzzi, F. Meinardi, A.Sassella, *Control of $\pi - \pi$ Interactions in Epitaxial Films of Platinum(II) Octaethyl Porphyrin*, Chemistry of Materials **23**, 832 (2011)

- M. Campione and E. Fumagalli, *Friction Anisotropy of the Surface of Organic Crystals and Its Impact on Scanning Force Microscopy*, Phys. Rev. Lett. **105**, 166103 (2010)

- E. Fumagalli, L. Raimondo, L. Silvestri, M. Moret, A. Sassella, M. Campione, *Oxidation Dynamics of Epitaxial Rubrene Ultrathin Films*, Chemistry of Materials, **23**, 3246 (2011)

- S. Uttiya, L. Raimondo, M. Campione, L. Miozzo, A. Yassar, M. Moret, E. Fumagalli, A. Borghesi, A. Sassella, *Stability to photo-oxidation of rubrene and fluorine-substituted rubrene*, Synthetic Metals **161**, 2603 (2012)

- M. Moret, A. Borghesi, M. Campione, E. Fumagalli, L. Raimondo, A. Sassella, *Organic-organic heteroepitaxy: facts, concepts and perspectives*, Crystal Research and Technology, **46**, 827 (2011)

- E. Fumagalli, M. Campione, L. Raimondo, A. Sassella, M. Moret, L. Barba, G. Arrighetti, *Grazing-incidence X-ray diffraction study of rubrene epitaxial thin films*, Journal of Synchrotron Radiation **19**, 682 (2012)

Presentations at congresses

- Poster presentation at E-MRS Spring Meeting 2011, 9th - 13th May 2011, Nice (France). Winner of the best poster prize;

- Poster presentation at Gordon Research Conference *Electronic Processes in Organic Materials*, 3rd - 8th June 2012, Barga, Lucca (Italy).

Attended courses

- 1st International Summer School on Materials for Renewable Energy - Erice (Italy), May 28th - June 2nd 2010.

- 12th International Conference-PCAM School on Advanced Materials and Technologies - Palanga (Lituania). 27th - 31th August 2010.